A TIME DOMAIN STRIP THEORY APPROACH TO PREDICT MANEUVERING IN A SEAWAY

by

Rahul Subramanian

A dissertation submitted in partial fulfillment
of the requirements for the degree of
Doctor of Philosophy
(Naval Architecture and Marine Engineering)
in The University of Michigan
2012

Doctoral Committee:

Professor Robert F. Beck, Chair
Associate Professor Bogdan Epureanu
Senior Associate Research Scientist Okey G. Nwogu
Professor Armin W. Troesch

ACKNOWLEDGEMENTS

I would like to humbly acknowledge everyone who has directly or indirectly helped in making this dissertation a success.

First and foremost, I would like to thank my adviser and mentor, Prof. Beck for giving me the opportunity to work with him. His immense knowledge, experience and insight in the subject have helped make this dissertation possible. His easy going nature and friendly personality have made it a pleasure to work with him. His kind words of encouragement and appreciation have helped me overcome even the most stressful phases of my research work.

I would like to thank my doctoral committee members, Prof. Troesch, Prof. Epureanu, and Dr. Nwogu for their helpful suggestions and comments. They have helped me to obtain new perspectives and insights into the problem.

I would like to express my love and gratitude for my parents Prof. Anantha Subramanian and Mrs. Prema for all their support and encouragement. My dad being a naval architect himself, inspired me from my early days to pursue a career in naval architecture and ocean engineering. A special thanks also goes out to our family friend Mr. GRP Subramaniam for all his help. A special thanks also goes out to my sister Gayathri, for all her encouragement and moral support.

A big thanks goes to my dear friends, Johny, Venky, Mahesh, Prasanna, Iyer, Manu, M Harish, Rajhesh, and Thrushal who not only supported me but also made my stay in Ann Arbor a memorable one.

I would like to thank Dr. Maki and his research team, in particular William

Rosemurgy and John for helping me set up the OpenFOAM runs in the final stage of my dissertation work.

I would like to thank my colleagues and staff in the department for all their technical and administrative support.

The project was partially funded by the Office of Naval Research, award number N00014-05-1-0537, and their support is greatly acknowledged.

TABLE OF CONTENTS

LIST OF FIGURES

Figure

LIST OF TABLES

Table

LIST OF APPENDICES

Appendix

ABSTRACT

A TIME DOMAIN STRIP THEORY APPROACH TO PREDICT MANEUVERING IN A SEAWAY

by

Rahul Subramanian

Chair: Robert F. Beck

A time-domain body exact strip theory is developed to predict maneuvering of a vessel in a seaway. A frame following the instantaneous position of the ship, by translating and rotating in the horizontal plane, is used to set up the Boundary Value Problem (BVP) for the perturbation potentials. Linearized free surface boundary conditions are used for stability and computational efficiency, and exact body boundary conditions are used to capture nonlinear effects. A nonlinear rigid body equation of motion solver is coupled to the hydrodynamic model to predict ship responses.

At each time-step, a two-dimensional mixed BVP is solved by using a boundary integral technique. Constant strength panels are used on the body surface and desingularised sources are placed above the free surface nodes. The constant strength panels have been shown to have better capability in handling complex hull geometries. The free surface and rigid body equations of motions are evolved in time using a fourth-order Adams-Bashforth technique. A separate BVP is set up to solve for the acceleration potential.

Forced oscillation problems are used to study convergence with respect to time-step size, number of body panels and free surface domain length. The seakeeping prediction capabilities of the method have been established by *Bandyk* (2009).

As a first stage of the research, the drifting of a ship freely floating without power in a seaway is simulated. Simulations are performed with and without viscous corrections, and give some interesting results. The Wigley-I and the containership S-175 are used for these studies. This is used to establish the robustness and stability of the code to perform long time simulations on the order of hundreds of wave periods.

The second stage of the thesis involves the prediction of controlled maneuvers of the containership S-175 in calm waters and in the presence of waves. The turning circle maneuver is performed on the S-175, and results compared with available experimental results. The simulations are able to capture general qualitative aspects and the essential physics of the problem. Computational issues are addressed in this chapter.

The third stage of the research involves the formulation of an empirical surge force model used in the methodology to correct the potential flow results. Comparisons are made with results obtained from open source CFD solver OpenFOAM.

The methodology has been shown to be robust, computationally efficient, and capable of predicting long time simulations of a ship maneuvering in a seaway. Although the basic physics of the problem are captured, the research is in a nascent stage, and computational issues are present. These are addressed wherever possible, and recommendations suggested. Also better models for external forces such as propeller thrust, rudder lift forces, and viscous modeling are required to improve the predictions of the method.

CHAPTER I

Introduction

Ship maneuvering and seakeeping have traditionally been dealt with as separate sub problems. Maneuvering is predicted in calm waters and seakeeping has to do with the response of the ship in waves. These give very important information to the naval architect during the initial stages of design. But in reality, they are coupled in nature. Presence of waves are known to effect course keeping and maneuvering performance of a ship by way of wave induced drift forces. On the other hand, maintaining a given course can induce severe ship motions, increase resistance and decrease propulsive efficiency and speed.

1.1 Background

Mathematical models have been used by several authors to study maneuvering of ships in a seaway. *Hirano et al.* (1980) used three-dimensional equations of motion in calm water to predict maneuvering performance by computing only wave drift forces. *McCreight* (1986) developed a maneuvering model in waves, in which the hydrodynamic forces were evaluated in a body-fixed coordinate system. The hydrodynamic coefficients were computed by linear strip-theory. *Ottosson and Bystrom* (1991) used a more simplified approach, where the hydrodynamic radiation coefficients were assumed to be constant based on mean encounter frequency during maneuvering motion.

Fang et al. (2005) developed a mathematical model taking into account the frequency of encounter into the time-domain simulation.

The models mentioned above do not take into account the memory effect due to ship motions. One popular approach to do so is the use of linear convolution integrals of *Cummins* (1962). *Bailey et al.* (1997) and *Fossen* (2005) have developed unified models for maneuvering in a seaway, using this approach. Recently *Skejic and Faltinsen* (2008) have developed a unified 4-DOF maneuvering model in which the mean 2^{nd} order wave loads were added using a direct pressure integration scheme. A two time scale approach was used in their methodology where the high frequency seakeeping was separated from the low frequency maneuvering problem. *Lin et al.* (2006) and *Yen et al.* (2010) solved the unified problem using a three-dimensional panel method. Their study was basically an extension of the nonlinear ship motion prediction code LAMP (Large Amplitude Motion Program). Recently, *Seo and Kim* (2011) extended the time-domain motion program WISH (computer program for nonlinear Wave Induced load and SHip motion analysis) based on a B-spline Rankine panel method to couple seakeeping and maneuvering. Second order wave drift forces were computed by direct pressure integration and modular-type maneuvering model (MMG) is integrated with seakeeping model.

Experimental methods, although an important tool to estimate wave effects on ship maneuvering, and to validate mathematical models and numerical methods; are difficult to conduct, very expensive and can suffer from scale effects. Nonetheless, several results have been presented using free-running model tests. *Hirano et al.* (1980) performed turning circle maneuvers in regular waves. *Ueno et al.* (2003) have carried out turning, zig-zag and stopping tests with a VLCC model. Recently, *Yasukawa and Nakayama* (2009) performed turning circle tests of the containership S-175 in both calm water as well as in waves for a variety of incident wave frequencies, amplitudes and headings.

There has been a lot of recent interest in CFD based methods. Although the increase in modern computational power has made it feasible to solve the viscous flow problem in the time-domain, as is done in unsteady Reynolds-Averaged Navier-Stokes (RANS) codes, the computational effort still remains enormous. Simply performing a one-minute maneuver may take several hundreds of CPU hours to simulate.

1.2 Overview

This dissertation presents the development of a unified model for predicting the maneuvering of a ship in a seaway by using a time-domain, strip theory approach. A hydrodynamic frame following the instantaneous position of the ship in the horizontal plane is used to set up the BVP. This has the advantage that the path and forward speed of the ship need not be described in advance, rather all 6 degrees of freedom are determined by solving the equations of motion.

The strip theory approach allows for faster computational times and simplified body geometry definition. The use of a blended method ensures that vital nonlinearities are captured while keeping the computational time down.

The theory, numerical methods, results, validations and discussion will be described in the following chapters.

Chapter II describes the problem formulation. This includes the coordinate frames used to set up the problem, conventions used, explanation and justification of assumptions made, and description of boundary conditions. The coupling of the hydrodynamic problem to the equations of motion, the acceleration potential formulation, and modeling of external forces such as propeller thrust, rudder forces, resistance and viscous forces are described in detail.

Chapter III describes the details of the numerical schemes used, including discretization techniques, time marching schemes for the free surface evolution and equations of motion solver, the details of the numerical damping beach, and radial basis

functions to obtain x-derivatives.

Chapter IV presents the results of the free motion drift simulation of the containership S-175, and Wigley-I hull form.

Chapter V presents the results of the turning circle maneuvers of the containership S-175 in calm water, and in the presence of regular waves. Comparisons are made with available experimental results.

Chapter VI presents the results for the surge damping model used to augment the potential flow results, and comparison with CFD simulations.

Chapter VII summarizes the dissertation work, and discusses the computational issues present, recommendations and considerations for future work.

CHAPTER II

Problem Formulation

2.1 Definition Sketch

The problem definition is as shown in Figure 2.1 where a freely floating rigid body such as a ship is moving either in calm water or in the presence of external waves. The objective is to predict the hydrodynamic forces acting on the ship and the resultant motions and trajectory of such a body.

Three different coordinate systems are used for solving the problem; an earth fixed inertial axis (x_e, y_e, z_e) is used to keep track of the position of the centre of gravity of the ship and the Euler angles. A hydrodynamic frame (x_h, y_h, z_h) translates in the horizontal calm water plane with translational velocities U, V and rotational yaw rate $\dot{\psi}$. It thus follows the ship such that its origin O_h is always in vertical line with the origin of the body frame, O_b. This is the frame in which the boundary value problem is formulated in. A body fixed frame (x_b, y_b, z_b) rotates and translates in all 6-DOF with the body. The frame is used to compute the forces acting on the ship and to solve for the equations of motions.

The velocities U, V and $\dot{\psi}$ are the instantaneous body velocities resolved in the hydrodynamic frame.

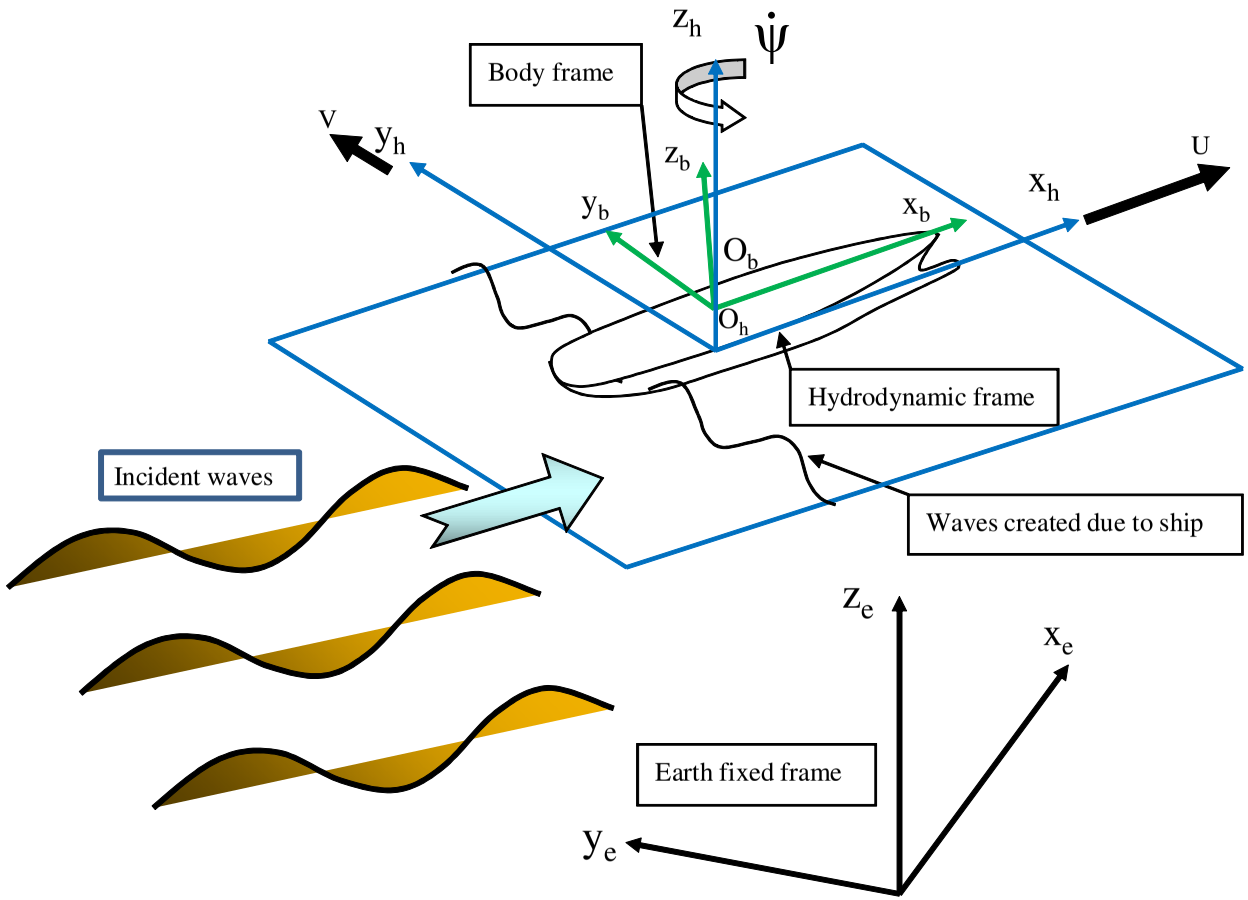

Figure 2.1: SCHEMATIC SHOWING DIFFERENT COORDINATE FRAMES USED

2.2 Mathematical Formulation

Basic Assumptions

The fluid flow problem in marine hydrodynamics is complicated and challenging. In order to account for viscous effects like wakes, boundary layers, flow separation and turbulence, there has been a tendency towards the development of numerical methods based on the Navier-Stokes equations. But even with the increase in modern computational power, the computer time needed to compute even a few minutes of real-time simulation remains large and requires enormous amounts of computational resources. Furthermore, reliable turbulence models are still an area of active research.

Fortunately, the physical model can be simplified considerably without losing its overall validity. The flow conditions can be assumed such that (i) the fluid is homogeneous and incompressible (small Mach number), (ii) the fluid is inviscid, and (iii) the flow is free of vorticity at $t = 0$. For an inviscid flow this would imply that the flow remains irrotational. Combining these assumptions leads to an incompressible, inviscid and irrotational fluid flow formulation, namely the potential flow model.

Governing Equations

The generalized three-dimensional potential flow problem can be formulated in terms of a velocity potential ϕ, representing the perturbation potential for the absolute fluid velocity. The velocity vector $\vec{v}$ can be written as:

$$\mathbf{v} = \nabla\phi \tag{2.1}$$

From Equation (2.1), the continuity equation for the conservation of mass of the fluid reduces to the Laplace's equation

$$\nabla^2\phi = 0 \tag{2.2}$$

The relationship between the coordinates (x_e, y_e, z_e) in the earth fixed frame and the coordinates (x_h, y_h, z_h) in the hydrodynamic frame are given by:

$$x_e = x_h \cos\psi(t) - y_h \sin\psi(t) + I \tag{2.3}$$

$$y_e = x_h \sin\psi(t) + y_h \cos\psi(t) + J \tag{2.4}$$

where

$$I = \int^t (U(\tau)\cos\psi(\tau) - V(\tau)\sin\psi(\tau))d\tau \tag{2.5}$$

$$J = \int^t (U(\tau)\sin\psi(\tau) + V(\tau)\cos\psi(\tau))d\tau \tag{2.6}$$

I and J are the x and y coordinates of the origin of the hydrodynamic frame with respect to the earth fixed frame as shown in Figure 2.2.

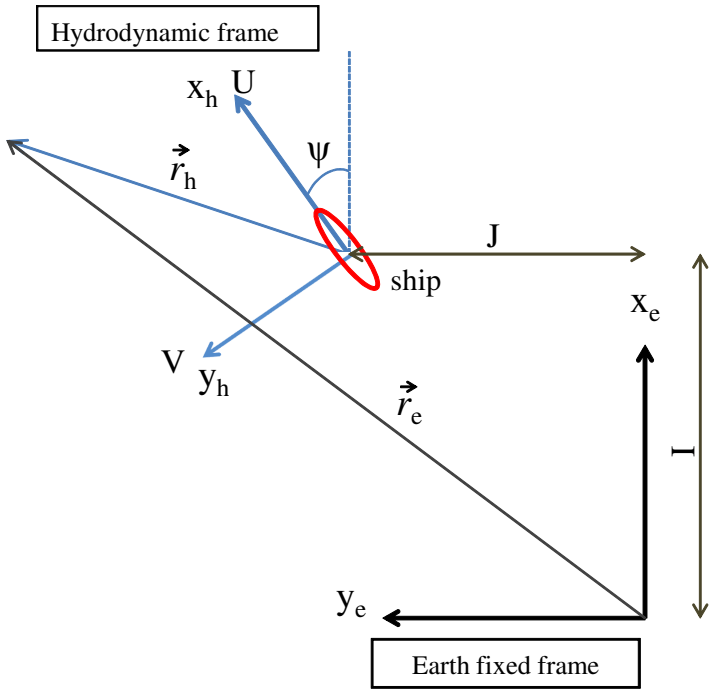

Figure 2.2: OVERHEAD VIEW OF COORDINATE FRAMES

Here,

$U(\tau), V(\tau)$ = translational velocities of the hydrodynamic frame resolved in the hydrodynamic frame.

τ = a dummy variable for integration representing time.

ψ = the heading angle of the hydrodynamic frame with respect to the earth fixed frame.

From the above equations, the relationship between the time derivative in the hydrodynamic and earth fixed frame is:

$$\left.\frac{\partial}{\partial t}\right|_e = \left.\frac{\partial}{\partial t}\right|_h - (\mathbf{U}\cdot\nabla) - (\dot{\mathbf{\Psi}}\times\mathbf{r_h})\cdot\nabla \tag{2.7}$$

$\left.\frac{\partial}{\partial t}\right|_e$ denotes the temporal derivative with respect to the earth fixed frame

$\left.\frac{\partial}{\partial t}\right|_h$ denotes the temporal derivative with respect to the hydrodynamic frame

$\mathbf{U}$ is the translational velocity vector of the hydrodynamic frame resolved in the hydrodynamic frame and given by $(U, V, 0)$

$\dot{\mathbf{\Psi}}$ is the rotational rate of the hydrodynamic frame given by $(0, 0, \dot{\psi})$

$\vec{r}_e$ and $\vec{r}_h$ are the position vector of a point in the earth fixed and hydrodynamic frame, respectively.

Using the relation in Equation (2.7), the Euler equations representing the momentum conservation equations reduce to the unsteady Bernoulli equation in the translating and rotating hydrodynamic frame:

$$\frac{p}{\rho} + \frac{\partial\phi}{\partial t} - \mathbf{U}\cdot\nabla\phi - (\dot{\mathbf{\Psi}}\times\mathbf{r_h})\cdot\nabla\phi + \frac{1}{2}\nabla\phi\cdot\nabla\phi + gz = c(t) \tag{2.8}$$

Here $\frac{\partial\phi}{\partial t}$ represents the temporal derivative of the potential taken with respect to the hydrodynamic frame.

Alternatively, the pressure can also be written with respect to the earth fixed

frame

$$\frac{p}{\rho} + \left.\frac{\partial \phi}{\partial t}\right|_e + \frac{1}{2}\nabla\phi \cdot \nabla\phi + gz = c(t) \tag{2.9}$$

where $\left.\frac{\partial \phi}{\partial t}\right|_e$ represents the temporal derivative of the perturbation potential with respect to the earth fixed frame.

Boundary Conditions

The boundary conditions on the free surface are the linearized kinematic and dynamic free surface boundary conditions, which follow from the fact that a fluid particle remains on the free surface and that the pressure is constant everywhere on the actual free surface respectively. These are derived in the hydrodynamic frame. The linearized kinematic free surface boundary condition

$$\frac{\partial \eta}{\partial t} = \frac{\partial \phi}{\partial z} + (\mathbf{U} + \dot{\mathbf{\Psi}} \times \mathbf{r_h}) \cdot \nabla\eta \qquad \text{on z} = 0 \tag{2.10}$$

and the linearized dynamic free surface boundary condition

$$\frac{\partial \phi}{\partial t} = -g\eta + (\mathbf{U} + \dot{\mathbf{\Psi}} \times \mathbf{r_h}) \cdot \nabla\phi \qquad \text{on z} = 0 \tag{2.11}$$

Here, η represents the free surface wave elevation which is measured from the calm water surface.

The body boundary condition is that of non-penetration of the fluid, which translates to no normal flow through the body surface

$$\nabla\phi \cdot \mathbf{n} = \boldsymbol{v} \cdot \mathbf{n} \qquad \text{on} \quad S_B(t) \tag{2.12}$$

where ϕ is the total perturbation potential, $\boldsymbol{v}$ is the absolute velocity of a node on the body surface with respect to the earth fixed frame including velocities due to

rotational effects; $\mathbf{n}$ is the unit normal vector positive out of the fluid (or into the body), and $S_B(t)$ is the exact wetted body surface.

The boundary conditions at ∞ will be discussed in detail in the following sections where the two-dimensional strip theory boundary value problem is described.

2.3 Strip Theory Approximation

The three-dimensional hull surface can be defined in a mathematical form as $y = \pm b(x, z)$. Then the three-dimensional unit normal vector is given by:

$$\mathbf{n} = (n_1, n_2, n_3) = \frac{(b_x, \mp 1, b_z)}{\sqrt{{b_x}^2 + 1 + {b_z}^2}} \tag{2.13}$$

Here $b_x = \frac{\partial b}{\partial x}$ and $b_z = \frac{\partial b}{\partial z}$. The unit normals are defined positive into the body.

If the slope of the body surface in the x-direction is assumed relatively small, i.e $b_x \ll (1, b_z)$, it follows that length (L) of the ship is large compared to it's beam (B) and draft (T), i.e $L = O(1)$; $B, T = O(\epsilon)$. Thus the unit normals can be approximated as

$$\mathbf{N} = (N_1, N_2, N_3) = \frac{(b_x, \mp 1, b_z)}{\sqrt{1 + {b_z}^2}} \tag{2.14}$$

$\mathbf{N}$ is defined as the strip theory unit normal vector. The two-dimensional unit normal that will be used in the formulation is given by $(0, N_2, N_3)$. This has unit magnitude and is used to satisfy the two-dimensional body boundary conditions. N_1 is a fictitious normal in the $x-$direction that will be used to obtain the surge forces. It is also useful to define (N_4, N_5, N_6) as:

$$(N_4, N_5, N_6) = \mathbf{r_b} \times \mathbf{N} \tag{2.15}$$

where $\mathbf{r_b}$ is the position vector of a node on the body surface with respect to the

body fixed frame. Now, the slender-body approximation is used to reduce the three-dimensional problem into a series of two-dimensional problems at each station or section of the ship. The detailed boundary value problem is explained in the next section.

2.4 Strip Theory Boundary Value Problem

Based on the assumptions stated in Section 2.3, the three-dimensional BVP in Section 2.2 gets reduced to the following two-dimensional BVP:

$$\nabla^2\phi(y,z,t;x) = 0 \tag{2.16}$$

Here $\phi = \phi(y,z,t;x)$ shall henceforth refer to the two-dimensional potential for notational convenience.

The free surface boundary conditions take the following form from Equations (2.10) and (2.11):

$$\frac{\partial\eta}{\partial t} = \frac{\partial\phi}{\partial z} + V\frac{\partial\eta}{\partial y} + x_h\dot{\psi}\frac{\partial\eta}{\partial y} \qquad \text{on z} = 0 \tag{2.17}$$

$$\frac{\partial\phi}{\partial t} = -g\eta + V\frac{\partial\phi}{\partial y} + x_h\dot{\psi}\frac{\partial\phi}{\partial y} \qquad \text{on z} = 0 \tag{2.18}$$

Consistent with strip theory, the encounter frequency is assumed high such that, $\frac{\partial}{\partial t} \gg U\frac{\partial}{\partial x}$ and the downstream free surface effects are ignored.

In the far field, a radiation boundary condition is imposed such that only the incident waves are incoming. This is done numerically by incorporating an outer damping beach and modifying the free surface boundary conditions. The details for this would be explained in the next Chapter dealing with numerical schemes. All simulations are carried out in deep water and so the gradient of the perturbation potential vanishes as $z \to -\infty$. This is automatically taken care of by the selection

of the Green function, which will be shown in the following section.

Velocity Potential Decomposition and Body Boundary Conditions

The perturbation potentials can be broken down into different components for proper bookkeeping:

$$\phi(y, z, t; x) = \phi_I + \phi_D + \phi_R$$

where,

$$\phi_I = \text{incident wave potential}$$

$$\phi_D = \text{diffracted potential}$$

$$\phi_R = \text{radiated potential}$$

The incident wave potential and elevation are known at all time and the linear Airy wave theory is used. The analytical expressions for the potential and wave elevation with respect to the earth fixed inertial frame are:

$$\phi_I = \frac{iga}{\omega_0} e^{-ik(x_e \cos\beta + y_e \sin\beta)} e^{i\omega_0 t} e^{kz} \tag{2.19}$$

$$\eta_I = a e^{-ik(x_e \cos\beta + y_e \sin\beta)} e^{i\omega_0 t} \tag{2.20}$$

Here,

a = wave amplitude

ω_0 = absolute wave frequency

k = wave number, given by $2\pi/\lambda$

λ = wavelength

β = heading angle with respect to the earth fixed x-axis

The body boundary condition (2.12) is re-written in terms of it's individual components in the two-dimensional frame

$$\nabla\phi_D \cdot \mathbf{N} = -\nabla\phi_I \cdot \mathbf{N} \quad \text{on } S_B(t) \tag{2.21}$$

$$\nabla\phi_R \cdot \mathbf{N} = \boldsymbol{v} \cdot \mathbf{N} \quad \text{on } S_B(t) \tag{2.22}$$

Here the two-dimensional strip theory normal $\mathbf{N}$ discussed in Section 2.3 is used. $S_B(t)$ is the instantaneous wetted body surface. The details of the blending scheme are given in Section 3.4.

The velocity $\boldsymbol{v}$ used in Equation (2.22) is the velocity of a node on the body surface with respect to the earth fixed frame and includes all the three translational and rotational components, namely (u, v, w, p, q, r). Since this is a strip theory formulation, care has to be taken not to include the steady forward speed component of the velocity into the body boundary condition, as this represents a steady flux of fluid into the two-dimensional domain and can cause continuity issues. In any case, solving the steady forward speed problem in a strip-theory formulation is of little use. In order to circumvent this problem, the following procedure is used. The velocity $\boldsymbol{v}$ can be assumed to consist of a time-varying mean component $\bar{\boldsymbol{v}}(t)$, and an oscillatory

component $\tilde{\boldsymbol{v}}(t)$, such that

$$\boldsymbol{v} = \bar{\boldsymbol{v}}(t) + \tilde{\boldsymbol{v}}(t) \tag{2.23}$$

The mean component is computed at every time-step by taking the average of the body velocities over the last number of time-steps

$$\bar{\boldsymbol{v}}(t) = \frac{\sum_{j=i-1}^{i-N+1} \boldsymbol{v}(t_j)}{T_{interval}} \tag{2.24}$$

where i is the current time level, j is the counter variable, $T_{interval}$ is the length of the interval for averaging, and N is the number of time-steps in the interval. $T_{interval}$ is chosen as the period of the incident waves. It is important to note that the averaging is done only in the x-direction, and other degrees are untouched and the velocities are fully solved for.

The modified body boundary condition is as follows

$$\nabla\phi_R \cdot \mathbf{N} = (\boldsymbol{v} - \boldsymbol{U}_{avg}) \cdot \mathbf{N} \quad \text{on } S_B(t) \tag{2.25}$$

where $\boldsymbol{U}_{avg}$ is the mean surge component that is not solved for and given by $(\bar{u}, 0, 0, 0, 0, 0)^T$.

2.5 Boundary Integral Method

To solve for the two-dimensional problem, Green's theorem is used with respect to the potential to write the fluid flow problem as a set of boundary integral equations. The source distribution method is used in this formulation and the perturbation potential is given by:

$$\phi(\mathbf{x}) = \int_C \sigma(\boldsymbol{\xi}) G(\mathbf{x}; \boldsymbol{\xi}) dC \tag{2.26}$$

where,

C = contour defining the perimeter of the 2-D boundary,

$\mathbf{x}$ = point anywhere in the fluid domain,

$\boldsymbol{\xi}$ = position of source points on boundary C,

σ = unknown source strength,

G = Green function satisfying Laplace's equation

The two-dimensional Rankine source Green function used is

$$G(\mathbf{x};\boldsymbol{\xi}) = \ln|\mathbf{x}-\boldsymbol{\xi}| \tag{2.27}$$

and has the following attributes

$$\nabla^2 G = 2\pi\delta(\mathbf{x}-\boldsymbol{\xi}) \tag{2.28}$$

$$\nabla G \to 0 \quad \text{as} \quad \mathbf{x} \to \infty \tag{2.29}$$

where δ is the Dirac delta function. The source strengths are determined such that they satisfy the boundary conditions. Once they are determined, the spatial derivatives of the potential can be found directly by using the derivative of Equation (2.26).

2.6 Forces and Moments

The pressure formulation that is used in the current method is the one written in the earth-fixed frame, given by Equation (2.9). The pressure is integrated on the exact body surface to obtain the forces and moments acting on the ship. The sectional forces and moments are first obtained and then the pressure is integrated along the

length of the vessel.

$$\frac{p}{\rho} + \left.\frac{\partial \phi}{\partial t}\right|_e + \frac{1}{2}\nabla\phi \cdot \nabla\phi + gz = 0 \tag{2.30}$$

$$\mathbf{F} = \int_L dx \int_{C_H} p\mathbf{N} dl \tag{2.31}$$

$$\mathbf{M} = \int_L dx \int_{C_H} p\mathbf{r} \times \mathbf{N} dl \tag{2.32}$$

Like the potential, the pressure is segregated into different components.

To avoid numerical differencing, a separate BVP is set up for the term $\frac{\partial \phi}{\partial t}$ known as the acceleration potential formulation. The advantage is it uses the same influence matrix as that of the ϕ problem. The other advantage is that it is stable and not sensitive to the time-step size when computing the pressure on the body, since $\frac{\partial \phi}{\partial t}$ is solved for directly. The details will be explained in the next chapter.

2.7 Equations of Motion

Once the potentials, pressure on the hull and forces and moments acting on the body are determined, using the position and velocity of the body, the equations of motion (EOM) are set up. The formulation here basically uses the convention followed by *Fossen* (1994).

The forces and moments on the ship are described in the body frame, and the equations of motion will be solved in the body frame. The origin of the body frame O_b is set at midships and is such that at $t = 0$, it is at the calm water line. The EOM

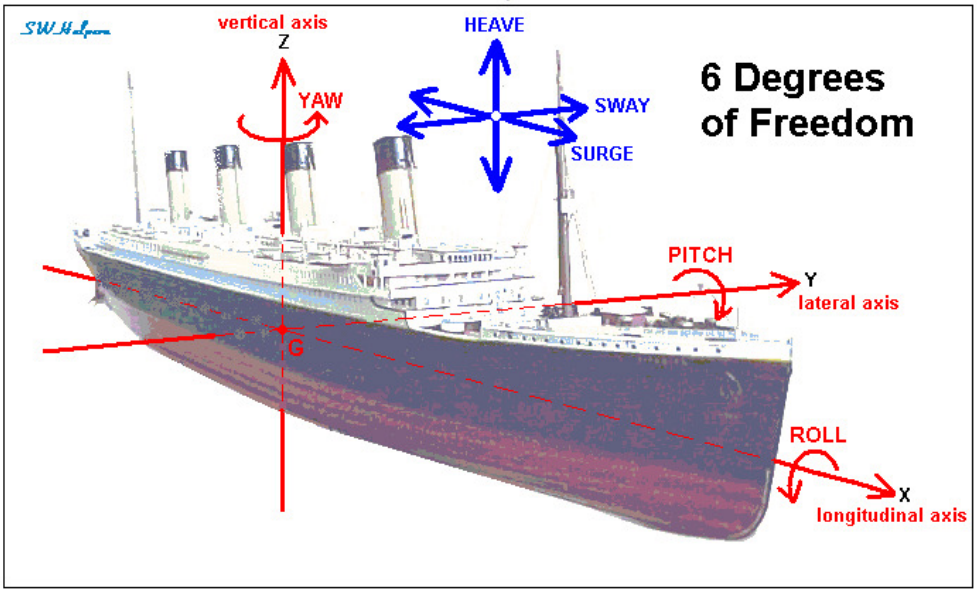

Figure 2.3: BODY COORDINATE SYSTEM SHOWING SIGN CONVENTIONS AND DEFINITIONS OF THE 6-DOF (ILLUSTRATION FROM johnclarkeonline.com)

can be written in compact vector form about O_b as follows:

$$m[\dot{\boldsymbol{v}}_b + \dot{\boldsymbol{\omega}} \times \boldsymbol{r}_g + \boldsymbol{\omega} \times \boldsymbol{v}_b + \boldsymbol{\omega} \times (\boldsymbol{\omega} \times \boldsymbol{r}_g)] + \boldsymbol{m_1}^* \dot{\boldsymbol{v}}_b + \boldsymbol{m_2}^* \dot{\boldsymbol{\omega}} = \mathbf{F} \tag{2.33}$$

$$\boldsymbol{I}_b \dot{\boldsymbol{\omega}} + \boldsymbol{\omega} \times \boldsymbol{I}_b \boldsymbol{\omega} + m\boldsymbol{r}_g \times (\dot{\boldsymbol{v}}_b + \boldsymbol{\omega} \times \boldsymbol{v}_b) + \boldsymbol{m_3}^* \dot{\boldsymbol{v}}_b + \boldsymbol{m_4}^* \dot{\boldsymbol{\omega}} = \mathbf{M} \tag{2.34}$$

where,

$$m = \text{mass of the ship}$$

$$\boldsymbol{v_b} = [u, v, w]^T = \text{linear velocity of body in body frame}$$

$$\boldsymbol{\omega} = [p, q, r]^T = \text{angular velocity of body in body frame}$$

$$\boldsymbol{r_g} = [x_g, y_g, z_g]^T = \text{position vector of CG with respect to } O_b$$

$$\mathbf{F} = [X, Y, Z]^T = \text{force through } O_b \text{ in body frame}$$

$$\mathbf{M} = [K, M, N]^T = \text{moment about } O_b \text{ in body frame}$$

$$\boldsymbol{I_b} = \begin{bmatrix} I_x & -I_{xy} & -I_{xz} \\ -I_{yx} & I_y & -I_{yz} \\ -I_{zx} & -I_{zy} & I_z \end{bmatrix} = \text{generalised moment of inertia matrix}$$

$$\boldsymbol{m}^*(t) = \begin{bmatrix} \boldsymbol{m_1}^*{}_{3\times3} & \boldsymbol{m_2}^*{}_{3\times3} \\ \boldsymbol{m_3}^*{}_{3\times3} & \boldsymbol{m_4}^*{}_{3\times3} \end{bmatrix} = \text{generalised radiation impulsive added mass matrix}$$

The generalised radiation impulsive added mass matrix, $\boldsymbol{m}^*(t)$ represents one part of the solution of the radiation acceleration potential formulation. The details are given in Section 2.8. The generalised force vector can be described by $\mathcal{F} = (\mathbf{F}, \mathbf{M})$. This can be written out in terms of the different components:

$$\mathcal{F} = \mathcal{F}^{FK} + \mathcal{F}^{DIFF} + \mathcal{F}^{RAD} + \mathcal{F}^{S} + \mathcal{F}^{HS} + \mathcal{F}^{VISC} + \mathcal{F}^{PROP} + \mathcal{F}^{CALM} + \mathcal{F}^{RUDDER} \quad (2.35)$$

where,

F^{FK} = exact Froude-Krylov incident wave force

F^{DIFF} = diffracted wave force

F^{RAD} = radiated wave memory force

F^{S} = force due to $\nabla\phi \cdot \nabla\phi$ term in the pressure equation

F^{HS} = exact hydrostatic force

F^{VISC} = empirical viscous forces in roll, sway and yaw DOF

F^{PROP} = propellor thrust force

F^{CALM} = calm water resistance

F^{RUDDER} = rudder force

The vessel's position and orientation are described with respect to the earth fixed coordinates by three translations and rotations, given by $\boldsymbol{\xi}$.

$$\boldsymbol{\xi} = [\xi_1, \xi_2, \xi_3, \phi, \theta, \psi]^T \tag{2.36}$$

Here, $\{\xi_1, \xi_2, \xi_3\}$ represents the three translations and $\{\phi, \theta, \psi\}$ represents the three Euler angles in roll, pitch and yaw respectively. The velocities in the earth fixed frame are obtained from the body velocities by use of transformation matrix.

$$\dot{\boldsymbol{\xi}} = [T]\boldsymbol{v} \tag{2.37}$$

$$T = \begin{bmatrix} T_1 & 0_{3\times3} \\ 0_{3\times3} & T_2 \end{bmatrix}$$

$$T_1 = \begin{bmatrix} \cos\theta\cos\psi & \sin\phi\sin\theta\cos\psi - \cos\phi\sin\psi & \cos\phi\sin\theta\cos\psi + \sin\phi\sin\psi \\ \cos\theta\sin\psi & \sin\phi\sin\theta\sin\psi + \cos\phi\cos\psi & \cos\phi\sin\theta\sin\psi - \sin\phi\cos\psi \\ -\sin\theta & \sin\phi\cos\theta & \cos\phi\cos\theta \end{bmatrix}$$

$$T_2 = \begin{bmatrix} 1 & \frac{\sin\phi\sin\theta}{\cos\theta} & \frac{\cos\phi\sin\theta}{\cos\theta} \\ 0 & \cos\phi & -\sin\phi \\ 0 & \frac{\sin\phi}{\cos\theta} & \frac{\cos\phi}{\cos\theta} \end{bmatrix}$$

2.8 The Acceleration Potential

The pressure equation (2.30) requires the evaluation of the temporal derivative $\frac{\partial\phi}{\partial t}$. In this methodology, a direct formulation is used to set up a BVP for this term, called the "acceleration potential", φ.

This method has a number of advantages. Firstly it allows for direct solution at each time, instead of relying on numerical differencing. It also avoids numerical difficulties with repanelization techniques. Secondly it can be written in terms of the body accelerations $\dot{\boldsymbol{v}}$. It can therefore be moved to the other side of the rigid body equations of motion. Overall it improves stability.

The formulation used here is based on the work of *Bandyk* (2009). Detailed background study, derivations, validations and comparison with other similar formulations can be found in *Bandyk* (2009) and *Bandyk and Beck* (2011).

The idea is that a BVP can be set up for φ in a similar manner as was done for the velocity potential ϕ, since the acceleration potential also satisfies the Laplace equation. A brief derivation of the formulation is as follows. The deep water and far field boundary conditions are satisfied in the same manner as in the velocity potential problem. The derivation of the body boundary conditions are involved and require the application of appropriate time-derivatives in different reference frames. The

following time-derivatives with respect to the earth fixed frame are used:

$$\left.\frac{\delta}{\delta t}\right|_e = \left.\frac{\partial}{\partial t}\right|_e + \boldsymbol{v}\cdot\nabla \tag{2.38}$$

$$\left.\frac{\delta}{\delta t}\right|_b = \left.\frac{\partial}{\partial t}\right|_b + \boldsymbol{\omega}\times \tag{2.39}$$

where, the term $\left.\frac{\delta}{\delta t}\right|_e$ is the prescribed rate of change following a body node with respect to the earth fixed frame and $\left.\frac{\partial}{\partial t}\right|_e$ is the temporal derivative with respect to the earth fixed frame. The quantity $\left.\frac{\delta}{\delta t}\right|_b$ is the prescribed rate of change of a vector defined in the body frame following a body node and $\left.\frac{\partial}{\partial t}\right|_b$ is it's temporal derivative with respect to the body frame. $\boldsymbol{v}$ is the body node velocity given by $\boldsymbol{v_b} + \boldsymbol{\omega}\times\boldsymbol{r_b}$.

The body boundary conditions for φ are derived by taking the time derivative following a body node, $\left.\frac{\delta}{\delta t}\right|_e$ with respect to the earth fixed frame of the equations (2.21) and (2.22).

$$\left.\frac{\delta}{\delta t}\right|_e (\nabla\phi_D\cdot\mathbf{N}) = \left.\frac{\delta}{\delta t}\right|_e (-\nabla\phi_I\cdot\mathbf{N}) \tag{2.40}$$

$$\left.\frac{\delta}{\delta t}\right|_e (\nabla\phi_R\cdot\mathbf{N}) = \left.\frac{\delta}{\delta t}\right|_e (\boldsymbol{v}\cdot\mathbf{N}) \tag{2.41}$$

After applying the chain rule and realizing that $\left.\frac{\partial\mathbf{N}}{\partial t}\right|_b = 0$, the resulting boundary conditions are

$$\mathbf{N}\cdot\nabla\varphi^D{}_e = \mathbf{N}\cdot\nabla\varphi^I{}_e - (\boldsymbol{\omega}\times\mathbf{N})\cdot(\nabla\phi^D+\nabla\phi^I) - \mathbf{N}\cdot[(\boldsymbol{v}\cdot\nabla)(\nabla\phi^D+\nabla\phi^I)] \tag{2.42}$$

$$\mathbf{N}\cdot\nabla\varphi^R{}_e = \{\dot{\boldsymbol{v}}_{\boldsymbol{b}}\cdot\mathbf{N} + (\dot{\boldsymbol{\omega}}\times\mathbf{r_b})\cdot\mathbf{N}\} - (\boldsymbol{\omega}\times\mathbf{N})\cdot\nabla\phi^R - \mathbf{N}\cdot[(\boldsymbol{v}\cdot\nabla)(\nabla\phi^R)] \tag{2.43}$$

The above formulations give the body boundary conditions for the acceleration potential φ_e for the diffraction and radiation components with respect to the earth fixed frame of reference. They can alternatively be derived with respect to the hydrody-

namic frame by using Equation (2.7) which relates the time derivative in the two frames

$$\varphi_e = \varphi_h - U\frac{\partial \phi}{\partial x} - V\frac{\partial \phi}{\partial y} + \dot{\psi}\left(y_h\frac{\partial \phi}{\partial x} - x_h\frac{\partial \phi}{\partial y}\right) \tag{2.44}$$

The free surface boundary condition is straightforward and follows directly from the dynamic free surface boundary condition in Equation (2.18) for the ϕ problem. By using the relation in Equation (2.44)

$$\varphi_e|_{FS} = -g\eta \qquad \text{on } z = 0 \tag{2.45}$$

At this point, since all the potentials and derivatives are solved for, all the quantities on the RHS of equations (2.42) and (2.43) are known with the exception of the first two terms within the $\{\}$ of equation (2.43) involving the body accelerations $\dot{\boldsymbol{v}}_{\boldsymbol{b}}$ and $\dot{\boldsymbol{\omega}}$.

The radiation acceleration potential φ^R is split into two components, the impulsive $\varphi^{R,\ Imp}$ and memory $\varphi^{R,\ Memory}$, subject to the following boundary conditions

$$\varphi^R = \varphi^{R,\ Imp} + \varphi^{R,\ Memory} \tag{2.46}$$

$$\mathbf{N}\cdot\nabla\varphi^{R,\ Imp}{}_e = \dot{\boldsymbol{v}}_{\boldsymbol{b}}\cdot\mathbf{N} + (\dot{\boldsymbol{\omega}}\times\mathbf{r_b})\cdot\mathbf{N} \quad \text{on} \quad S_B(t) \tag{2.47}$$

$$\mathbf{N}\cdot\nabla\varphi^{R,\ Memory}{}_e = -(\boldsymbol{\omega}\times\mathbf{N})\cdot\nabla\phi^R - \mathbf{N}\cdot[(\boldsymbol{v}\cdot\nabla)(\nabla\phi^R)] \quad \text{on} \quad S_B(t) \tag{2.48}$$

$$\varphi^{R,\ Imp} = 0 \quad \text{on} \quad S_{FS} \tag{2.49}$$

$$\varphi^{R,\ Memory} = \varphi^R{}_e\big|_{FS} \quad \text{on} \quad S_{FS} \tag{2.50}$$

The body boundary conditions are applied on the instantaneous wetted body surface, $S_B(t)$. It is observed that the impulsive component is only a function of body accelerations and is reduced into six canonical problems. For notational convenience, let

χ represent $\varphi^{R,\ Imp}$. Then χ can be represented as follows

$$\chi = \sum_{i=1}^{6} \dot{v}_i \chi_i \tag{2.51}$$

where $\dot{v}_i$ andχ_i are the acceleration and scaled acceleration potential, due to a unit body acceleration, in the i^{th} mode of motion. They are such that they satisfy the following boundary conditions

$$\mathbf{N} \cdot \nabla \chi_i = N_i \quad \text{for} \quad (i = 1, ...6) \quad \text{on} \quad S_B(t) \tag{2.52}$$

$$\chi_i = 0 \quad \text{for} \quad (i = 1, ...6) \quad \text{on} \quad S_{FS} \tag{2.53}$$

The solution of the χ_i problem produces the $\boldsymbol{m}^*$ impulsive added mass matrix seen in Section 2.7. The components are given by

$$m^*_{ij} = \rho \int_L dx \int_{S_B(t)} \chi_j N_i dl \tag{2.54}$$

These terms are then moved to the other side of the equations of motions (2.33) and (2.34). On the other hand, the solution of $\varphi^{R,\ Memory}$ goes directly into the pressure equation and is integrated over the entire body to give $\boldsymbol{F}^{RAD}$, the radiation memory force in Equation (2.35).

2.9 External Forces

The external forces acting on the body constitute the last four terms in the Equation (2.35), namely the viscous forces in roll, sway and yaw, propeller thrust force, calm water resistance and forces from control surfaces such as rudder, fins or thrusters.

Viscous Forces

Potential theory does not capture the effects of viscosity. Seakeeping problems are dominated by inertial effects. However, there are scenarios where viscosity plays a vital role. This is especially true of vortical flows characterized by separation such as roll. Crucially, slow motion maneuvering is viscous dominated since potential theory predicts zero damping force at zero frequency limit.

Additional roll viscous damping is used in this formulation. The model is based on the empirical corrections made by *Himeno* (1981). The amount of damping is a function of the hull form and the section shape, and is usually determined from experimental results.

The viscous force model used in sway and yaw is based on linear and nonlinear maneuvering coefficients obtained either from experimental captive model tests such as Planar Motion Mechanism (PMM) or from empirical formulas from regression analysis.

The maneuvering coefficients used in Chapter V on the maneuvering of the container ship S-175 in calm water and waves are the PMM based derivatives in *Son and Nomoto* (1981).

$$X_{visc} = X_{vr}vr + X_{vv}v^2 + X_{rr}r^2 \qquad \text{surge damping} \tag{2.55}$$

$$Y_{visc} = Y_v v + Y_r r + Y_{vvv}v^3 + Y_{rrr}r^3 + Y_{vvr}v^2 r + Y_{vrr}vr^2 \quad \text{sway damping} \tag{2.56}$$

$$N_{visc} = N_v v + N_r r + N_{vvv}v^3 + N_{rrr}r^3 + N_{vvr}v^2 r + N_{vrr}vr^2 \quad \text{yaw damping} \tag{2.57}$$

where X_{visc}, Y_{visc} and N_{visc} are the viscous damping forces in surge, sway and yaw respectively. These terms would show up on the right hand side of a typical modular-type mathematical maneuvering model (MMG model). The forces proportional to the body accelerations, namely the added mass terms are accounted for by potential theory. The terms $Y_v v$, $Y_r r$, $N_v v$ and $N_r r$ are related to wave damping and hull lifting

forces. The strip theory formulation gives zero wave damping because the waves are too short to be resolved at slow speeds, but as will be discussed in Chapter V, it does predict a lift and moment. The lift and moments are already accounted for in the values of $Y_j, N_j (j = 2, 6)$ used in Equations (2.56) and (2.57). This implies that they are being "double counted". A detailed analysis of this phenomenon and solution of this problem is currently outside the scope of the work, but related work can be found in *Yen et al.* (2010) and *Seo and Kim* (2011).

Alternatively, an empirical method can be used to obtain the values of the linear maneuvering derivatives. In Chapter IV, where the free motion drift simulations of the containership S-175 and Wigley-I hull form in waves are presented, a semi-empirical method proposed by *Clarke et al.* (1983) is used. The hull is assumed to be a low aspect ratio wing and the maneuvering coefficients are a function of the length to draft ratio of the ship. The non-dimensional coefficients are given by the following empirical formulas

$$Y_v^{'} = -\pi \left(\frac{T}{L}\right)^2 \left(1.0 + 0.4 C_B \frac{B}{T}\right) \tag{2.58}$$

$$Y_r^{'} = -\pi \left(\frac{T}{L}\right)^2 \left(-0.5 + 2.2 \frac{B}{L} - 0.08 \frac{B}{T}\right) \tag{2.59}$$

$$N_v^{'} = -\pi \left(\frac{T}{L}\right)^2 \left(0.5 + 2.4 C_B \frac{T}{L}\right) \tag{2.60}$$

$$N_r^{'} = -\pi \left(\frac{T}{L}\right)^2 \left(0.25 + 0.039 \frac{B}{T} - 0.56 \frac{B}{L}\right) \tag{2.61}$$

where L, B, T, C_B are the length, beam, draft and the block coefficient of the hull.

The dimensional values are given by

$$Y_v = Y_v^{'} 0.5 \rho L^2 U_{net} \tag{2.62}$$

$$Y_r = Y_r^{'} 0.5 \rho L^3 U_{net} \tag{2.63}$$

$$N_v = N_v^{'} 0.5 \rho L^3 U_{net} \tag{2.64}$$

$$N_r = N_r^{'} 0.5 \rho L^4 U_{net} \tag{2.65}$$

where ρ is the fluid density and $U_{net} = \sqrt{u^2 + v^2}$ is the net speed of the ship.

The rest of the terms in Equations (2.55)-(2.57) are nonlinear viscous damping terms. They contribute significantly when the low frequency yaw rates and sway velocities are high such as in a tight turning circle maneuver.

Propeller Thrust Force

The thrust model used in the current method is the one presented in *Son and Nomoto* (1981). The thrust force is given by

$$T_{prop} = (1 - t) \rho n^2 D^4 K_T \tag{2.66}$$

where T_{prop}, t, n, D and K_T are the propeller thrust force, the thrust-deduction fraction, propeller revolutions per second, propeller diameter, and thrust coefficient, respectively. The thrust coefficient, K_T is expressed as a linear function of the advance ratio, J

$$K_T = 0.527 - 0.455 J \tag{2.67}$$

$$J = u_P^{\prime} U_{net} / nD \tag{2.68}$$

where u'_P represents the effective wake fraction given by

$$u'_P = \cos v'[(1 - w_p) + \tau(v' + x'_p r')^2] \tag{2.69}$$

where w_p is the wake fraction in straight-ahead condition, v' and r' are the non-dimensional sway and yaw velocities, x'_p is the x-location of the propeller plane, and τ is a parameter to account for the lateral velocity components.

Calm water Resistance

The calm water resistance is estimated according to the quadratic curve fit for low Froude numbers, given in *Son and Nomoto* (1981)

$$X(u) = X'_{u|u|} 0.5 \rho L^2 u|u| \tag{2.70}$$

where $X'_{u|u|}$ is the total calm water resistance coefficient at model scale set at a constant value of $X'_{u|u|} = -0.0004226$ for the containership S-175. This model is deemed sufficient for the low Froude number, $F_n = 0.15$, that is used for the maneuvering simulations in the present research. Consistent with the definition of all body velocities, u represents the instantaneous velocity which includes both the oscillatory as well as the time varying mean component. This implies that the model also accounts for the viscous surge oscillatory damping in addition to the steady calm resistance. This model is tested and validated in Chapter VI for the Wigley-I hull by comparing with results obtained from CFD.

Control Forces

The hydrodynamic forces acting on the ship due to rudder action is modeled according to *Son and Nomoto* (1981) and is written as follows:

$$X_{Rudder} = c_{RX} F'_N \sin\delta' \tag{2.71}$$

$$Y_{Rudder} = (1 + a_H) F'_N \cos\delta' \tag{2.72}$$

$$K_{Rudder} = -(1 + a_H) F'_N \cos\delta' \times z'_R \tag{2.73}$$

$$N_{Rudder} = (1 + a_H(x'_H/x'_R)) F'_N \cos\delta' \times x'_R \tag{2.74}$$

where X_{Rudder}, Y_{Rudder}, K_{Rudder}, and N_{Rudder} are the non-dimensional rudder forces in surge, sway, roll and yaw respectively. Variables δ', x'_R, and z'_R represent the rudder angle, and the x- and z-directional centre of normal force acting on the rudder, respectively. Parameters c_{RX}, a_H, and x'_H represent the interaction of the hull and rudder which can be obtained experimentally or through empirical methods. The rudder normal force F'_N is expressed as follows:

$$F'_N = -\frac{6.13\Lambda}{\Lambda + 2.25} \cdot \frac{A_R}{L^2} ({u'_R}^2 + {v'_R}^2) \sin\alpha_R \tag{2.75}$$

$$\alpha_R = \delta + \tan^{-1}(v'_R/u'_R) \tag{2.76}$$

here A_R and Λ represent the area and aspect ratio of the rudder, respectively. α_R, u'_R, and v'_R represent the effective inflow angle, and the x- and y- components of the effective inflow velocity into the rudder, respectively. The effective inflow speed and angle are affected by the hull wake, the flow straightening effect of the hull, propeller and ship motions. In the presence of incident waves, the wave particle velocities could also have a significant effect on the rudder forces. To account for these effects, semi-empirical formulas are used. In the current method, the experimental data and coefficients used in *Son and Nomoto* (1981) for the calm water condition are used.

CHAPTER III

Numerical Techniques

3.1 Source Distribution Formulation

The mixed boundary value problem introduced in Chapter II has to be solved for the perturbation potentials ϕ_R and ϕ_D and their derivatives. In the present work, a source distribution technique is used. Desingularised sources are placed above the free surface node and constant strength panels are used on the body. The potential at any point on the fluid is then given by:

$$\phi_i = \sum_{S_F} \sigma_j G(\mathbf{x_i}; \boldsymbol{\xi_j}) + \int_{S_B} \sigma_j G(\mathbf{x_i}; \boldsymbol{\xi_j}) dl \tag{3.1}$$

where,

$$\begin{aligned}
\phi_i &= \text{velocity or acceleration potential} \\
\mathbf{x_i} &= \text{field point anywhere in the domain} \\
\boldsymbol{\xi_j} &= \text{location of a source point} \\
\sigma_j &= \text{source strength of source point} \\
S_B &= \text{instantaneous hull contour} \\
S_F &= \text{free surface contour} \\
G(\mathbf{x_i};\boldsymbol{\xi_j}) &= \text{Rankine source Green function, given by} \\
&= \ln r \\
r &= |\mathbf{x_i} - \boldsymbol{\xi_j}| \quad \text{(the distance between a field point and a source point)}
\end{aligned}$$

The first term on the RHS of Equation (3.1) is the contribution of the isolated desingularised free surface sources and the second term the influence from the panels on the body.

Applying the Dirichlet and Neumann boundary conditions on the free surface and body respectively, and using Equation (3.1), the integral is discritized to form a system of linear equations to be solved for the source strengths σ_j.

$$\sum_{S_F} \sigma_j \ln|\mathbf{x_i} - \boldsymbol{\xi_j}| + \int_{S_B(t)} \sigma_j \ln|\mathbf{x_i} - \boldsymbol{\xi_j}| dl = \phi_i \quad \mathbf{x_i} \in S_F \tag{3.2}$$

$$\sum_{S_F} \sigma_j \frac{\partial \ln|\mathbf{x_i} - \boldsymbol{\xi_j}|}{\partial N} + \int_{S_B(t)} \sigma_j \frac{\partial \ln|\mathbf{x_i} - \boldsymbol{\xi_j}|}{\partial N} dl = \frac{\partial \phi_i}{\partial N} \quad \mathbf{x_i} \in S_B \tag{3.3}$$

These equations (3.2) and (3.3) can be written in discritized matrix form, $A_{ij}\sigma_j{=}b_i$, where A_{ij} is the influence matrix, which is determined from the LHS of the equations, σ_j are the unknown source strengths, and b_i the RHS of the equations. The matrix is inverted using a LU decomposition technique.

Once the source strengths are determined, the potentials and their derivatives are determined on the body and free surface.

3.2 Domain Discretization

Body panelization

The body is modeled using flat panels as they are more capable of handling complex body geometries. The hull offsets are read from an input file and then each station is curve fitted using a cubic spline. The sections are then panelized based on the body resolution specified.

The body panel size is fixed for the entire simulation, i.e the panelization is done only once, using a preprocessor. This also ensures that the size of the body panels are maintained about the same order of magnitude as that of the free surface resolution. This also implies that as the sections translate and rotate relative to the water surface, the number of panels on the body change.

Free Surface Discretization

On the free surface, desingularised sources are distributed above the free surface nodes. The desingularization distance, L_d is given by

$$L_d = l_d \Delta s^{\alpha} \tag{3.4}$$

where l_d is set to 3.0 and α to 0.5 based on the study by *Cao et al.* (1991). Here Δs represents the area of the mesh in 3-D. In the present formulation, Δs is set to be the internodal spacing on the free surface and scaled by the body panel size.

The free surface is divided into two segments, the inner region which resolves the waves and an outer region representing the numerical beach. The length of the domain is set based on the wavelength of the incident waves or the radiated waves

in the case of forced oscillatory problems. Typically for the frequencies spanning the normal seakeeping range, two wavelengths are used for the inner region and two wavelengths for the beach on each side of the station. To resolve the radiated waves, the number of nodes used per wavelength is usually $\frac{\lambda}{30}$. To avoid the influence of the singular point on the corner of the body-free surface intersection, the first free surface node is placed twice the body panel size away from the centre of the nearest body panel.

The numerical beach is important to satisfy the far field boundary condition and ensure there are no wave reflections. It is thus a crucial element to performing stable long time simulations. The details of the beach will be discussed in Section 3.3.

3.3 Time Integration

The free surface elevation and potentials are evolved in time by integrating the free surface boundary conditions given by Equations (2.17) and (2.18). In the body exact formulation, as the body moves relative to the water surface, it is to be ensured that it does not crash into the free surface nodes. To do this, all the free surface nodes on each station are displaced such that the distance between the first free surface node and the nearest body panel is constant. The rate at which they are displaced would be the component of the body velocity relative to the hydrodynamic frame, resolved along the calm water surface. This is called the "moving node velocity". The integrations are done by following the nodes on the free surface, hence would include the contribution of the moving node velocity.

$$\frac{\delta\eta}{\delta t} = \frac{\partial\phi}{\partial z} + V\frac{\partial\eta}{\partial y} + x_h\dot{\psi}\frac{\partial\eta}{\partial y} + v_m\frac{\partial\eta}{\partial y} - \mu\eta \qquad \text{on z} = 0 \tag{3.5}$$

$$\frac{\delta\phi}{\delta t} = -g\eta + V\frac{\partial\phi}{\partial y} + x_h\dot{\psi}\frac{\partial\phi}{\partial y} + v_m\frac{\partial\phi}{\partial y} - \mu\phi \qquad \text{on z} = 0 \tag{3.6}$$

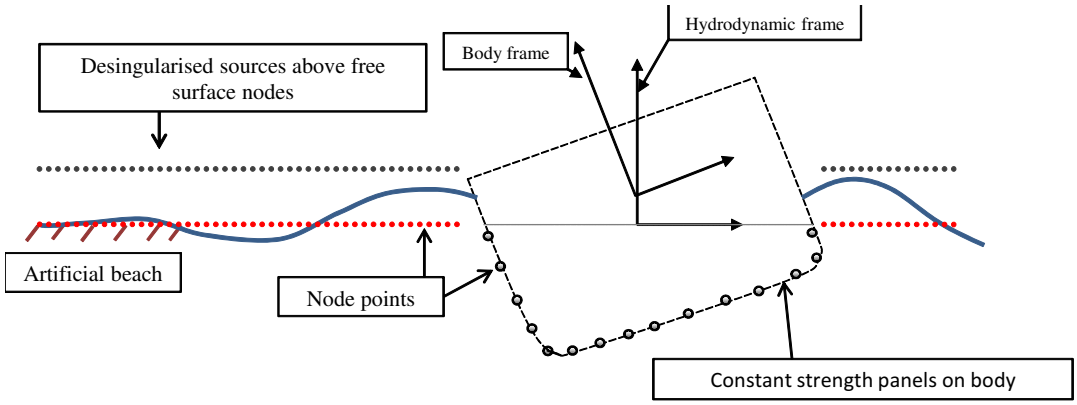

Figure 3.1: DETAILS AT A GIVEN STATION

Here $\frac{\delta}{\delta t}$ refers to the time derivative taken by following a free surface node. v_m is the velocity of the moving node. The last terms in the equations (3.5) and (3.6) are the damping terms that are added to generate artificial damping at the beach.

The beach is based on the work by *Cointe et al.* (1990). The damping coefficient μ is given by

$$\mu(y) = \alpha\omega \left(\frac{y - y_0}{\lambda} \right)^2, \quad y_0 \leq y \leq y_0 + \beta\lambda \tag{3.7}$$

where y_0 is the location of the start of the beach, ω and λ are the angular frequency and wavelength of the incident or radiated waves. The parameters α and β are used to tune the strength of damping and length of the damping zone respectively. Based on the study by *Tanizawa* (1996), the optimum value of α was arrived at $\alpha = 1$ and the minimum length of the damping zone required to minimize reflections was one wavelength. In the current method, α is set to 1 and $\beta = 2$.

To numerically integrate the free surface equations (3.5) and (3.6) and the rigid body equations (2.33) and (2.34), an explicit fourth-order Adams-Bashforth scheme is used

$$F^{n+1} = F^n + \frac{\Delta t}{24}(55{F_t}^n - 59{F_t}^{n-1} + 37{F_t}^{n-2} - 9{F_t}^{n-3}) \tag{3.8}$$

where F denotes the function being numerically integrated, F_t is the time-derivative,

and the superscripts indicate the time level at which they are evaluated. The quantities that are integrated using the scheme are $F = \phi, \eta$ on the free surface and $F = \boldsymbol{v}, \boldsymbol{\xi}$ for body equations of motion. To obtain the spatial derivatives, $\frac{\partial \eta}{\partial y}$ and $\frac{\partial \phi}{\partial y}$, of η and ϕ, respectively, a central difference scheme is used. For the nodes at the ends, one sided differencing is used.

The time-step size is set based on the period of the wave. Typically the values of Δt used are in the range of $T/200$ to $T/100$. It also depends on the spatial resolution of the free surface. Numerical instabilities can occur if Δt is chosen to be too large. The general guideline used here is based on the stability criterion described in *Park and Troesch* (1992) and *Wang and Troesch* (1997)

$$S = \pi g \Delta t^2 / \Delta x \tag{3.9}$$

where S is the stability index dependent on the spatial discretization Δx and time-step size Δt. It is in general dependent on the type of boundary condition and the integration scheme. As a conservative estimate, the value of $S \leq 1$ is used to ensure a stable free surface throughout the computations.

3.4 Blending Scheme

The present formulation uses a blended approach to ensure computational efficiency while capturing essential nonlinearities. The free surface boundary conditions are linearized while the degree of nonlinearity accounted for in the body boundary conditions depend on the choice of the blending scheme.

In the present formulation, the incident wave force and the hydrostatic loads are computed up to the intersection between the body position and exact incident wave surface. For solving the radiation and diffraction problems, the corresponding pressure components are integrated up to the intersection of the mean free surface

and the exact instantaneous body surface.

The body-exact approach also has the ability to allow sections to completely emerge out of the water surface and re-enter. This is possible if either the stations are shallow or the wave amplitudes get large. There are two ways to handle the situation. The computations can be stopped for the particular station and re-initialize the values of ϕ, $\frac{\partial \phi}{\partial t}$ to zero. The other approach is to continue the free surface evolution even as the body is out of water. In the present method, the former approach is implemented. This can lead to impact loads especially for ships with transom sterns.

3.5 Radial Basis Functions

The first order derivative $\frac{\partial \phi}{\partial x}$ and higher order derivatives $\frac{\partial^2 \phi}{\partial x \partial y}$ and $\frac{\partial^2 \phi}{\partial x \partial z}$ are required to be evaluated in the body boundary conditions for the acceleration potential in equations (2.42) and (2.43). This is approximated using radial basis functions (RBF).

Once the two-dimensional BVP is solved on each station, a scalar quantity Φ at any point on the body can be expressed as a function of the Euclidean distance from the other nodes.

$$f_j(\mathbf{x_i}) \equiv f(|\mathbf{x_i} - \mathbf{x_j}|) \tag{3.10}$$

$$\Phi(\mathbf{x_i}) = \sum_{j=1}^{N} \alpha_j f_j(\mathbf{x_i}) + \alpha_{N+1} \tag{3.11}$$

$$\sum_{j=1}^{N} \alpha_j = 0 \tag{3.12}$$

where f is the basis function. The last equation is a constraint on α_j to ensure uniqueness. The quantity Φ represents the scalar on which the x-derivative is to be evaluated namely, ϕ, $\frac{\partial \phi}{\partial y}$ and $\frac{\partial \phi}{\partial z}$.

The expansion coefficients are found by setting up a system of $N + 1$ equations,

such that

$$P = \begin{bmatrix} 1 \\ \vdots \\ 1 \end{bmatrix} \in \mathbf{R}^N$$

$$F = \begin{bmatrix} f_1(\mathbf{x_1}) & \cdots & f_N(\mathbf{x_1}) \\ \vdots & f_j(\mathbf{x_i}) & \vdots \\ f_1(\mathbf{x_N}) & \cdots & f_N(\mathbf{x_N}) \end{bmatrix} \in \mathbf{R}^{N \times N}$$

$$H = \begin{bmatrix} F & P \\ P^T & 0 \end{bmatrix} \in \mathbf{R}^{(N+1)\times(N+1)}$$

These equations can be rewritten in a compact matrix form as

$$H_{ij}\alpha_j = \Phi_i \tag{3.13}$$

with $\Phi_{N+1} = 0$. The interpolation expansion coefficients can be found after the matrix inversion

$$\alpha_j = [H_{ij}]^{-1}\Phi_i$$

These coefficients are used to interpolate the data in three-dimensional space and to find the derivatives at any point. The x-derivative is determined by taking the partial derivative of the basis function with respect to the x-direction.

$$\frac{\partial \Phi(\mathbf{x_i})}{\partial x} = \sum_{j=1}^{N} \alpha_j \frac{\partial f_j(\mathbf{x_i})}{\partial x}$$

Different forms of the basis functions were extensively tested by *Bandyk* (2009) for

maximum accuracy and stability of the partial derivatives by comparing with known analytical results. The form that was finally arrived at and used in the present work is

$$f_j(\mathbf{x_i}) = e^{-\frac{|\mathbf{x_i}-\mathbf{x_j}|^{1.5}}{{c_j}^{1.5}}} \tag{3.14}$$

CHAPTER IV

Free Motion Drift

The computer code for the present work is built on the body-exact strip theory method by *Bandyk* (2009), where the body is restricted to travel in a rectilinear forward path. Fundamental departure from the work involve setting up the BVP in the rotating and translating hydrodynamic frame and incorporating the damping beach to carry out long time simulations. The acceleration potential formulation, though based on the previous work, has been re-derived and modified for the present methodology. Other changes include curve-fitting the input hull geometry to improve accuracy, new algorithms to determine hull-free surface intersection locations and keep track of the three coordinate frames used, and incorporation of models for the propeller thrust, hull resistance, viscous forces and rudder forces. The present code has been tested for its seakeeping prediction capabilities and compared with the results obtained from experiments and *Bandyk* (2009). The results compare favorably in general. Extensive results for a variety of hull forms for the hydrodynamic coefficients and response amplitude operators (RAO) are presented and compared against experiments and other research groups in *Bandyk* (2009).

As a first stage of the research, the free motion drifting of a ship in the presence of waves are simulated. This represents the scenario of a ship that has lost power and control, and is at the mercy of the waves. These simulations show some interesting

results for the course, the drift speed and final stable steady state orientation of the vessel with respect to the waves.

The simulations are done for two vessels, the Wigley-I hull and the containership S-175. The Wigley-I hull is a mathematical hull form that is commonly used for analytical and numerical research. The hull form has parabolic stations and waterlines, and is fore and aft symmetric.

$$\frac{\eta(x,z)}{L} = \frac{B}{2L}\left(1-\left(\frac{z}{T}\right)^2\right)\left(1-\left(\frac{2x}{L}\right)^2\right) \quad \text{Wigley-I hull surface} \tag{4.1}$$

where L, B, and T are the length, breadth and draft of the hull, respectively. The second ship on which the free motion simulations are performed, is the containership S-175, which has a bulbous bow and a transom stern section. There exists extensive experimental data in literature for the S-175 and it is widely used by research groups for benchmarking computational methods. The hull particulars are given in Table 4.1.

Based on the results of the convergence tests given in Appendix A, the computational domain size for each station is set to two wavelengths of the incident wave with an additional two wavelengths for the beach. The number of panels per station on the body is set to 50. On the free surface, 30 nodes are used per wavelength to resolve the waves, and a time step size of $T/200$ is used for the numerical integration of the free surface boundary conditions and nonlinear Euler EOM.

In all the simulations results presented here, the propeller and rudder modules are turned off. The drag force in surge is calculated based on the assumption that the drift speeds are small enough that the vessel only has frictional resistance from the fluid. The value of c_f, the skin friction coefficient is calculated based on the $ITTC'57$

	Wigley-I	**S-175**
LBP[m]	3.0	175.0
B[m]	0.3	25.4
T[m]	0.1875	9.5
S[$\mathbf{m^2}$]	1.3385	5540
$\mathbf{C_W}$	0.6886	0.7080
$\mathbf{C_B}$	0.5571	0.5714

Table 4.1: HULL PARTICULARS

friction line for a flat plate

$$c_f = \frac{0.075}{[\log_{10}(R_n) - 2]^2} \tag{4.2}$$

where R_n is the Reynold's number of the vessel. A form factor of 1.15 is used based on empirical calculations. The simulations are performed with and without sway and yaw viscous forces. The viscous forces are modeled using the empirical coefficients of *Clarke et al.* (1983), as given in Section 2.9.

Discussion

Wigley-I

The Figure 4.1 shows the first of the results for the free motion drift simulation of the Wigley-I hull. As shown in 4.1(c), the waves are incident at an angle of 45^o wrt the positive x-axis of the earth fixed frame, x_e. The wave slope is fairly steep at $H/\lambda = 1/50$ and wavelength is set equal to ship length. At $t = 0$, the ship is aligned with x_e with bow pointing in positive x_e. At $t = 0$, the waves are turned on. A brief ramp of 2 periods is used to get to full wave height. Here no viscous forces in sway and yaw are modeled.

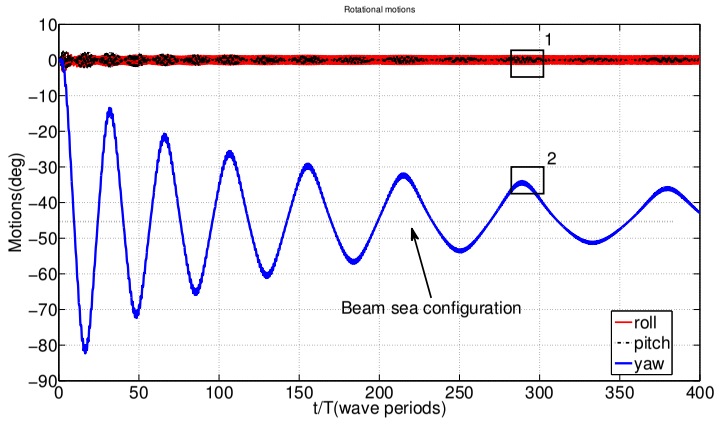

(a) Time history of yaw motions

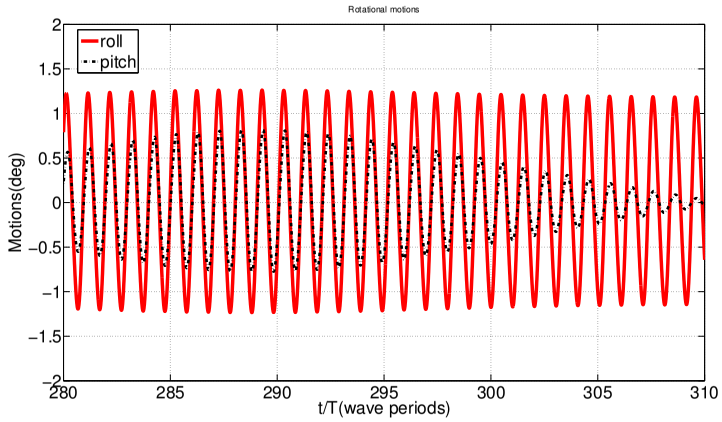

(b) Details of roll and pitch motions from inset 1

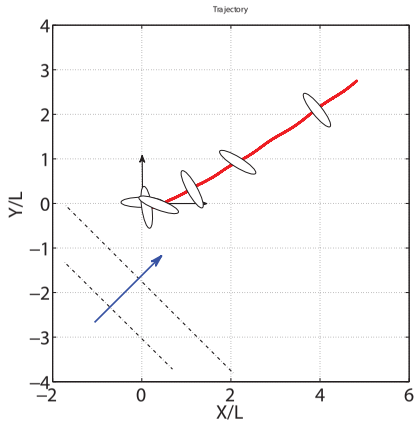

(c) Track of ship

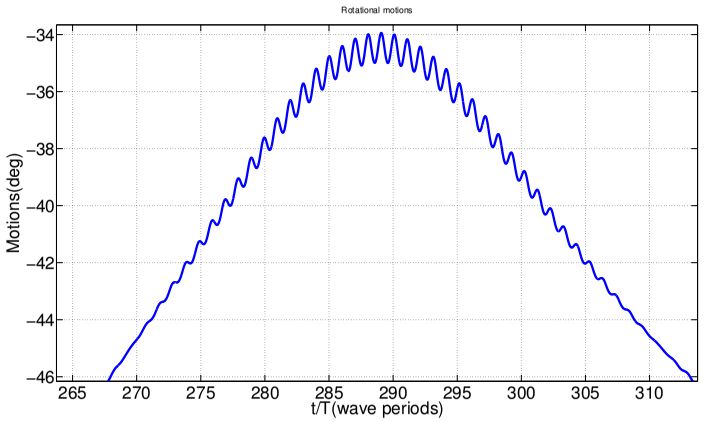

(d) Details of yaw motions from inset 2

Figure 4.1: FREE MOTION DRIFT OF WIGLEY-I, $\lambda/L = 1.0$, $H/\lambda = 1/50$, WAVE DIRECTION= 45^o, NO SWAY-YAW VISCOUS FORCES

Figure 4.1(a) shows the time history of the yaw motions. The vessel quickly yaws from its initial orientation and enters into a series of long period slowly varying oscillations. The oscillations have a mean of -45^o, which corresponds to the orientation of the ship when it is at beam seas to the incoming waves. The beam sea configuration is defined as the orientation when the ship is aligned normal to the direction of incident waves. This seems intuitive from the fact that the Wigley-I is a fore and aft symmetric vessel. The interesting feature is that superimposed on this low-frequency oscillations, is the high-frequency wave response of the ship. This is shown via insets (1) and (2), in Figure 4.1(b) and 4.1(d) which show the final steady state details of roll, pitch and yaw, respectively. Figure 4.1(c) shows the track of the centre of gravity of the ship. It also shows the orientation of the vessel at different times as it is drifting down wave.

The inclusion of the sway and yaw viscous forces, dramatically change the results. As can be seen from Figure 4.2, the additional viscous damping reduces the overshoot of the slowly varying yaw response and quickly brings the vessel to a stable equilibrium configuration. The steady state orientation has changed from being beam seas to about 10^o away from the expected beam sea configuration, bow into the waves. This could be the effect of the change in the force balance between the 2^{nd} order wave drift forces, potential damping forces and viscous forces. This is reflected in the trajectory of the ship, as seen in Figure 4.2(b), where the ship is drifting almost along the direction of the wave fronts. The results could also be the effect of the "double-counting" issue mentioned in Section 2.9, where part of the lift forces in the hydrodynamic derivatives $Y_j, N_j (j = v, r)$ are being accounted for by the potential forces.

The effects of the change in wave heading, slope and frequency is shown in Figures 4.3-4.5. All the simulations are done with viscous forces in sway and yaw. The final steady state orientation of the vessel is between 10^o and 15^o away from the beam

sea configuration, depending on the incident wave parameters. It is to be mentioned that in the case of head seas, with the vessel starting off in an unstable equilibrium position, a small perturbation is given to the wave heading (made 179.95^o) to kickstart the free motions.

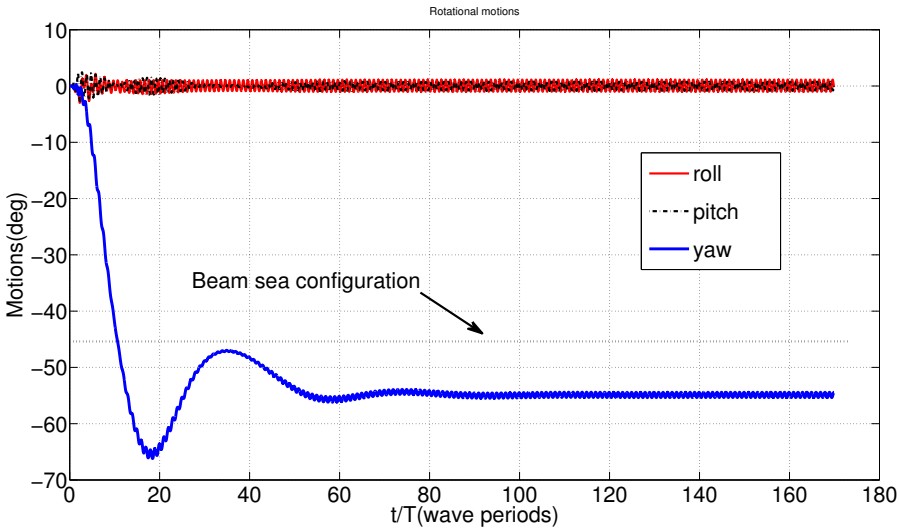

(a) Time history of yaw motions

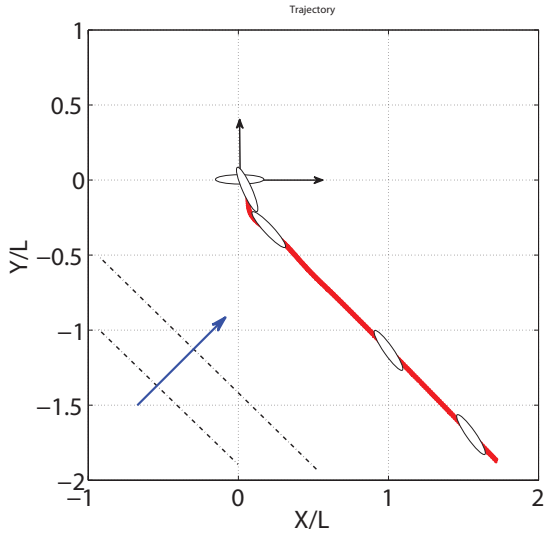

(b) Track of ship

Figure 4.2: FREE MOTION DRIFT OF WIGLEY-I, $\lambda/L = 1.0$, $H/\lambda = 1/50$, WAVE DIRECTION= 45^o, WITH SWAY-YAW VISCOUS FORCES

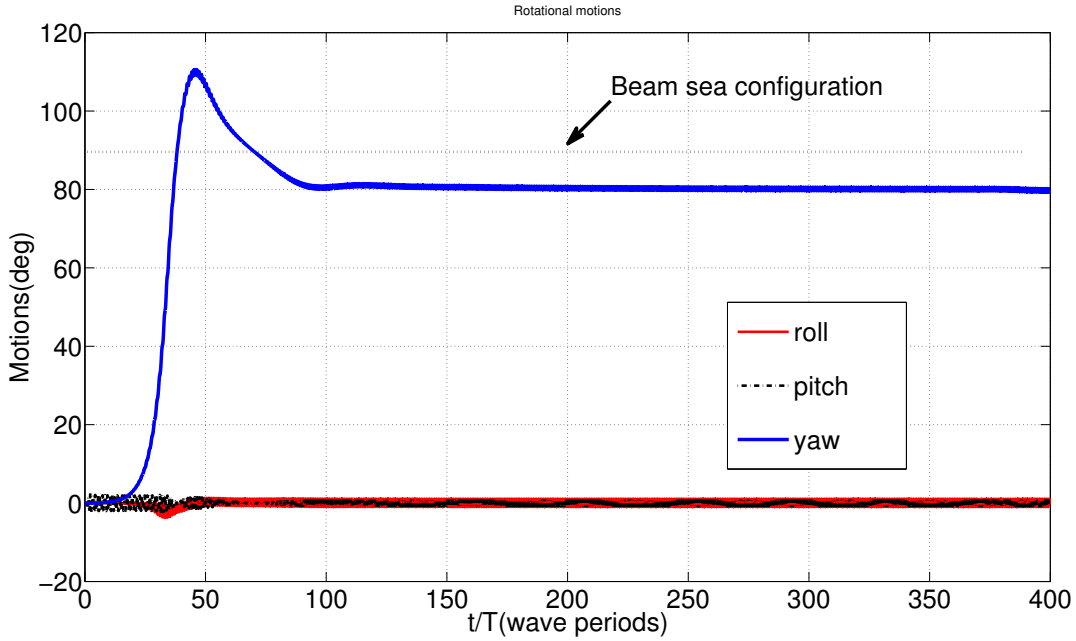

(a) Time history of yaw motions

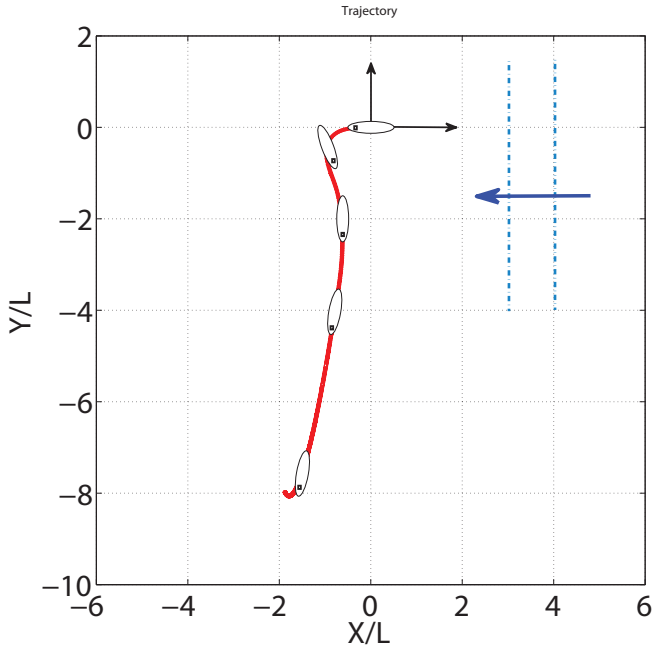

(b) Track of ship (dot represents aft of the ship)

Figure 4.3: FREE MOTION DRIFT OF WIGLEY-I, $\lambda/L = 1.0$, $H/\lambda = 1/50$, WAVE DIRECTION = HEAD SEAS, WITH SWAY-YAW VISCOUS FORCES

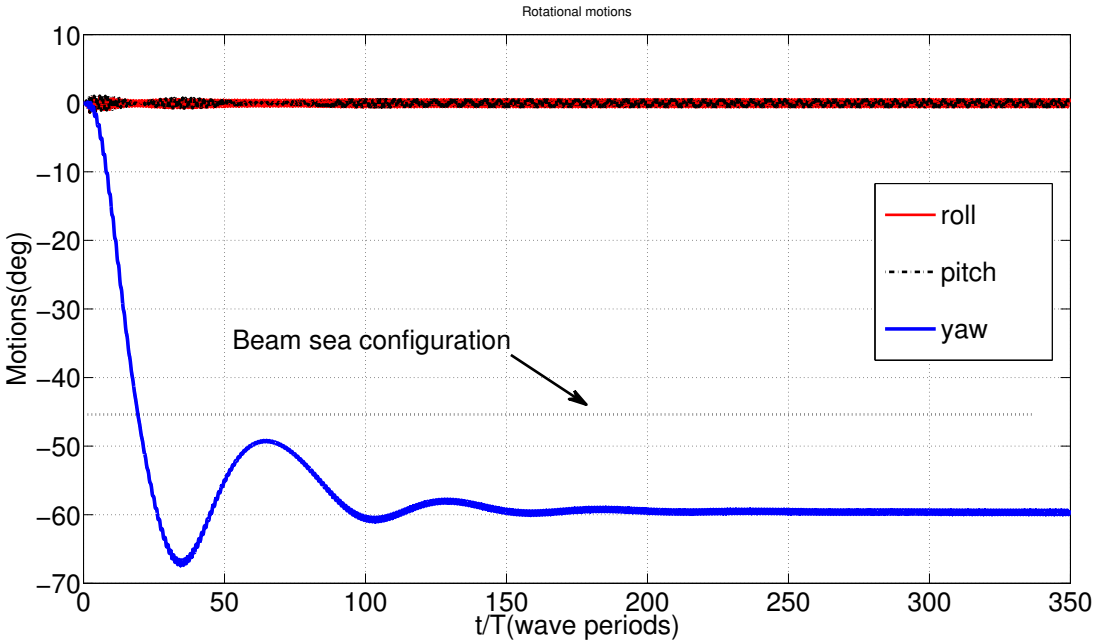

(a) Time history of yaw motions

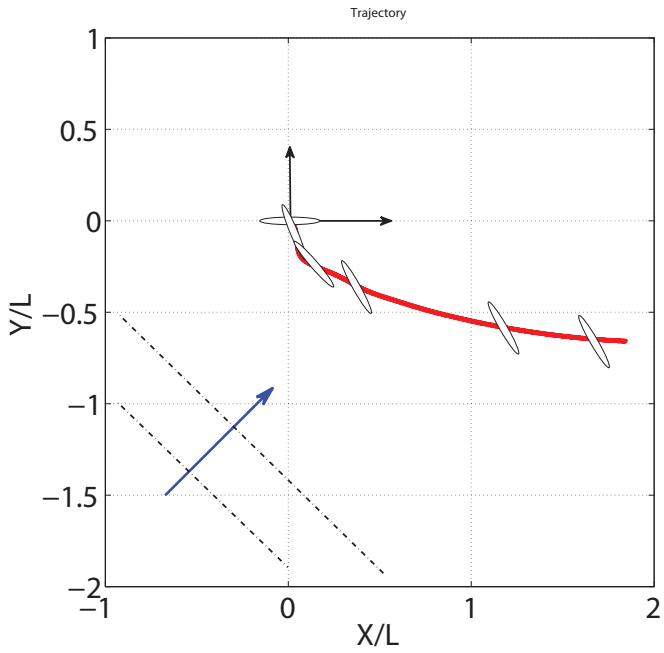

(b) Track of ship

Figure 4.4: FREE MOTION DRIFT OF WIGLEY-I, $\lambda/L = 1.0$, $H/\lambda = 1/100$, WAVE DIRECTION= 45^o, WITH SWAY-YAW VISCOUS FORCES

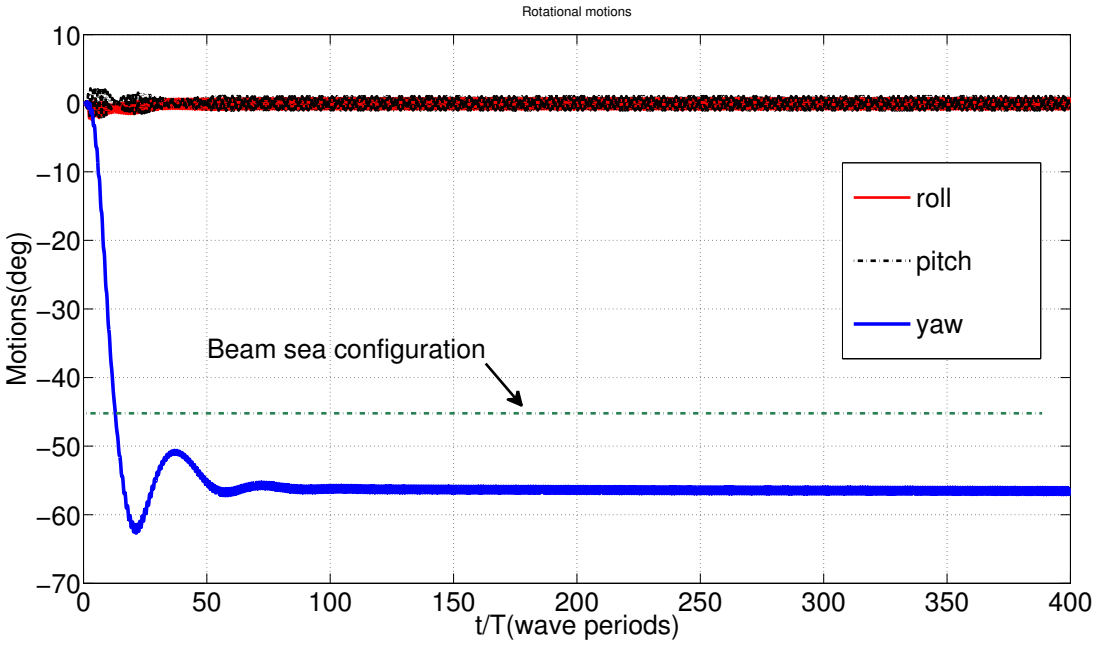

(a) Time history of yaw motions

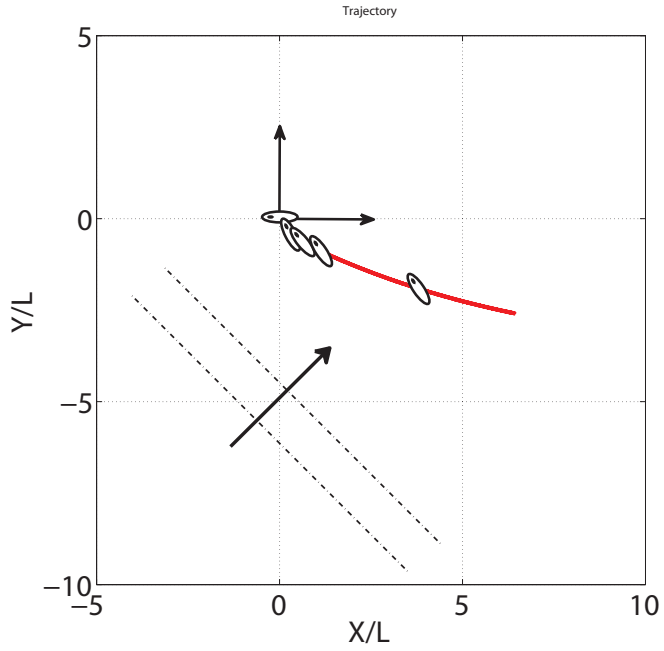

(b) Track of ship (dot represents the aft of the ship)

Figure 4.5: FREE MOTION DRIFT OF WIGLEY-I, $\lambda/L = 0.7$, $H/\lambda = 1/50$, WAVE DIRECTION= 45^o, WITH SWAY-YAW VISCOUS FORCES

S-175

The first of the free motion drift simulations of the containership S-175 is shown in Figure 4.6. No viscous sway-yaw forces are modeled. As with all the simulations, the ship is aligned at $t = 0$ with the positive x_e axis. Waves are incident at 45^o wrt x_e. The ship quickly changes its orientation from the initial configuration and after a couple of overshoots past the beam sea configuration, enters into the slowly varying response in a similar manner to the Wigley-I responses. Because of the fore and aft asymmetry of the hull, the mean of the final stable state configuration is about -30^o wrt x_e. This is about 15^o away from the beam sea configuration, with the stern into the waves. This is also evident from Figure 4.6(c), showing the track of the ship with the orientations superimposed at different instances in time. Figures 4.6(b) and 4.6(d) show the details of the first order responses.

The effect of including sway and yaw viscous forces is seen in Figure 4.7. As with the response of the Wigley-I, the overshoot is dampened down by 10^o and the ship settles quickly to a stable state configuration of about -62^o wrt x_e. It is interesting to note that the new equilibrium is about 17^o away from the beam sea configuration, with bow into the waves. This also has an effect on the track of the ship as seen in Figure 4.7(b), where the ship is drifting into the waves.

The effects of change in wave heading, slope and frequency is see seen in Figures 4.8 through 4.11. All the simulations are done with the sway and yaw viscous effects on. The final steady state orientation of the vessel is between 15^o and 17^o away from the beam sea configuration with bow into the waves, depending on the wave characteristics.

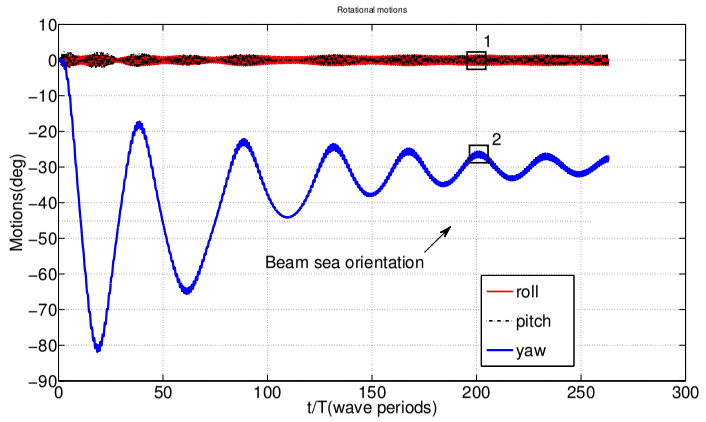

(a) Time history of yaw motions

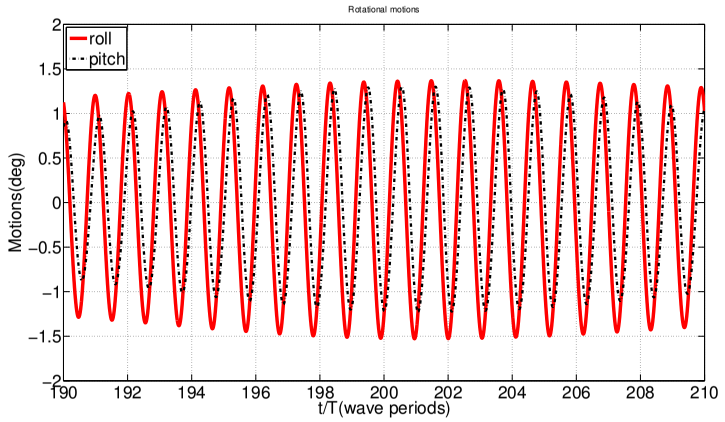

(b) Details of roll and pitch motions from inset 1

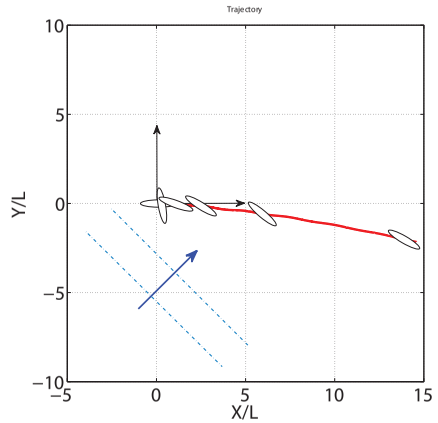

(c) Track of ship

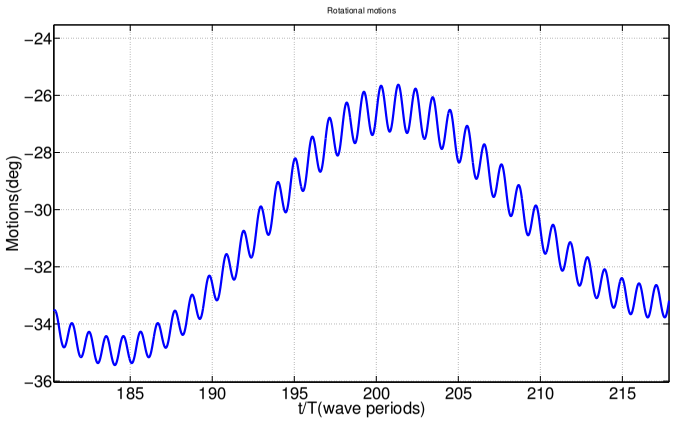

(d) Details of yaw motions from inset 2

Figure 4.6: FREE MOTION DRIFT OF S-175, $\lambda/L = 1.0$, $H/\lambda = 1/50$, WAVE DIRECTION= 45^o, NO SWAY-YAW VISCOUS FORCES

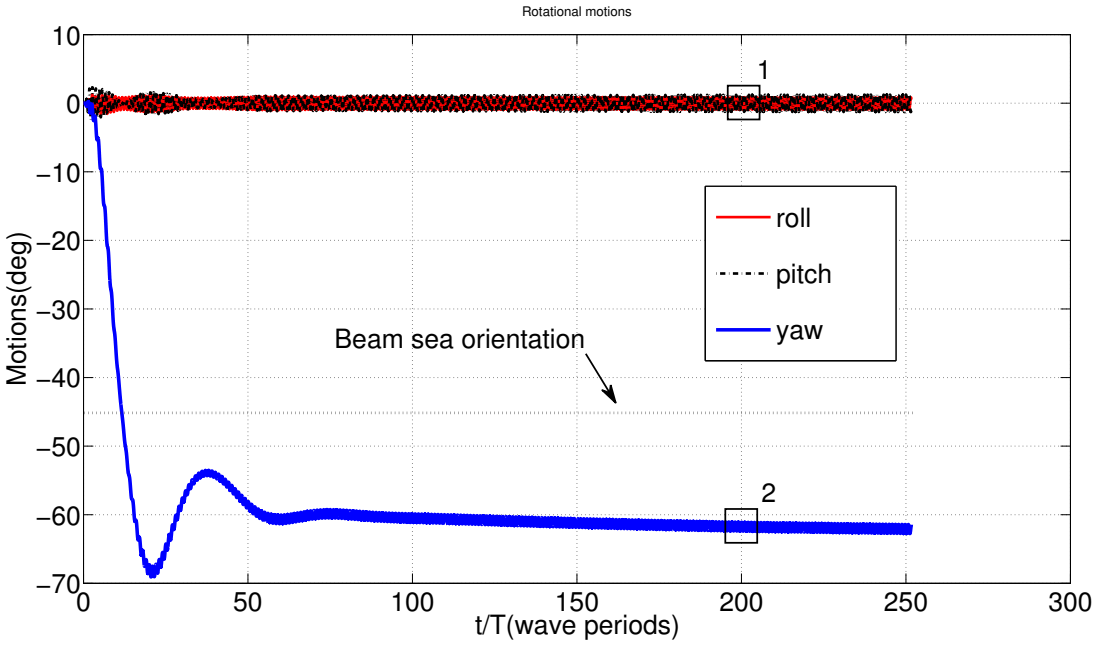

(a) Time history of yaw motions

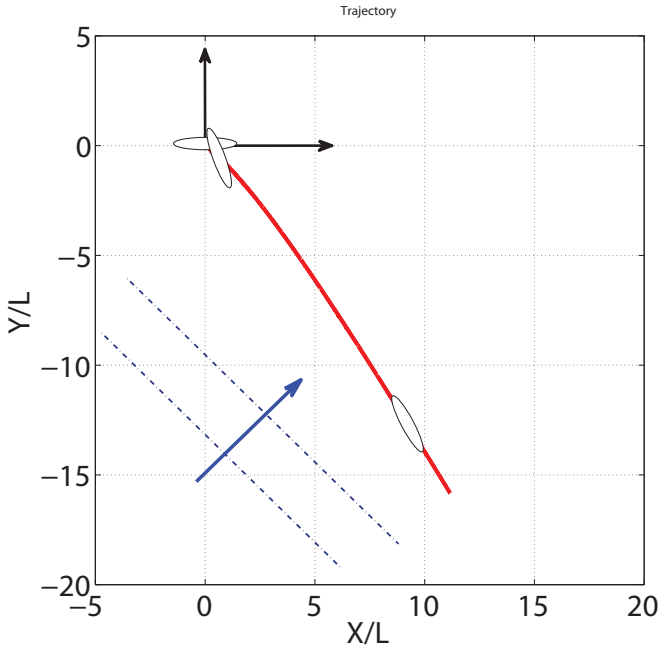

(b) Track of ship

Figure 4.7: FREE MOTION DRIFT OF S-175, $\lambda/L = 1.0$, $H/\lambda = 1/50$, WAVE DIRECTION= 45^o, WITH SWAY-YAW VISCOUS FORCES

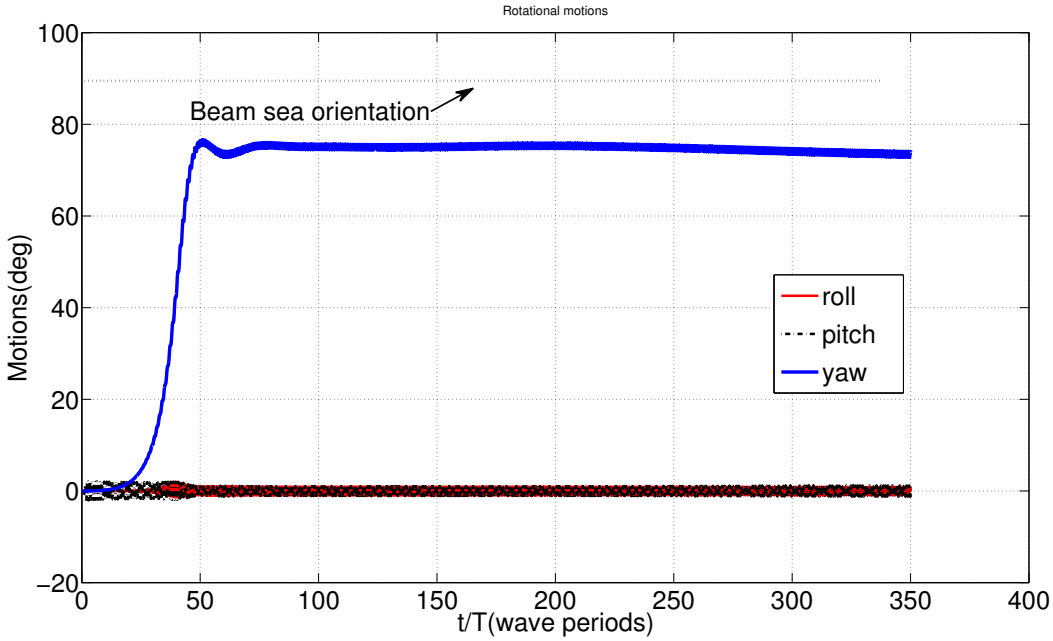

(a) Time history of yaw motions

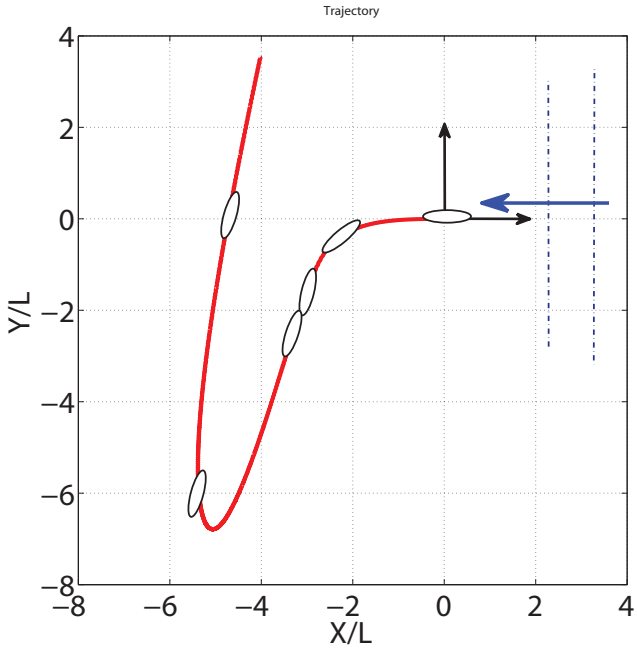

(b) Track of ship

Figure 4.8: FREE MOTION DRIFT OF S-175, $\lambda/L = 1.0$, $H/\lambda = 1/50$, WAVE DIRECTION= 180^o, WITH SWAY-YAW VISCOUS FORCES

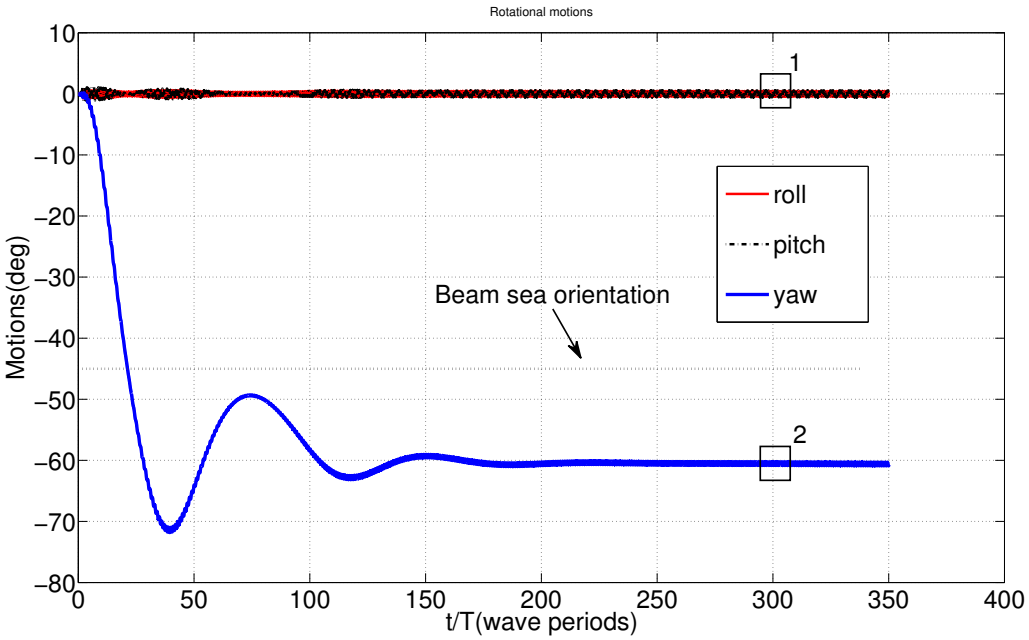

(a) Time history of yaw motions

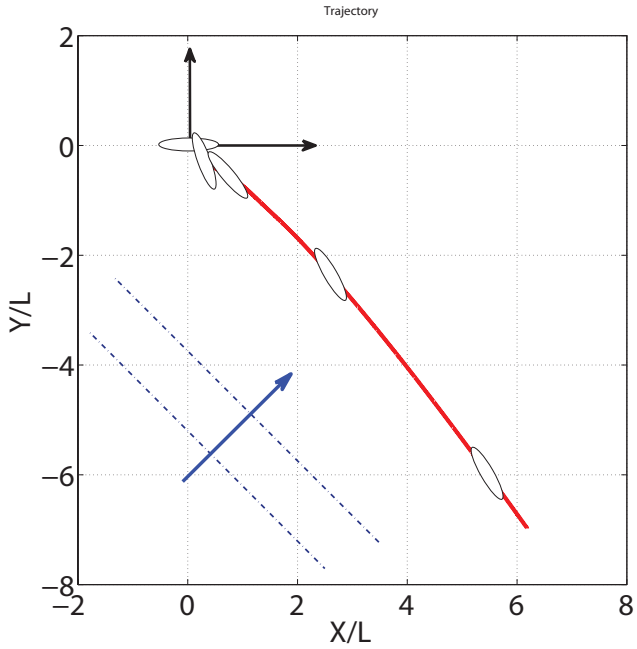

(b) Track of ship

Figure 4.9: FREE MOTION DRIFT OF S-175, $\lambda/L = 1.0$, $H/\lambda = 1/100$, WAVE DIRECTION= 45^o, WITH SWAY-YAW VISCOUS FORCES

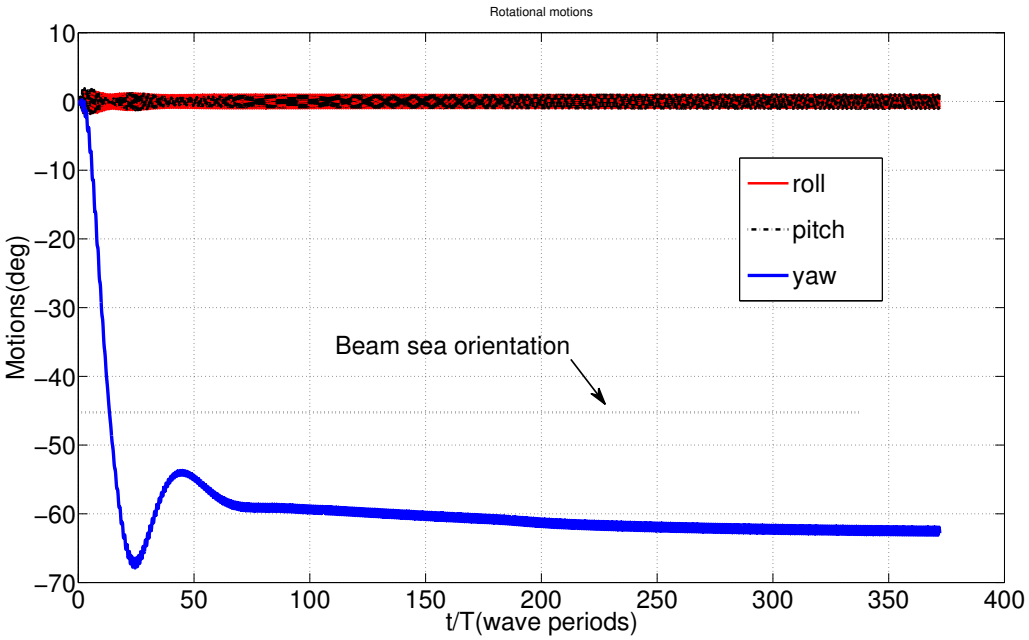

(a) Time history of yaw motions

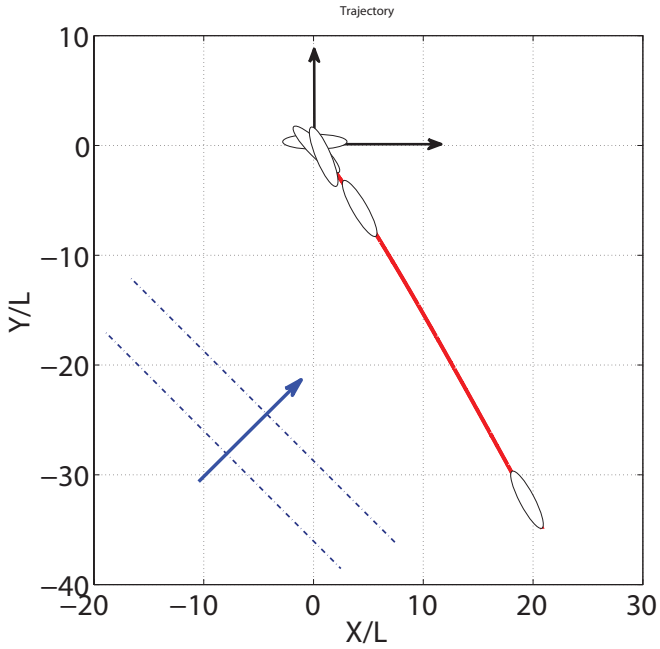

(b) Track of ship

Figure 4.10: FREE MOTION DRIFT OF S-175, $\lambda/L = 1.2$, $H/\lambda = 1/60$, WAVE DIRECTION= 45^o, WITH SWAY-YAW VISCOUS FORCES

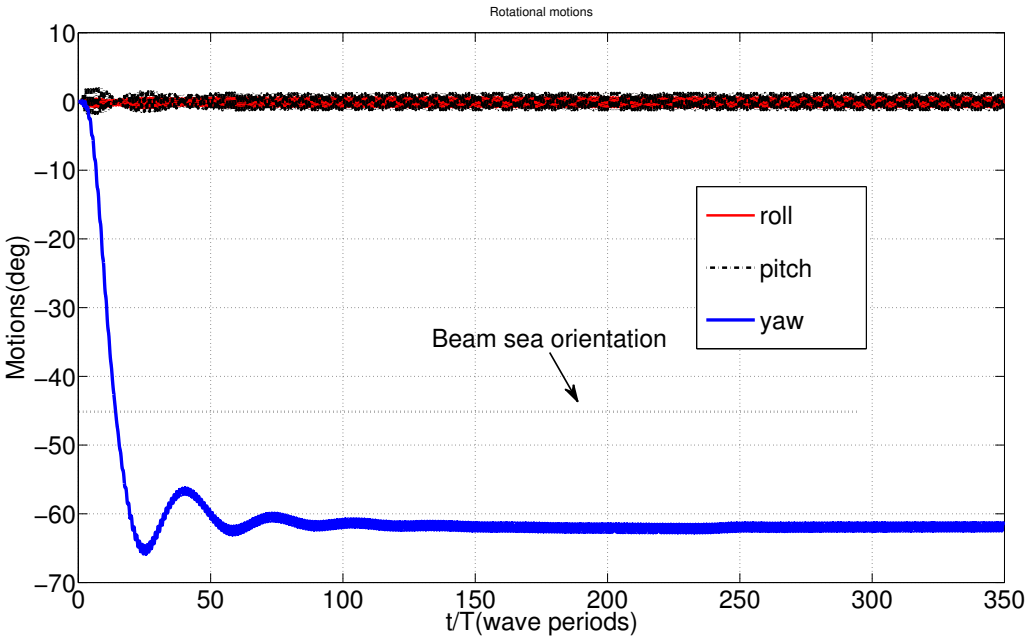

(a) Time history of yaw motions

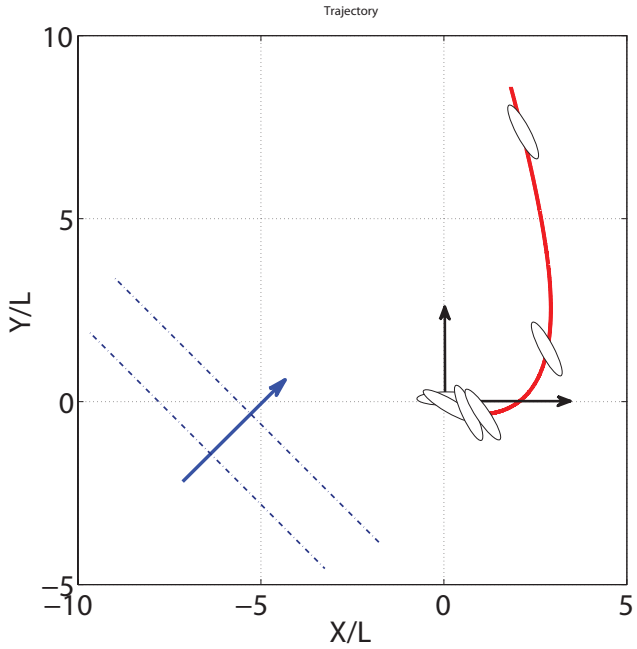

(b) Track of ship

Figure 4.11: FREE MOTION DRIFT OF S-175, $\lambda/L = 0.7$, $H/\lambda = 1/50$, WAVE DIRECTION= 45^o, WITH SWAY-YAW VISCOUS FORCES

CHAPTER V

Maneuvering Results

The turning circle maneuvers of the containership S-175 are simulated in calm water and regular waves, and compared with experiments conducted by *Yasukawa and Nakayama* (2009). The propeller thrust, the hull resistance, rudder forces, and viscous linear and nonlinear forces in sway and yaw, are modeled according to *Son and Nomoto* (1981). The basic details are given in Section 2.9. The main particulars of the hull, rudder and propeller are given in Table 5.1.

As mentioned in Section 2.9, the models in *Son and Nomoto* (1981) for the S-175, make use of semi-empirical parameters and coefficients to account for hull wake, rectification of the flow from the propeller to the rudder, and to model the rudder lift forces. In the present computations, no attempt has been made to tune these parameters to obtain a better fit with experiments.

5.1 Calm Water Turning Circle Test

At $t = 0$, the propeller is turned on and the ship is allowed to come up to the approach speed set at 6.212 m/s ($F_n = 0.15$). The propeller rps (revolutions/sec) to achieve this speed is calculated from the thrust-resistance balance and set at 0.9893 rps. In order to keep the ship on course, an automatic 4-DOF based nonlinear controller developed by *Li et al.* (2010) is used. At $t = 1200$ s, the rudder is put over at

LBP $[m]$	175.0
B $[m]$	25.4
T $[m]$	9.5
S $[m^2]$	5540
$\mathbf{C_W}$	0.7080
$\mathbf{C_B}$	0.5714
Rudder area $[m^2]$	33.04
Aspect ratio	1.8219
Propeller diameter $[m]$	6.533

Table 5.1: DETAILS OF CONTAINERSHIP S-175

maximum deflection of $\delta = -35^o$ to execute a tight starboard turn. The maximum rudder deflection rate is set to $\dot{\delta} = 5^o/s$. The track of the ship is shown in Figure 5.1. The results from the experimental data in *Yasukawa and Nakayama* (2009) is also shown for comparison. As can be seen from the plots, the agreement is quite good. The advance, transfer and steady turning diameter are in close agreement to the experimental values. The tactical diameter is off by about 0.8 shiplength. One possible explanation for this could be due to the additional lift forces and moments that are generated from the potential theory and the issue of "double-counting" mentioned in Section 2.9. Figures 5.1 (b) and (c) show the time-history of the translational and rotational velocities of the hydrodynamic frame as it is maneuvering.

5.2 Turning Circle Test in Regular Waves

The turning circle tests are performed for the containership S-175 in the presence of regular waves. Wave headings of $\theta = 90^o$ (Beam seas) and $\theta = 180^o$ (Head seas) are considered and λ/L is set to 0.7, 1.0, *and* 1.2. In order to compare with the available experimental results from *Yasukawa and Nakayama* (2009), the wave height is set equal to 3.5 m. This would correspond to $H/L = 1/50$, which implies the wave steepness changes with wavelength of the incident waves. As with the case of the calm water maneuvering test, the ship is brought up to an approach speed of 6.212

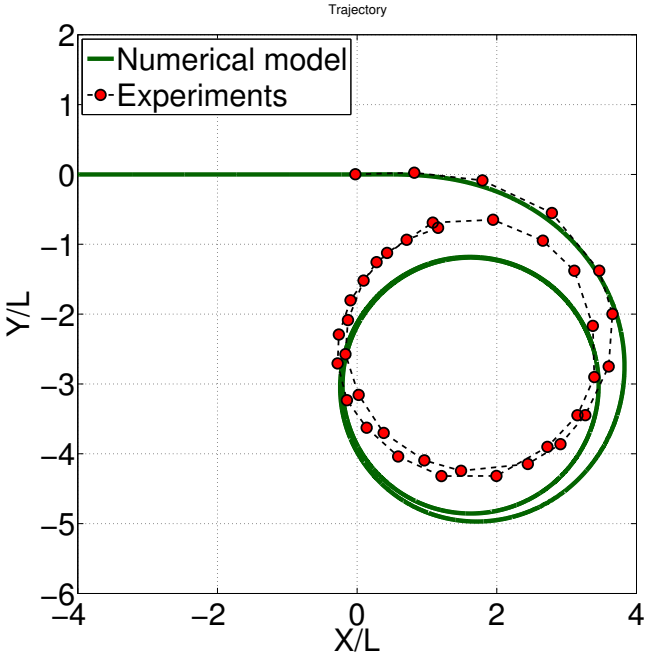

(a) Trajectory

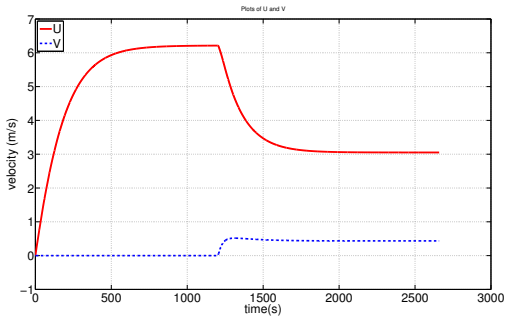

(b) Velocities U and V of hydrodynamic frame

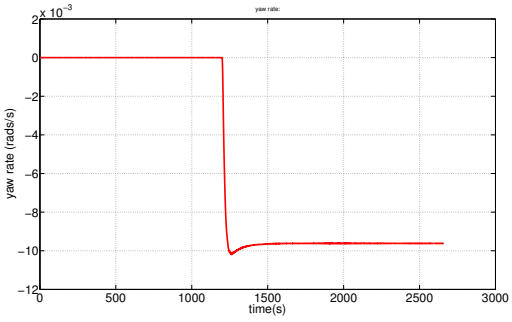

(c) Yawrate $\dot{\psi}$ of hydrodynamic frame

Figure 5.1: CALM WATER TURNING CIRCLE OF S-175, $\delta = -35^o$

m/s ($Fn = 0.15$) and once steady state is reached ($t = 1200$ s), the rudder is put hard over and simultaneously, the waves are turned on. A brief linear ramp of two periods is used to bring the waves to full wave height.

Figures 5.2 and 5.3 show the results of the starboard ($\delta = -35^o$) turning circle test for $\lambda/L = 1.0$ in beam seas. The arrow in Figure 5.2(a) indicates the direction of the waves and the shows the track of the ship. As can be seen, the model reasonably captures the general characteristics of the turn. The ship enters into a series of steady turning circle loops, along with a net drift due to the wave drift forces. It is interesting to note that there are drift components both along and perpendicular to the direction of the wave fronts. Although the steady turning diameter, advance, transfer and tactical diameter are being over-predicted, the overall course and drift of the ship is in the right direction. Figures 5.2(b) and 5.2(c) show interesting results for the translational and rotational velocities of the hydrodynamic frame, respectively. The model captures the increase and decrease of the velocities at different phases of the turn. As can be seen, the oscillatory component of the velocities is superimposed on the time-varying mean component. Figure 5.3 shows the details of roll, pitch and heave motions during the turning maneuver, of inset 1 in Figure 5.3(a). The interesting feature here is that as the ship traverses from a following sea configuration, through beam sea and into head sea, there is a shift in the frequency of encounter. This is evident from plots 5.3(b) and 5.3(c).

Figures 5.4-5.12 show the turning circle results for $\lambda/L = 1.0$, $\lambda/L = 1.2$, and $\lambda/L = 0.7$ for beam and head seas. For $\lambda/L = 1.0$ and $\lambda/L = 1.2$, the ship is able to enter into a series of loop to loop turns and drift in the right direction. The advance, transfer and turning diameter are being over-predicted by the present method. In general, it is observed that the rudder is encountering large opposing forces that are delaying the turning rate. This looks more apparent when the ship is in a following sea configuration. It also indicates that the forward speed is much higher than what

it should be, which results in a much larger turning diameter. The other issue is that of "double-counting", where the rudder is facing the opposing forces of viscous maneuvering forces $Y_j,\ N_j\ (j = v, r)$ as well as the forces being generated from the potential theory. The other source of over-prediction could be with the prediction of the 2^{nd} order wave drift forces and moments. It is known that as the wavelengths get shorter, the drift forces get larger. This is apparent from Figures 5.11 and 5.12, which represent the starboard and portside turning maneuver for $\lambda/L = 0.7$ in beam seas, respectively. The ship is being drifted by a large amount when it is in following sea condition. From Figure 5.11, it is seen that the ship in fact begins the turn pretty much in agreement with the experiments, before it turns around and enters the following sea configuration and begins being drifted a long way before the rudder can again turn the ship around. The turning tests for $\lambda/L = 0.7$ are done in relatively steep waves of $H/\lambda = 1/35$. In order to ensure that the incorrect drift is not a frequency related issue, the wave height was reduced, such that $H/\lambda = 1/50$, and the turn simulated. The result is shown in Figure 5.13, where the ship is drifting in the right direction. The other issue could also be that since the rudder model parameters are not tuned in any way, the lift forces produced by the rudder are not strong enough to tighten the turns.

The effect of changing the initial phase angle of the incident waves is seen in Figure 5.14. An initial phase angle of 0^o corresponds to a wave crest at midships at $t = 0$, and initial phase angle of 90^o corresponds to a zero crossing at $t = 0$. The shift in phase does not have an effect on the 2^{nd} order wave drift forces, but as can be seen from the details in Figure 5.14(b), there is a phase shift in the first order response as expected.

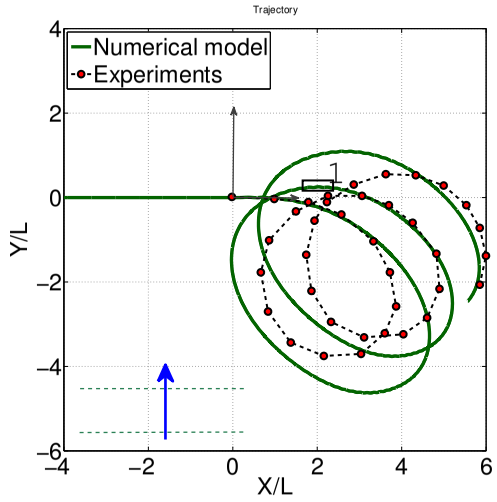

(a) Trajectory

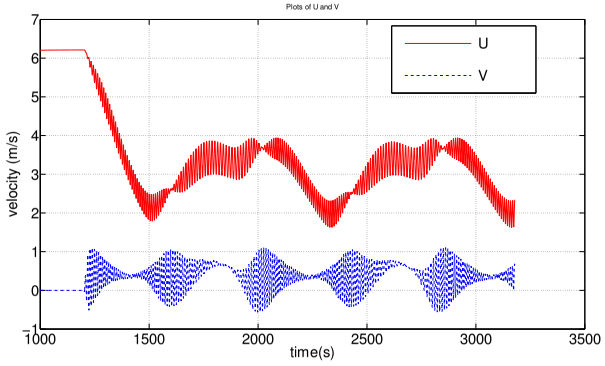

(b) Velocities U and V of hydrodynamic frame

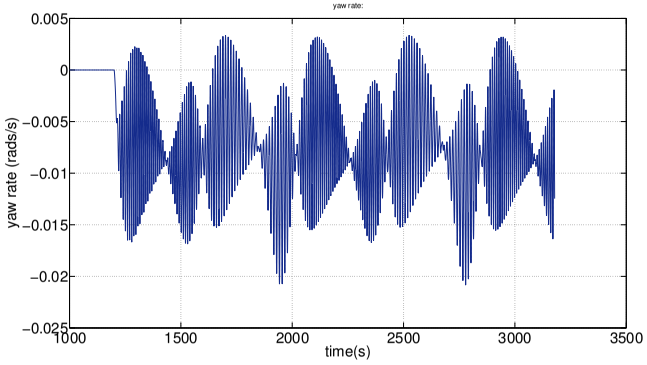

(c) Yawrate $\dot{\psi}$ of hydrodynamic frame

Figure 5.2: TURNING CIRCLE OF S-175 IN WAVES, $\delta = -35^o$, $\lambda/L = 1.0$, HEADING = BEAM SEAS, $H/\lambda = 1/50$

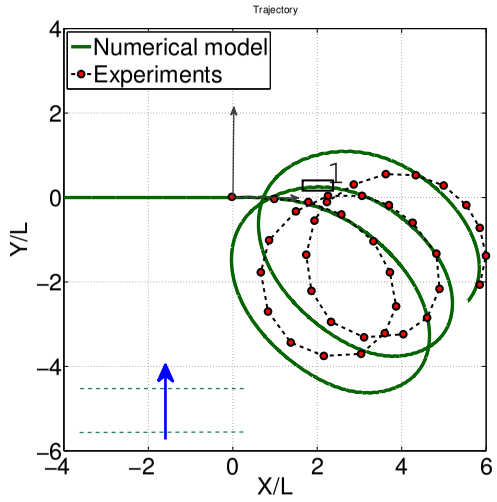

(a) Trajectory

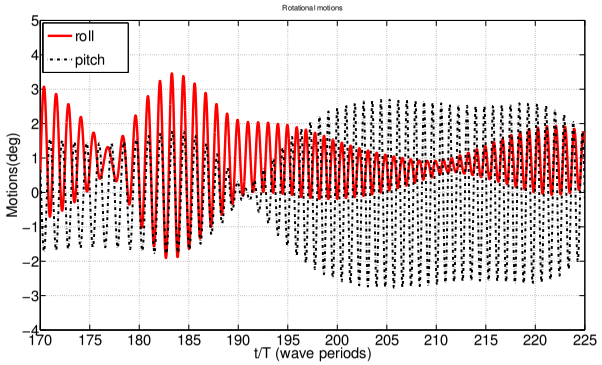

(b) Details of roll and pitch motions

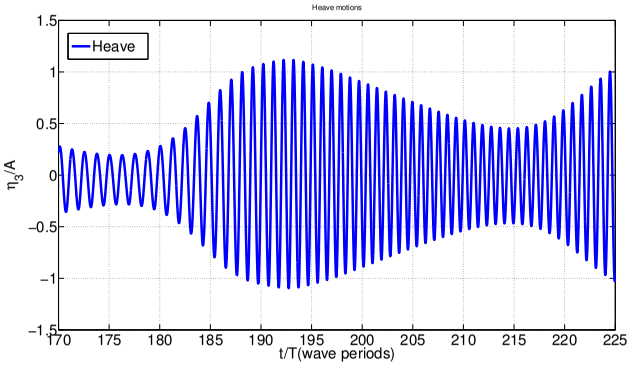

(c) Details of heave motions

Figure 5.3: DETAILS OF ROLL, PITCH AND HEAVE DURING TURNING MANEUVER, $\delta = -35^o$, $\lambda/L = 1.0$, HEADING = BEAM SEAS, $H/\lambda = 1/50$

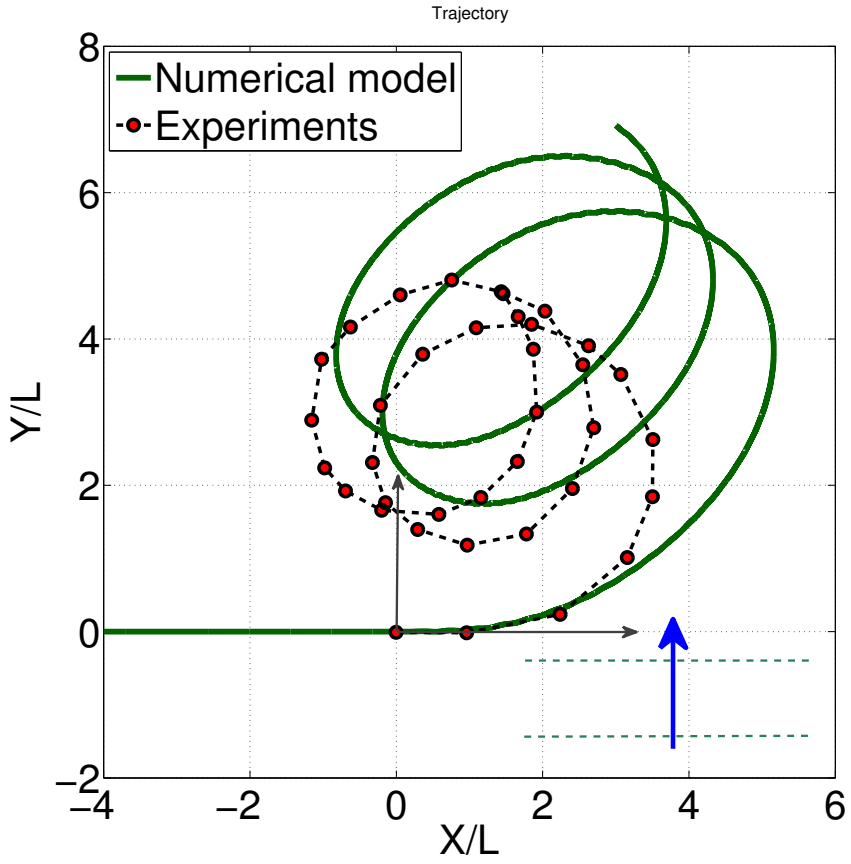

Figure 5.4: TURNING CIRCLE OF S-175 IN WAVES, $\delta = 35^o$, $\lambda/L = 1.0$, HEADING = BEAM SEAS, $H/\lambda = 1/50$

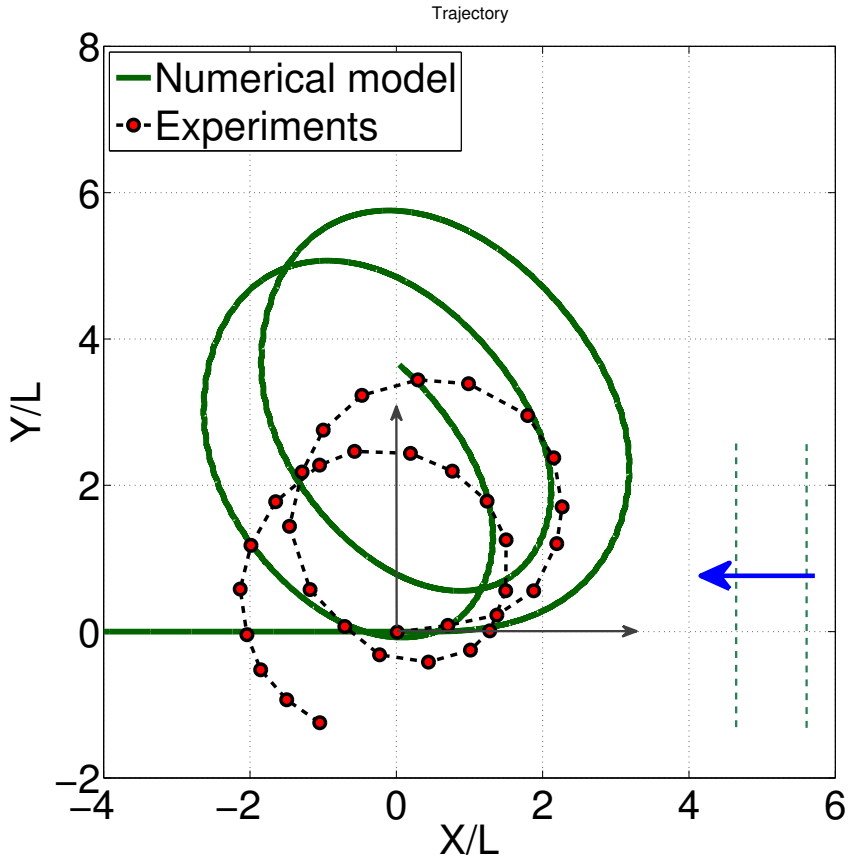

Figure 5.5: TURNING CIRCLE OF S-175 IN WAVES, $\delta = 35^o$, $\lambda/L = 1.0$, HEADING = HEAD SEAS, $H/\lambda = 1/50$

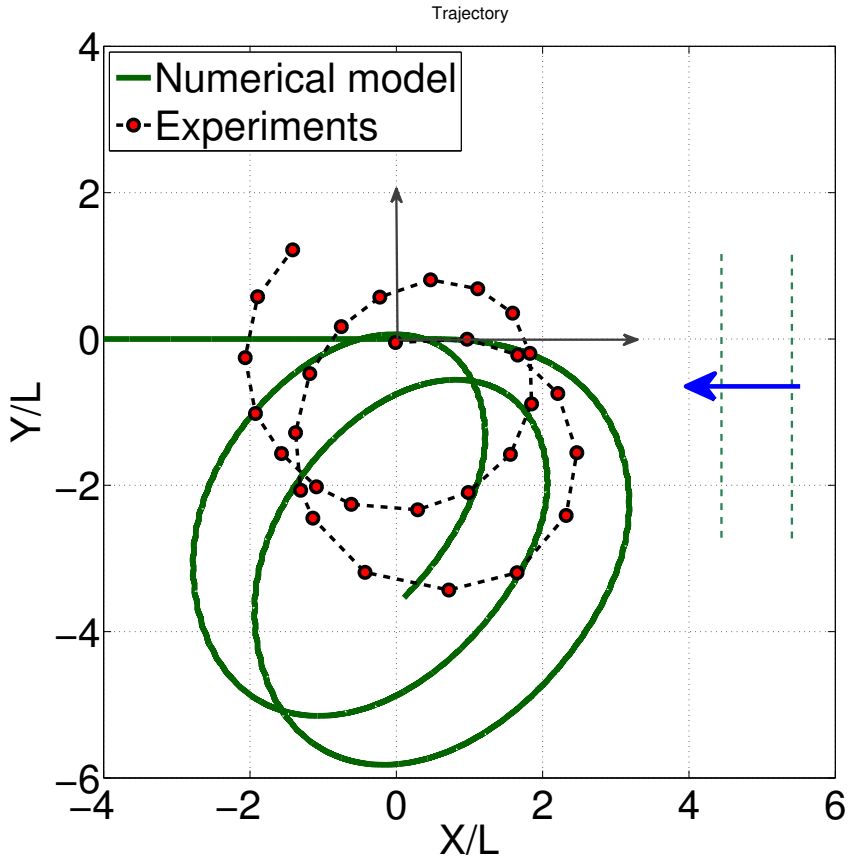

Figure 5.6: TURNING CIRCLE OF S-175 IN WAVES, $\delta = -35^o$, $\lambda/L = 1.0$, HEADING = HEAD SEAS, $H/\lambda = 1/50$

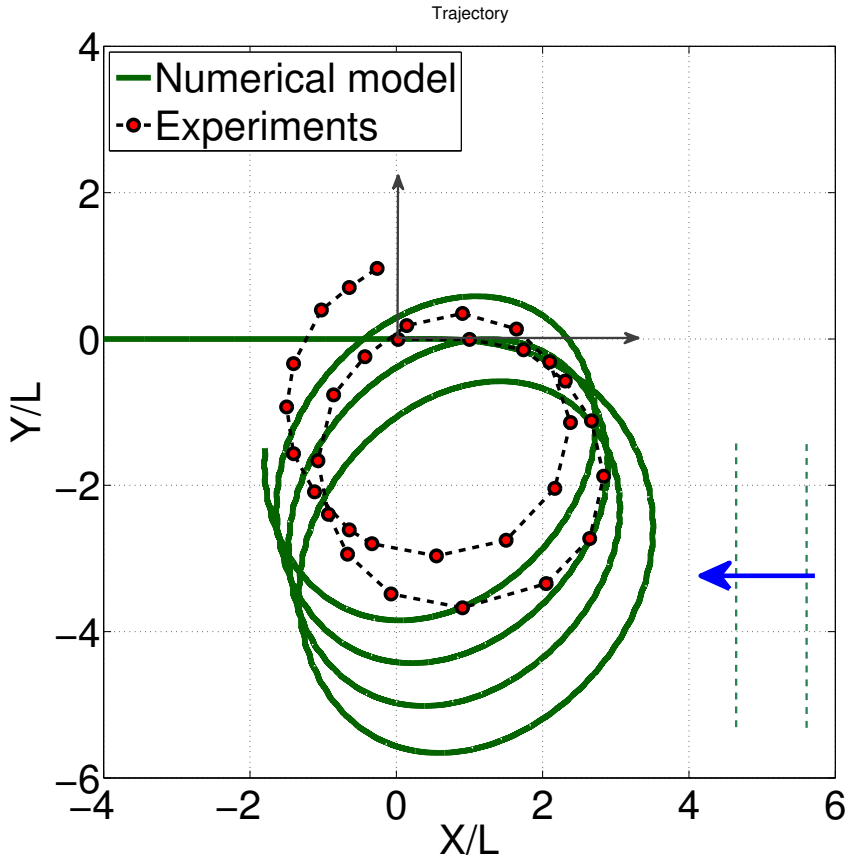

Figure 5.7: TURNING CIRCLE OF S-175 IN WAVES, $\delta = -35^o$, $\lambda/L = 1.2$, HEADING = HEAD SEAS, $H/\lambda = 1/60$

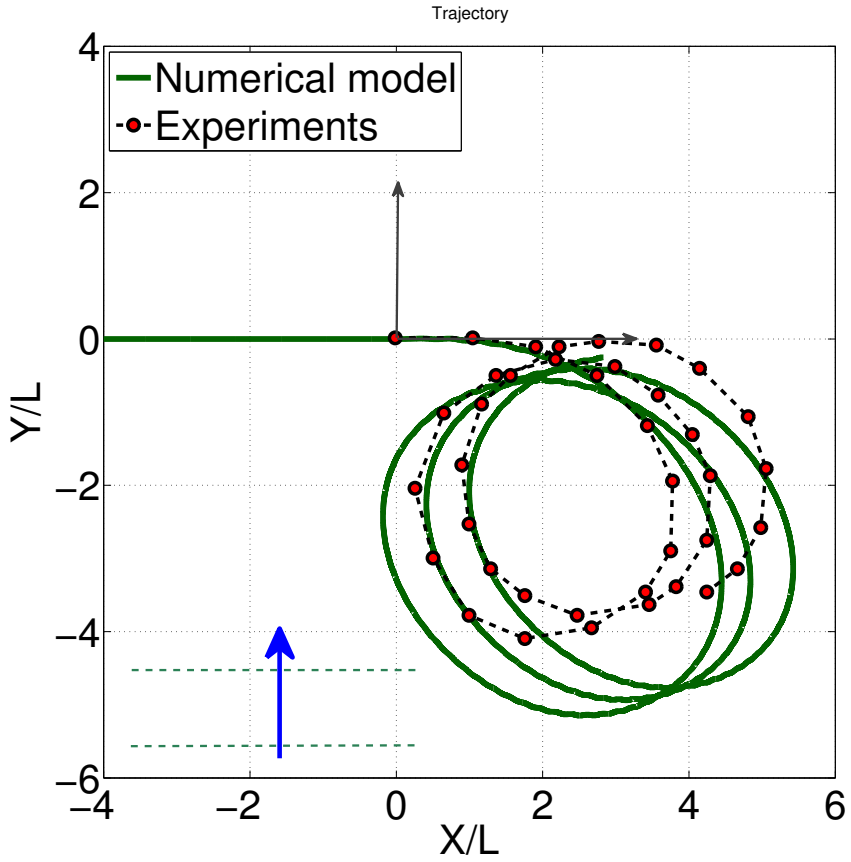

Figure 5.8: TURNING CIRCLE OF S-175 IN WAVES, $\delta = -35^o$, $\lambda/L = 1.2$, HEADING = BEAM SEAS, $H/\lambda = 1/60$

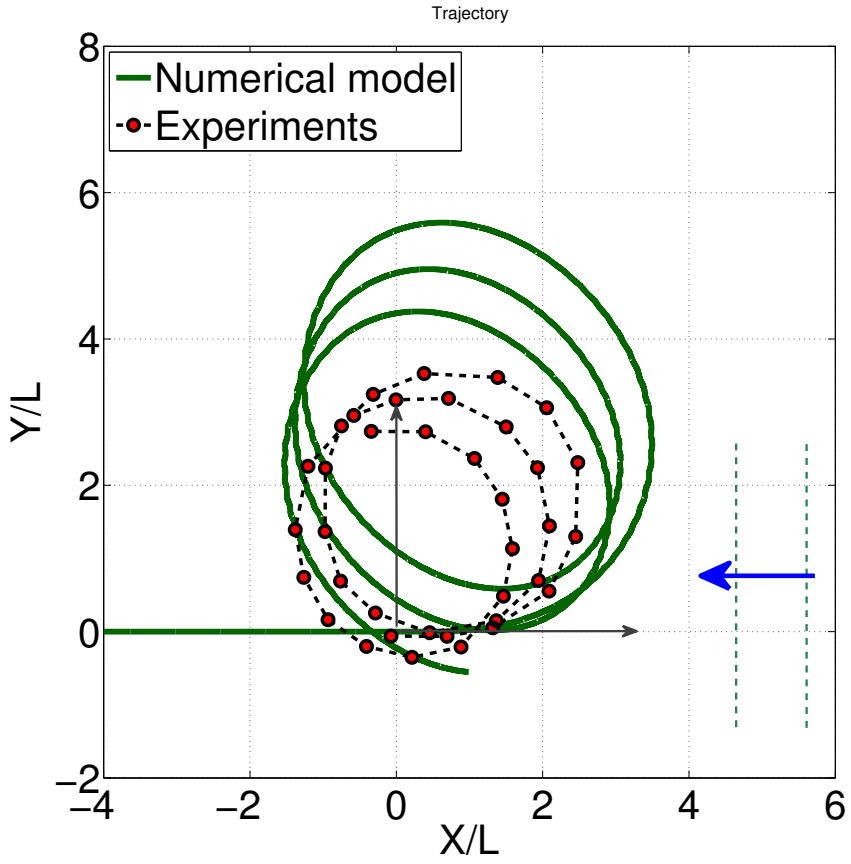

Figure 5.9: TURNING CIRCLE OF S-175 IN WAVES, $\delta = 35^o$, $\lambda/L = 1.2$, HEADING = HEAD SEAS, $H/\lambda = 1/60$

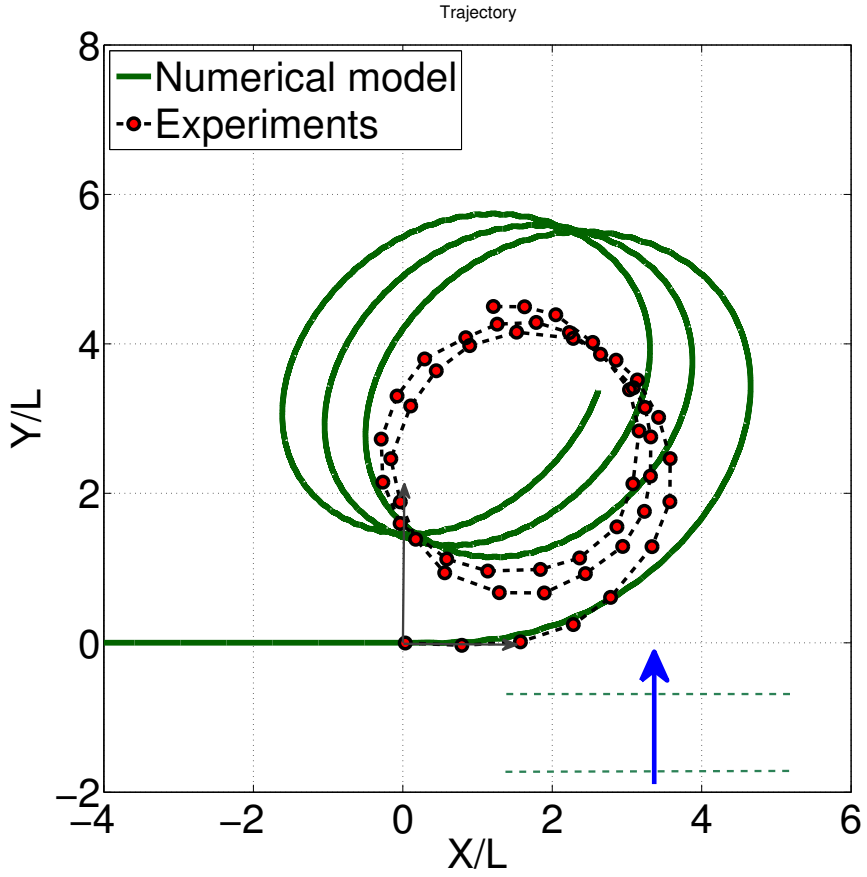

Figure 5.10: TURNING CIRCLE OF S-175 IN WAVES, $\delta = 35^o$, $\lambda/L = 1.2$, HEADING = BEAM SEAS, $H/\lambda = 1/60$

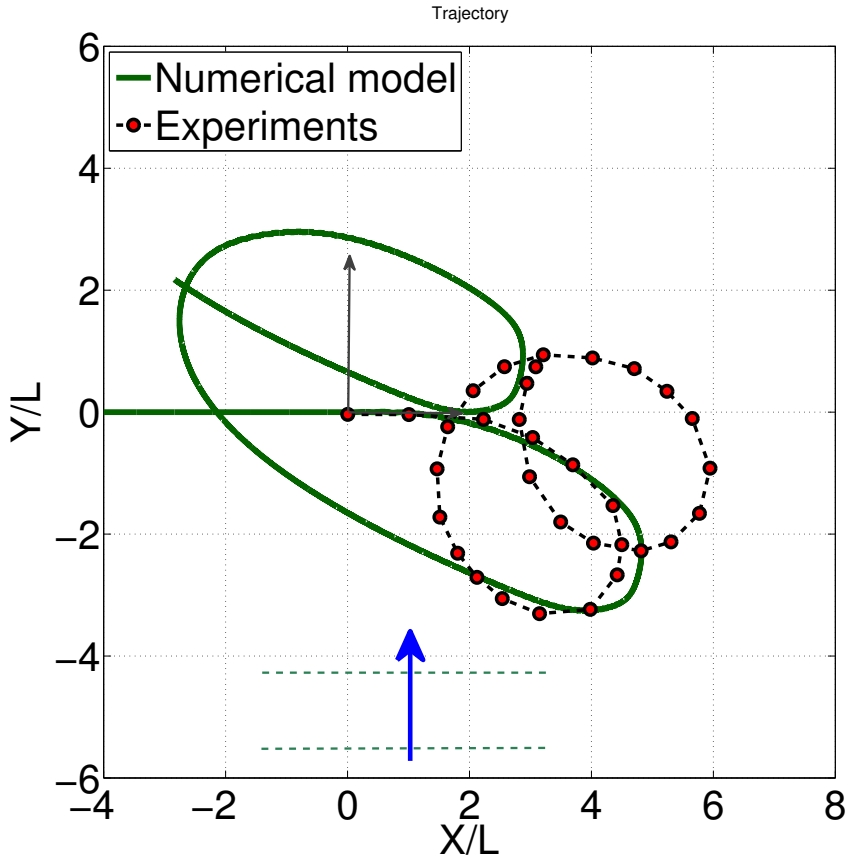

Figure 5.11: TURNING CIRCLE OF S-175 IN WAVES, $\delta = -35^o$, $\lambda/L = 0.7$, HEADING = BEAM SEAS, $H/\lambda = 1/35$

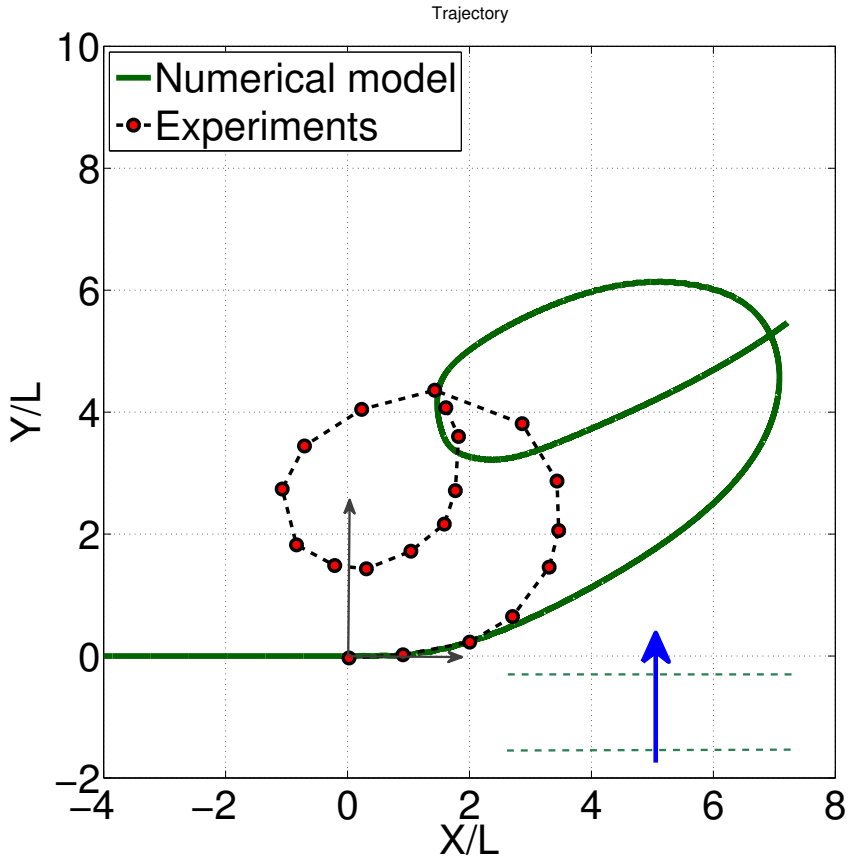

Figure 5.12: TURNING CIRCLE OF S-175 IN WAVES, $\delta = 35^o$, $\lambda/L = 0.7$, HEADING = BEAM SEAS, $H/\lambda = 1/35$

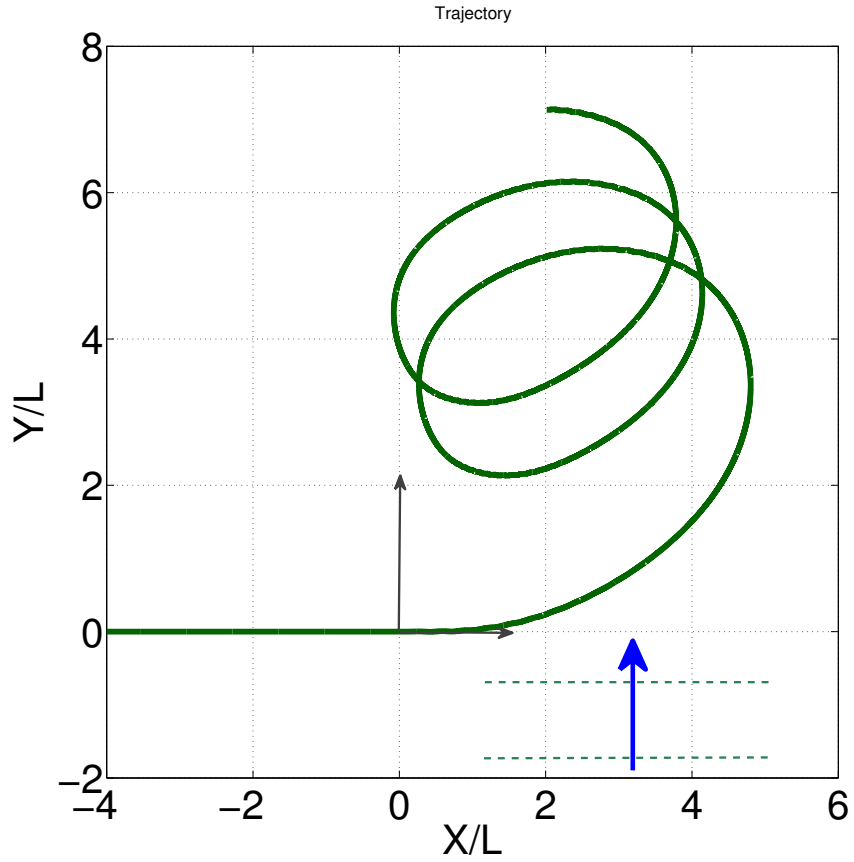

Figure 5.13: TURNING CIRCLE OF S-175 IN WAVES, $\delta = 35^o$, $\lambda/L = 0.7$, HEADING = BEAM SEAS, $H/\lambda = 1/50$

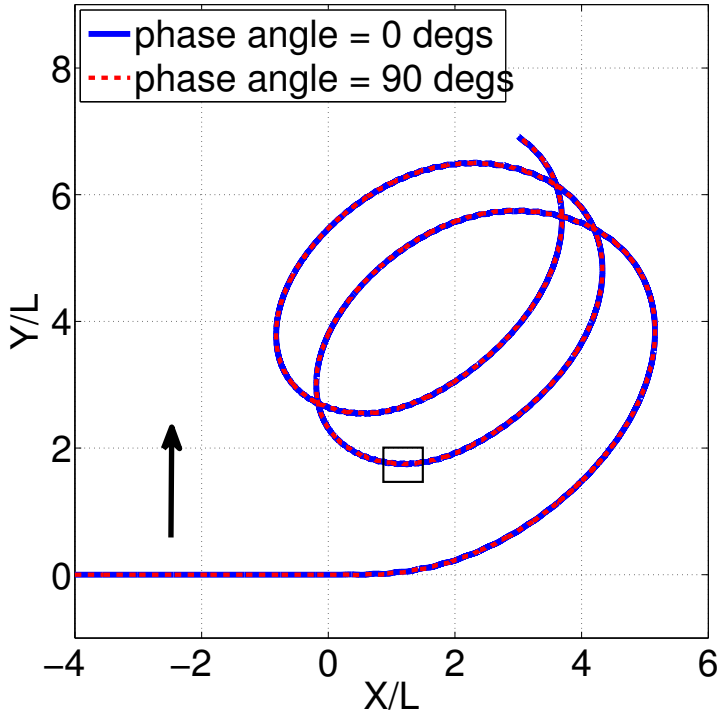

(a) Trajectory

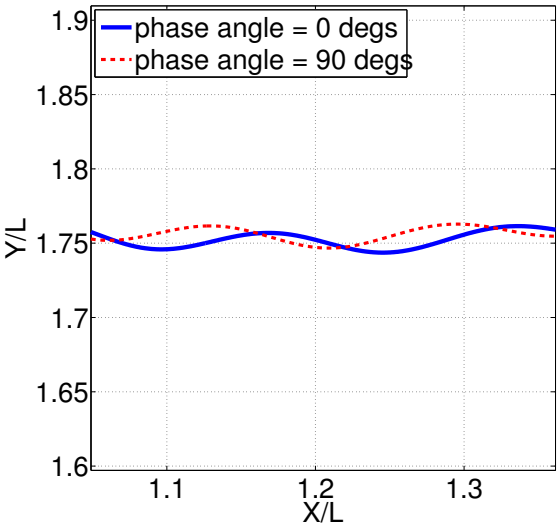

(b) Details of inset

Figure 5.14: EFFECT OF INITIAL PHASE ANGLE OF INCIDENT WAVES, $\delta = 35^o$, $\lambda/L = 1.0$, HEADING = BEAM SEAS, $H/\lambda = 1/50$

CHAPTER VI

Surge Damping Model

Although potential theory has proven to be a robust and powerful seakeeping prediction tool, it cannot predict viscous forces. For the horizontal plane motions, this is crucial due to lack of restoring forces. The viscous force models have been elaborated in this research work in Chapters II, IV and V. In this chapter, the surge force prediction capability of the strip theory approach is examined.

The present formulation is used to predict the surge force on the Wigley-I hull that is set into forced surge oscillations, towed at a constant forward speed. A simple empirical damping model is proposed and the force is added to the results from potential theory. The results from the simulations are compared with the results predicted by an Unsteady Reynolds-Averaged Navier-Stokes (URANS) equation CFD solver-openFOAM.

6.1 Empirical Scheme

A simple "quasi-steady" formulation in which the surge force is proportional to the instantaneous forward speed, is proposed to model the surge damping, F_{surge} given by:

$$F_{surge} = -\frac{1}{2} c_D \rho S u(t)|u(t)| \tag{6.1}$$

LBP $[m]$	4.0
B $[m]$	0.4
T $[m]$	0.25
S $[m^2]$	2.3796
$\mathbf{C_W}$	0.6886
$\mathbf{C_B}$	0.5571

Table 6.1: DETAILS OF WIGLEY-I HULL

where ρ and S are the density of fluid, and the wetted surface area, respectively. c_D is the drag coefficient based on the calm water resistance of the ship. The forward speed $u(t)$ is the instantaneous surge velocity. Therefore, this model predicts both the calm water resistance as well as the surge oscillatory damping.

6.2 URANS Formulation

The viscous flow solver is based on the open source CFD library OpenFOAM. It basically solves the URANS equations and uses a VOF method for interface capturing. The package is heavily customizable with a wide variety of options to specify the type of computational elements, solution gradients, discretization schemes for the convection and advection terms, interface-capturing schemes, type of solver for the transport equations and governing equations etc. It can also be run in parallel to speed up the computations.

6.3 Results and Discussion

The Wigley-I hull is used for the computations. The details are given in Table 6.1. The test matrix for the study is given in Table 6.2. The nondimensional frequency $\omega* = \omega\sqrt{L/g}$ used in the study, spans the normal range of frequencies used in sea-keeping analysis. The amplitude of motion, A is set such that $(2A)/\lambda$, the wave slope of the radiated waves is 1/60. Interestingly, this also implies that the amplitude of the acceleration of the body, $A\omega^2$ is constant across the frequency range. The forward

Run id	**1**	**2**	**3**	**4**	**5**
λ/L	0.5	1.0	1.5	2.0	2.5
A [m]	0.0167	0.0334	0.0500	0.0667	0.0834
T [s]	1.1323	1.6013	1.9612	2.2646	2.5318
ω (rads/s)	5.5490	3.9238	3.2037	2.7745	2.4817
$\omega*$	3.54	2.51	2.05	1.77	1.58
$\frac{A\omega}{U}$	0.049	0.071	0.085	0.099	0.110

Table 6.2: TEST MATRIX FOR FORCED SURGE PROBLEM

speed, U of the hull is set to 1.88 m/s, corresponding to a Froude number of 0.3.

Potential Flow Details

The present method uses 40 panels on the body, per station. The number of nodes/wavelength on the free surface is set to 30 and the computational domain length is set to 4 wavelengths on each side, including 2 wavelengths for the numerical beach. A time step size of $T/200$ is used for the numerical integration on the free surface.

OpenFOAM CFD Solver

The computational domain shown in Figure 6.1 extends from one ship-length upstream to $3L$ downstream. The lateral domain extends to one ship-length form the centreline and the bottom is set at $0.75L$ below the calm water level. The domain for the air column extends to $0.1875L$. The number of cells used in the computations is $163,580$. This is considered a coarse grid.

Calm Water Resistance

The calm water resistance of the Wigley hull at $F_n = 0.3$ is computed by using the OpenFOAM solver. Figure 6.2 shows the wave patterns generated by the ship. The computations were run out to 100 s to allow for the transients to decay. The dynamic pressure on the hull surface with the high pressure bow region, is shown in

Figure 6.3. The calm water resistance is computed by integrating the pressure and shear stress on the hull surface. The calm water resistance time history is shown in Figure 6.4 with both the pressure and viscous components. The value of F_{calm}, the calm water resistance, is calculated to be 18.9860 N by averaging over the last few cycles. The value from the experiments is about 20 N, which is a difference of 5%. This is used to compute the value of c_D to be used in the empirical model, which turns out to be 4.4047×10^{-3}.

Forced surge motions

The forced surge motions are performed by using the test matrix in Table 6.2 as input to both the body-exact potential flow solver, and the OpenFOAM URANS solver. The simulations are run for 50 periods. The surge force from the damping model is added to the potential theory results.

Figures 6.5 - 6.9, show the surge force time history for the 5 test cases from $\lambda/L = 0.5$ to $\lambda/L = 2.5$. Comparisons are made between the forces predicted with and without the damping model, to the CFD results. It is observed that the potential theory formulation, underpredicts the force compared to CFD, while the surge force model overpredicts it. As expected, the potential theory gives better results at higher frequencies, and gets worse as frequency drops, eventually predicting zero damping at $\omega = 0$. On the other hand, potential theory predicts the forces within a good level of accuracy for the higher frequencies, in particular, for $\lambda/L \leq 1.0$. The results suggest that although the damping model does help in correcting the values from potential theory, it is overpredicting the values, and thus may need to be carefully augmented based on the frequency. One solution would be in the manner that *Bailey et al.* (1997) used a linear ramp to correct the potential theory sway and yaw forces by adding the maneuvering derivatives as viscous effect corrections. Figures 6.11 and 6.12 are the frequency domain results obtained by running the time domain results through a

FFT routine. It gives a better perspective of the model used and can be used to improve the empirical method to correct the potential flow results. The combined wave systems of the steady forward speed problem and forced surge oscillations are shown in Figure 6.10.

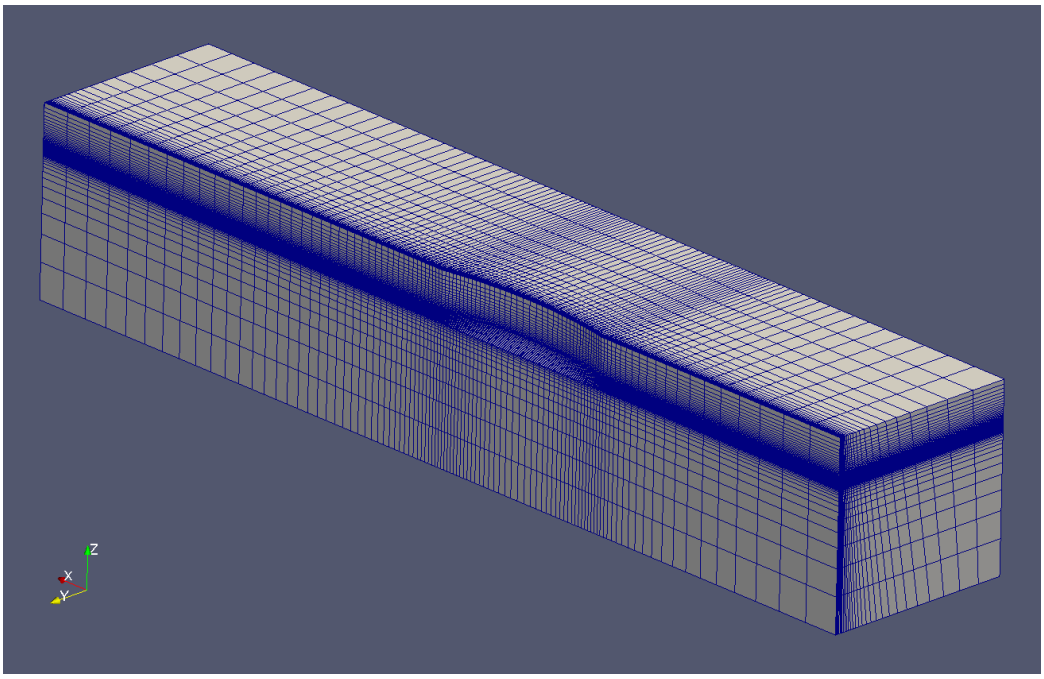

Figure 6.1: OpenFOAM COMPUTATIONAL DOMAIN

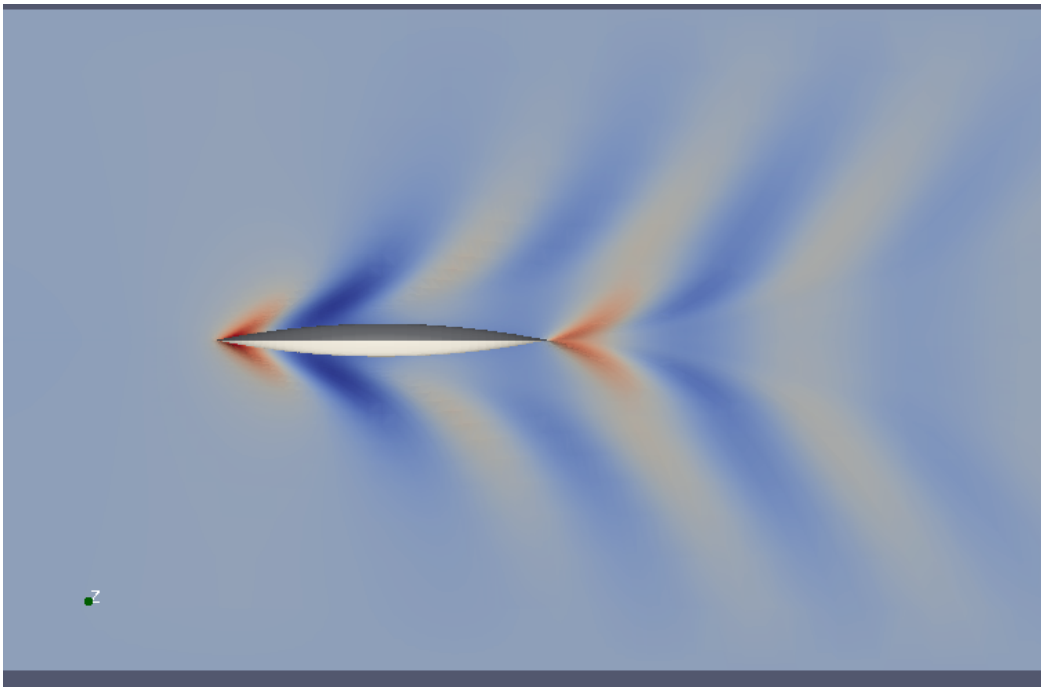

Figure 6.2: CALM WATER WAVE PATTERN, $F_n = 0.30$ (OpenFOAM)

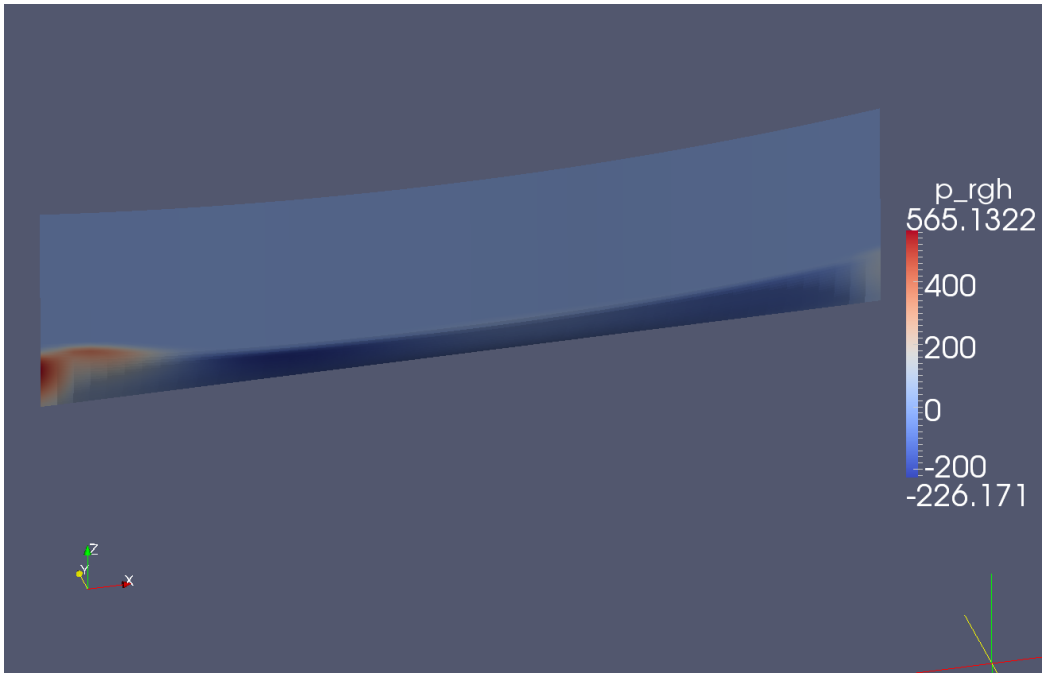

Figure 6.3: DYNAMIC PRESSURE ON HULL SURFACE, $F_n = 0.30$ (OpenFOAM)

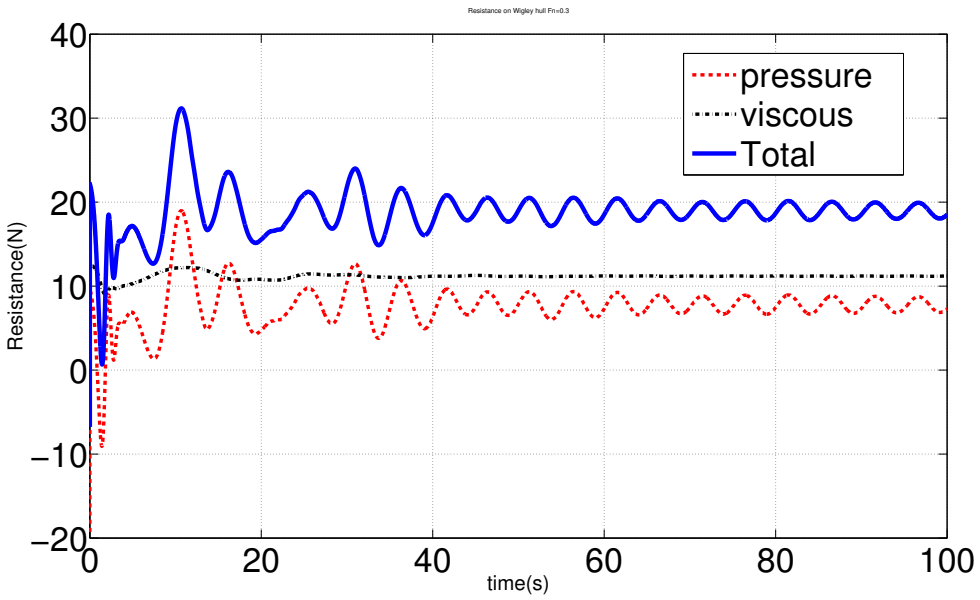

Figure 6.4: CALM WATER RESISTANCE, $F_n = 0.30$ (OpenFOAM)

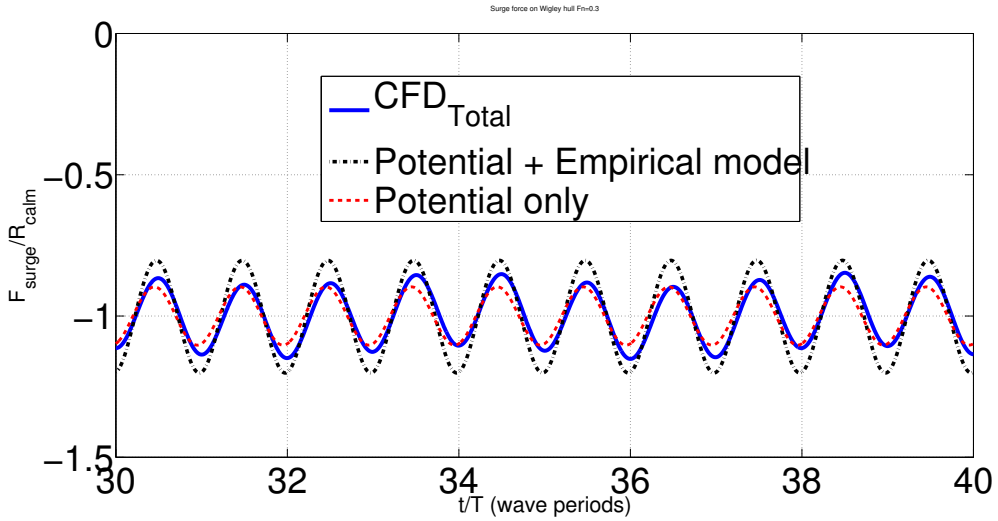

Figure 6.5: SURGE FORCE $\lambda/L = 0.5$

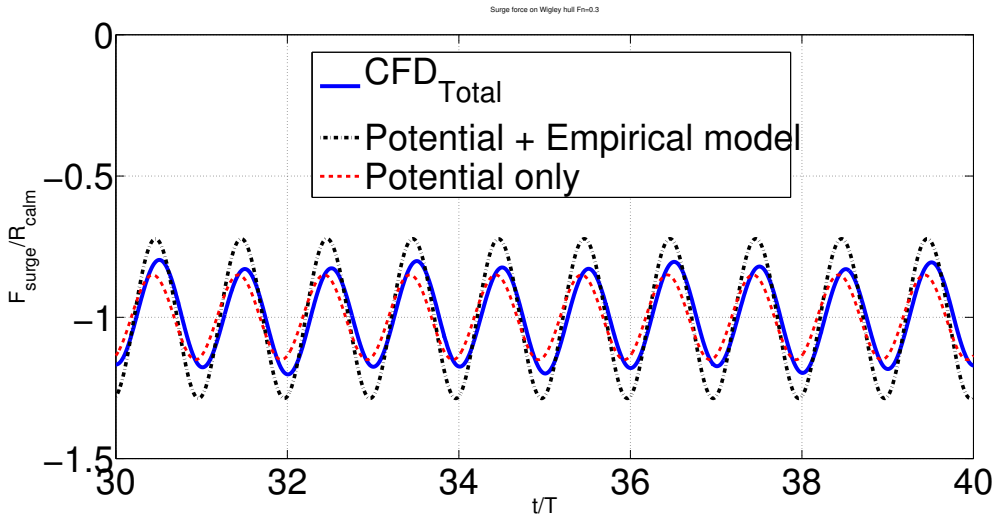

Figure 6.6: SURGE FORCE $\lambda/L = 1.0$

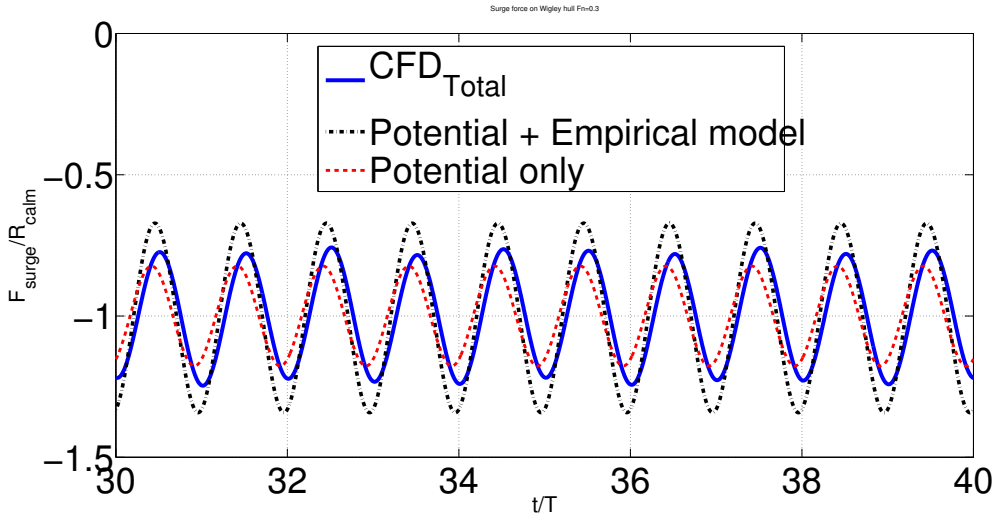

Figure 6.7: SURGE FORCE $\lambda/L = 1.5$

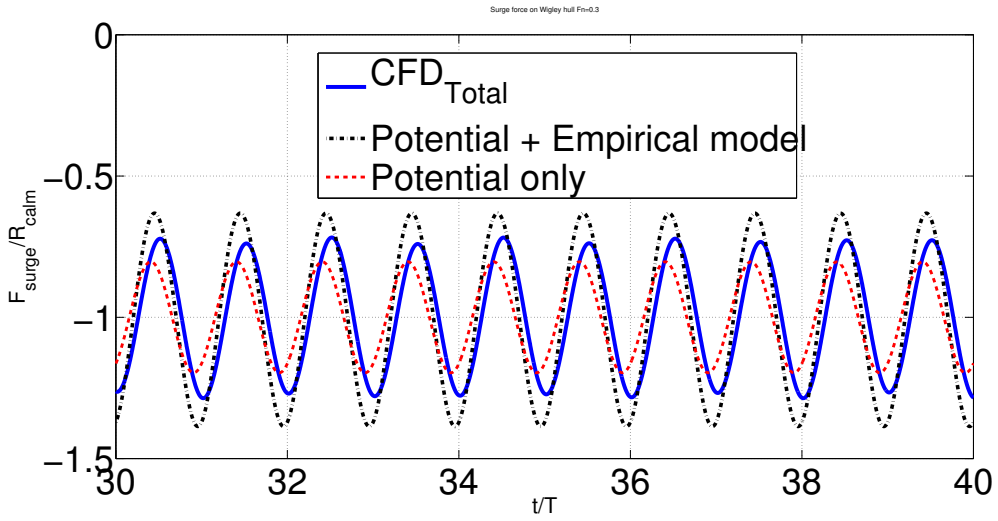

Figure 6.8: SURGE FORCE $\lambda/L = 2.0$

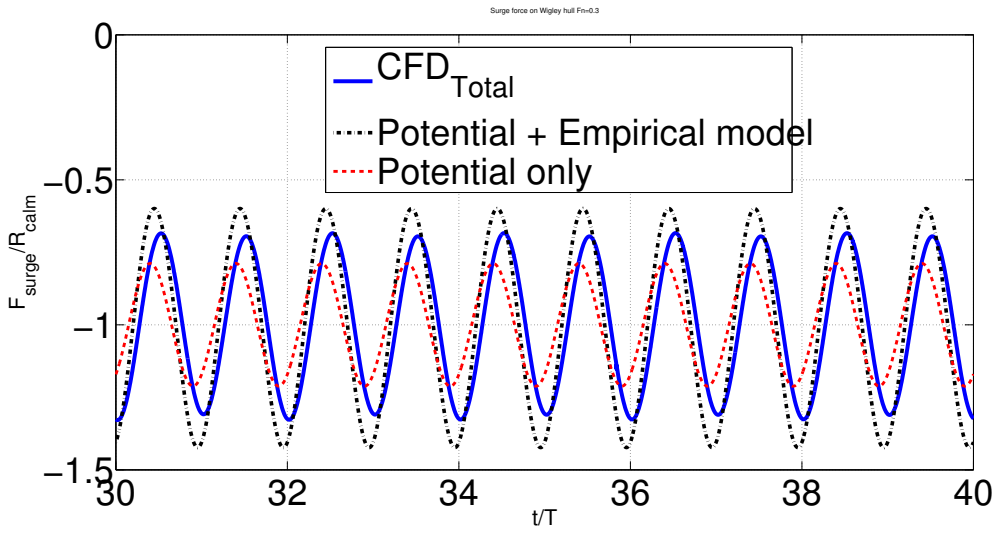

Figure 6.9: SURGE FORCE $\lambda/L = 2.5$

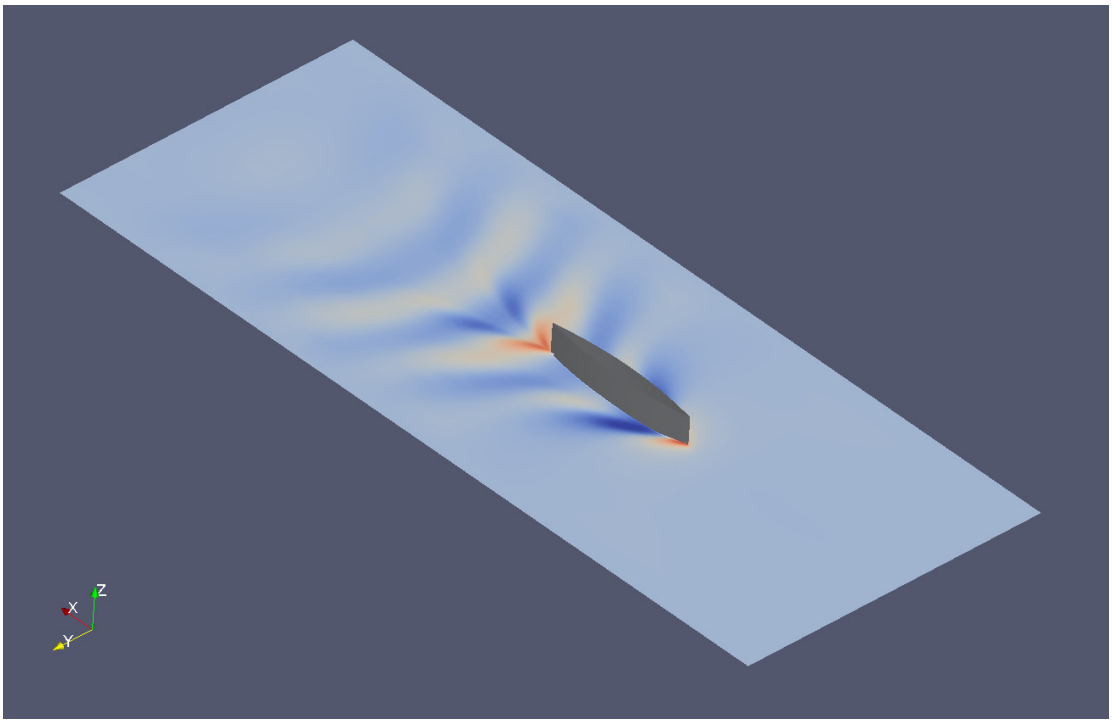

Figure 6.10: FREE SURFACE, FORCED SURGE $\lambda/L = 2.5$

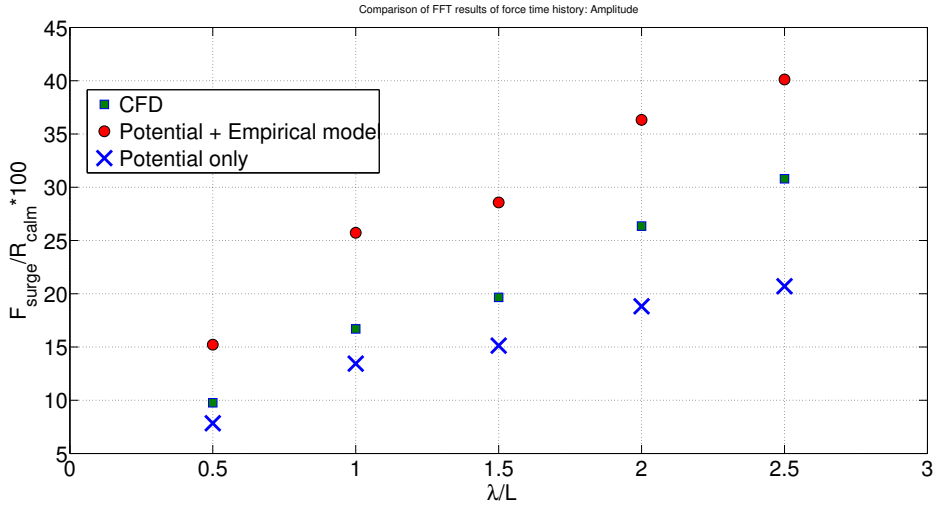

Figure 6.11: COMPARISON OF FORCE AMPLITUDES FROM FFT ANALYSIS

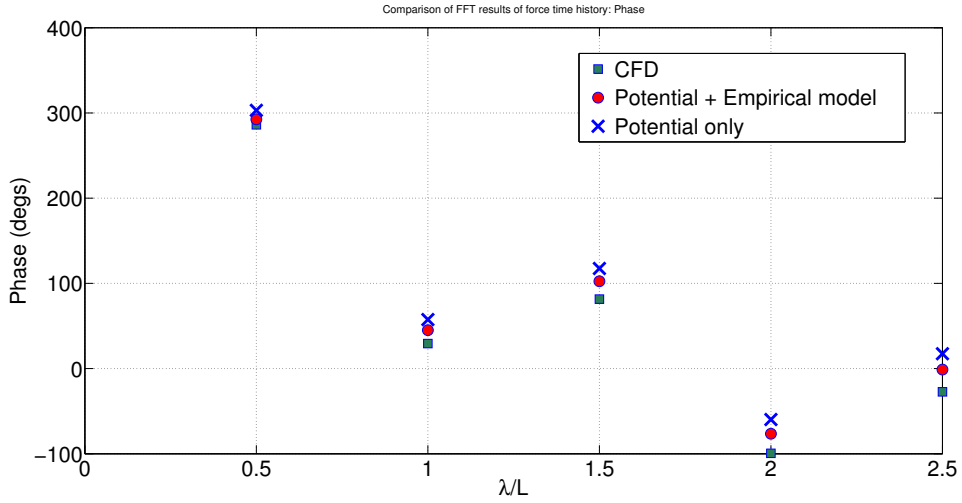

Figure 6.12: COMPARISON OF FORCE PHASE FROM FFT ANALYSIS

CHAPTER VII

Conclusions and Recommendations

A body-exact strip theory has been developed to simulate maneuvering of a ship in a seaway. Free motion drift simulations have been performed on the Wigley-I and containership S-175. The long time simulations establish the ability of the translating and rotating hydrodynamic axis system in predicting the drift and steady state stable equilibrium configuration of the ship wrt the waves. Both first order responses at the wave frequency, and higher order slowly varying drift motions are captured. The results also establish the stability of the numerical scheme and the numerical damping beach by the ability to simulate hundreds of wave periods. The methodology is robust enough to handle realistic hull forms like the S-175 with a bulbous bow and transom stern.

Propeller thrust force, calm water resistance, viscous forces and rudder lift forces are modeled based on semi-empirical methods, to predict the turning circle maneuver of the containership S-175 in calm waters and in the regular waves. The qualitative aspects of the maneuver are captured by the numerical model, in particular for longer waves.

In order to make quantitative comparisons, there are issues that need to be addressed. In the present methodology, the potential theory predicts lift forces and moments. The steady potential corresponding to the time-varying mean component of

the body velocity is also solved for in the present formulation. In a three-dimensional linear potential method, there would be no lift forces generated on a body. The forces predicted by the present method could be an artifact of strip theory, so one solution would be to avoid solving the steady velocity potential and only solve for the oscillatory component. Another approach would be to reduce the viscous forces to avoid "double-counting" the hull lift forces.

Improved models for predicting the rudder forces and propeller rudder interactions are needed. The models that are used in the present computations are directly from the ones used in *Son and Nomoto* (1981). No attempt has been made to tune these coefficients to improve the prediction. Since the model is known to be sensitive to these parameters, it is crucial to correctly account for these factors. It is also to be noted that, the present simulations do not consider the side force from the propeller, which can be quite a significant percentage of the forward thrust.

Radial basis functions are used to compute the x-derivative. Although their reliability has shown to be sufficient, there is scope for improvement by use of improved basis functions. They are also one of the most time-consuming routines in the computer code, so improvements in the efficiency of these routines could also translate to much faster computational times.

A simple empirical surge damping model has been proposed and used to correct the surge force predictions made by the potential theory. Comparisons are made with results obtained from CFD. Although, the model does correct the potential flow results, they are being overpredicted. The analysis does provide a basis to improve the damping model by considering a correction factor, such as the linear ramp that is used in *Bailey et al.* (1997).

APPENDICES

APPENDIX A

Convergence Results

Any numerical scheme must be studied for convergence. This gives a handle on the maximum value of the resolution, that gives an acceptable solution. The studies are done for two scenarios. The first set of convergence studies is done for the forced heave problem of the Wigley-I hull form. The convergence study with respect to time-step size is also done for the free motion drift problem of the Wigley-I. This is important because, since the simulations are being done for long times, quantities like body accelerations and velocities are integrated in time, causing accumulation of the integration errors at each time-step.

A.1 Forced Heave Problem

The Wigley-I hull is set into forced heave motions, and the heave force is used to study convergence characteristics. The details of the hull are given in Table 4.1 in Chapter IV. The frequency of oscillations is chosen such that, the wavelength, λ to shiplength, L ratio is $\lambda/L = 1.25$. The amplitude of motions, A is set equal to about 15% of the draft, T.

Three parameters are studied in the problem, namely, the time-step size, number of body panels, and the free surface domain size. It is to be noted that, the free

surface resolution is not entirely independent of the body resolution. In order to maintain good condition number of the influence matrix, the free surface resolution has to be of the same order of magnitude as the body resolution. It is observed that for convergence of the solution, there is a minimum free surface resolution required for a given body resolution. Therefore, in these tests, the free surface resolution is changed proportionately to the body resolution. The time-step size is based on the period of the radiated waves. The free surface domain is based on the size of the inner region. The outer region, consisting of the damping beach, is set to two wavelengths and fixed.

The convergence is studied, by changing one parameter at a time, keeping the others fixed at a high resolution value deemed sufficient for converged results. The results are shown in figures A.1 - A.3. As can be see, the convergence w.r.t the time-step size is fast. Based on the results, 50 panels on the body, a free surface resolution of $\lambda/30$ and free surface domain length of 2 wavelengths is considered as a set of parameters to have a good balance between computational speed and accuracy.

A.2 Free Motion Drift

As an additional check, the convergence is also studied for the free motion drift problem of the Wigley-I in the presence of external waves. The convergence is studied with respect to the time-step size, to ensure that the solution is not affected by accumulation of integration errors. The results are shown for the track and yaw motion time history in figures A.4 and A.5, respectively.

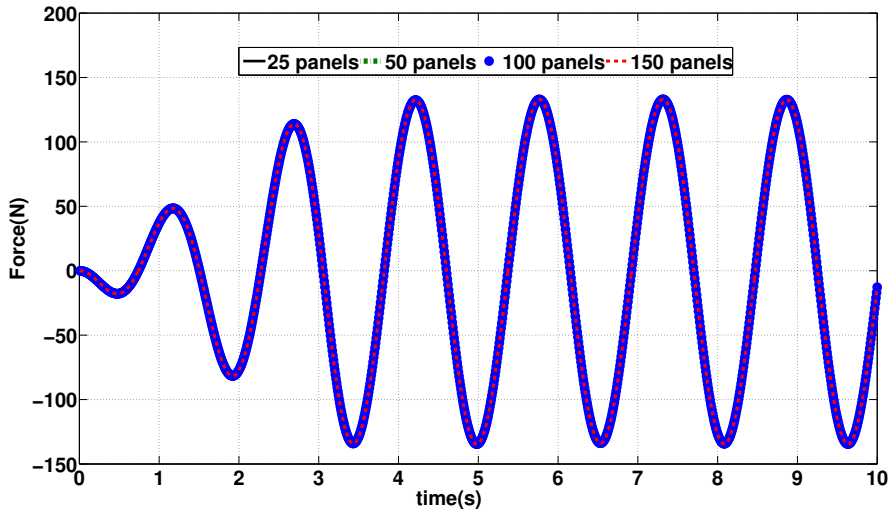

(a) Time history of heave force

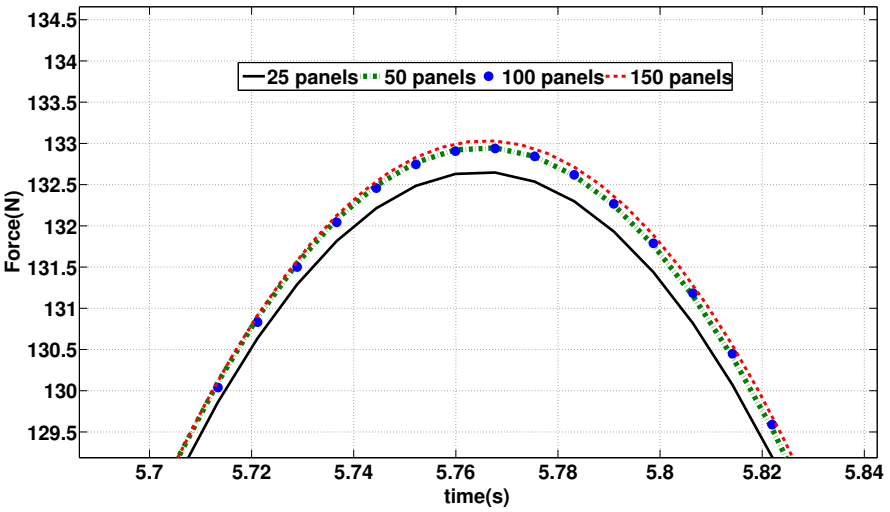

(b) Details

Figure A.1: CONVERGENCE STUDIES FOR NUMBER OF BODY PANELS, FREE SURFACE RESOLUTION FOR 25 BODY PANELS = $\lambda/30$, 50 BODY PANELS = $\lambda/60$, 100 BODY PANELS = $\lambda/60$, 150 BODY PANELS = $\lambda/90$. TIME-STEP SIZE = $T/200$. FREE SURFACE INNER DOMAIN = 2 WAVELENGTHS.

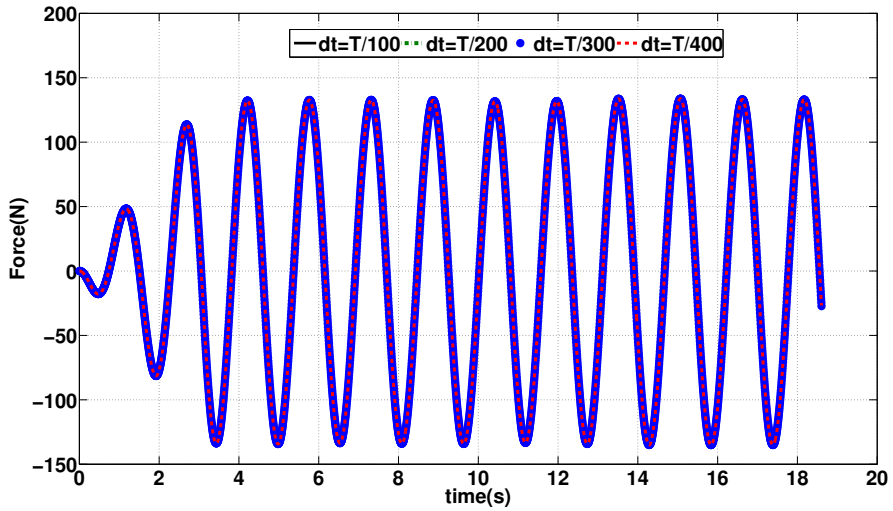

(a) Time history of heave force

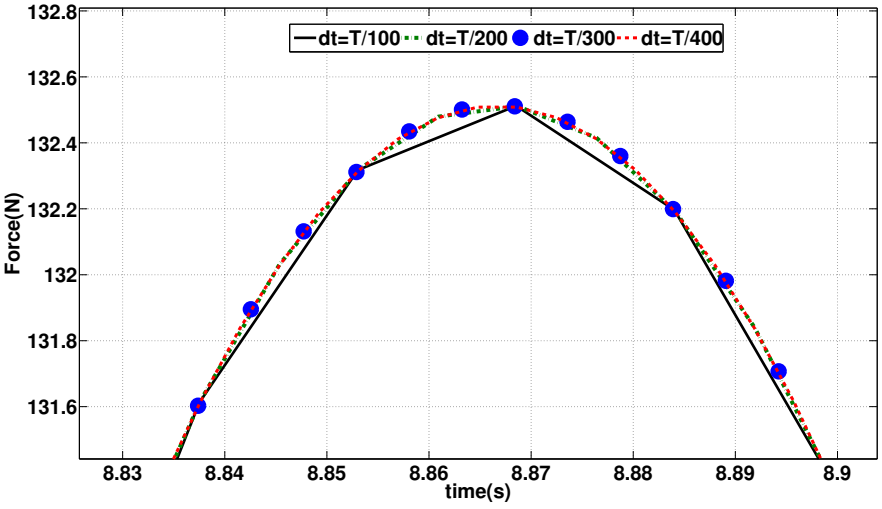

(b) Details

Figure A.2: CONVERGENCE STUDIES FOR TIME-STEP SIZE, NUMBER OF PANELS ON BODY = 50, FREE SURFACE RESOLUTION = $\lambda/30$. FREE SURFACE INNER DOMAIN = 2 WAVELENGTHS.

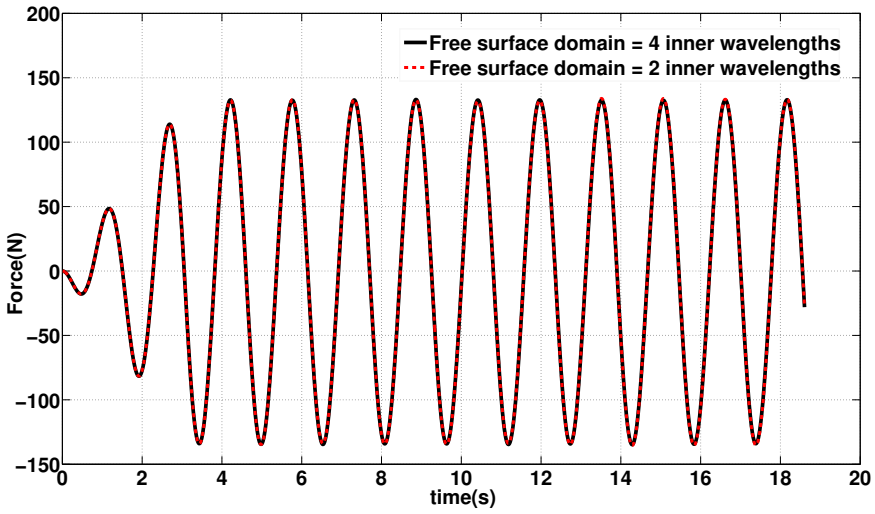

(a) Time history of heave force

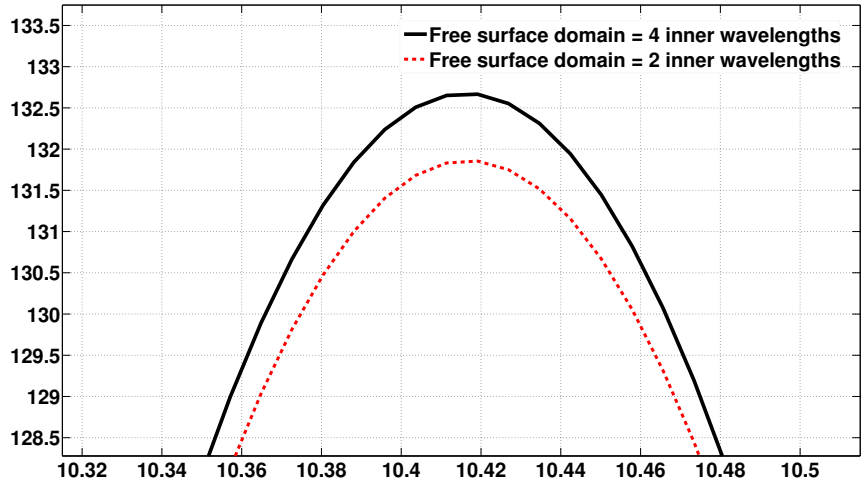

(b) Details

Figure A.3: CONVERGENCE STUDIES FOR INNER DOMAIN SIZE, NUMBER OF PANELS ON BODY = 50, TIME-STEP SIZE = $T/200$. FREE SURFACE RESOLUTION = $\lambda/60$.

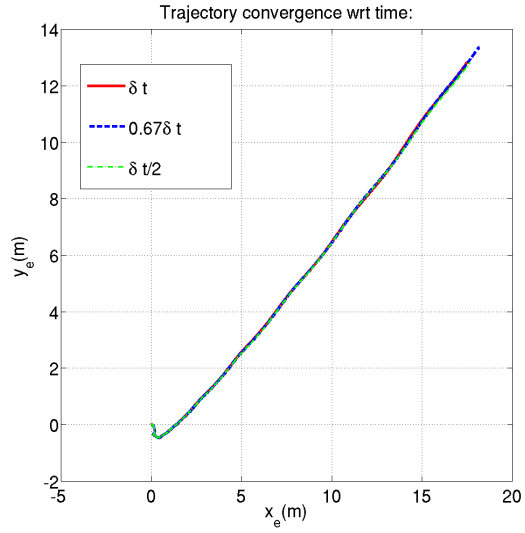

(a) Track of ship

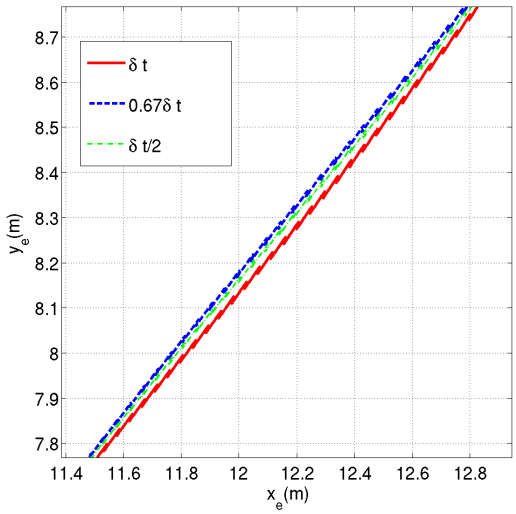

(b) Details of track of ship

Figure A.4: TRACK OF SHIP-CONVERGENCE STUDIES FOR TIME-STEP SIZE, FREE MOTION DRIFT OF WIGLEY-I, NUMBER OF PANELS ON BODY = 50, REFERENCE TIME-STEP SIZE $\delta t = T/200$. FREE SURFACE RESOLUTION = $\lambda/30$, FREE SURFACE INNER DOMAIN = 2 WAVELENGTHS.

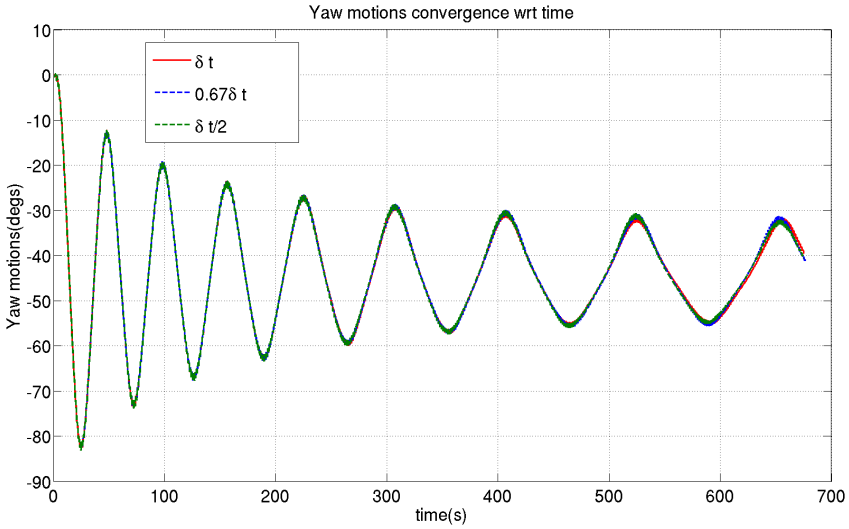

(a) Yaw motion time history

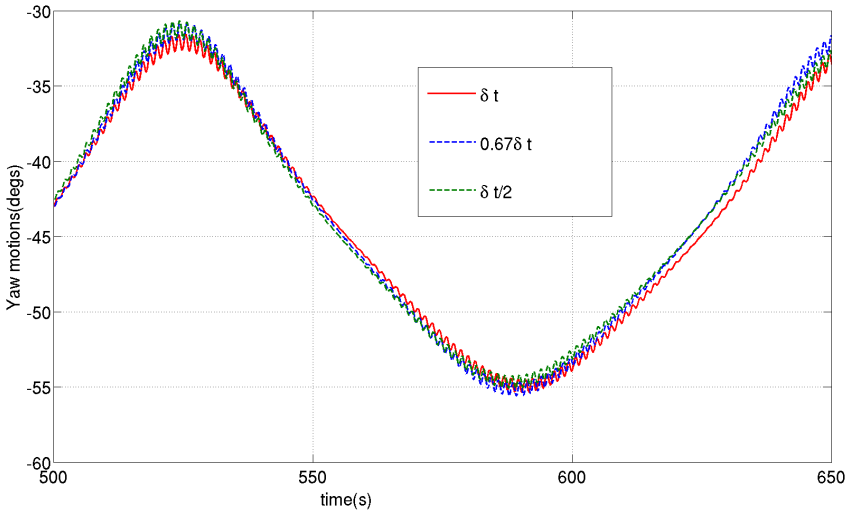

(b) Details of yaw motions

Figure A.5: YAW MOTIONS OF SHIP - CONVERGENCE STUDIES FOR TIME-STEP SIZE, FREE MOTION DRIFT OF WIGLEY-I, NUMBER OF PANELS ON BODY = 50, REFERENCE TIME-STEP SIZE $\delta t = T/200$. FREE SURFACE RESOLUTION = $\lambda/30$, FREE SURFACE INNER DOMAIN = 2 WAVELENGTHS.

APPENDIX B

Validation of Computer Code

Computer codes are prone to bugs and programming errors. It is therefore, important to validate the code by performing suitable tests. Since the present methodology is designed to handle a variety of hull forms, where the length scales of the problem could range from model scale to full scale, the code is tested for invariance with respect to scale. Also, since the physics of the problem is independent of the coordinate reference frame used, the code is tested for invariance with respect to the coordinate frame.

B.1 Scale Factor Test

The Wigley-I hull is set into forced heave oscillations, and the heave force is used to verify the invariance of the problem with respect to the scale factor. Two sets of computations are performed, one at model scale and the other at a scale factor of 60. The forces are compared by nondimensionalising the heave force by $\frac{1}{2}\rho L^2(A\omega)^2$. The details of the parameters used for the test are given in Table B.1.

The results for the scale factor test is given in Figure B.1. The details in Figure B.1(b) highlight the differences in solution, when the input is scaled by a factor of

Scale factor	1	60
LBP$[m]$	3.0	180.0
B$[m]$	0.3	18.0
T$[m]$	0.1875	11.25
S$[m^2]$	1.3385	4818.6
$\mathbf{C_W}$	0.6886	0.6886
$\mathbf{C_B}$	0.5571	0.5571
$\boldsymbol{\omega}[rads/s]$	4.0525	0.5232
A$[m]$	0.0250	1.5

Table B.1: WIGLEY-I PARTICULARS FOR SCALE FACTOR TEST

60. The difference is in the 3^{rd} decimal place, a variation of 0.16% compared to scale = 1. The difference could be attributed to the fact that the input data is rounded off to the 4^{th} decimal place.

B.2 Coordinate Frame Invariance Test

The free motion drift simulation of the Wigley-I hull is used to verify the coordinate frame invariance. Two sets of simulations are done. In the first case, at $t = 0$, the ship is aligned with the x_e axis. The waves are incident at an angle of $\theta = 45^o$. This is called reference frame 1 for convenience. In the second case, the ship is set at an initial yaw angle of $\theta = -45^o$, and the waves are incident at $\theta = 0^o$. This is called reference frame 2. Both the problems are exactly the same, with the difference being only in the coordinate frame reference. The wavelength and wave height of the incident waves are such that, $\lambda/L = 1.0$, and $H/\lambda = 1/50$, respectively. Viscous forces in sway and yaw are included in the computations.

The results are shown in Figures B.2 - B.4. Figure B.2 shows the comparison of the track of the ship, between the two frames. The comparison is made by making a linear transformation of the x and y coordinates in reference frame 2, into reference frame 1. The details of the track are shown in Figure B.2(b). The results show very good agreement. The comparison of the yaw motions are shown in Figure B.3, with

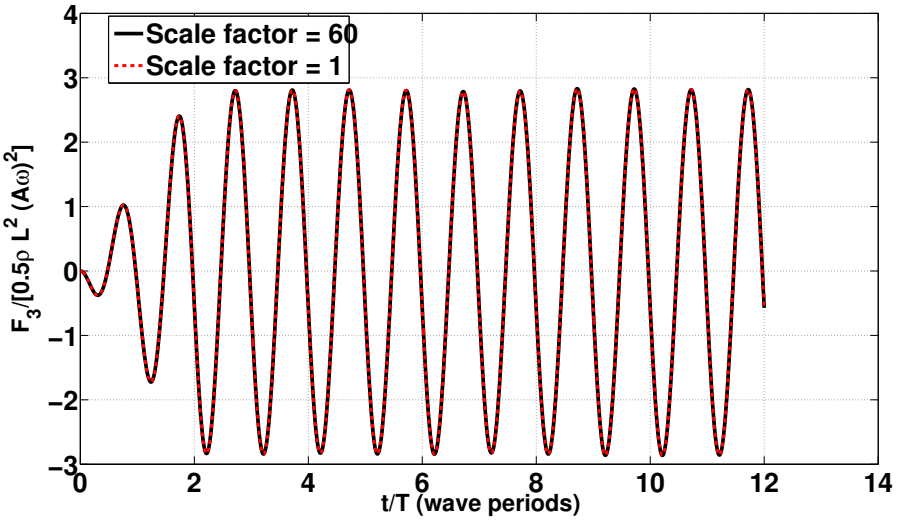

(a) Time history of heave force

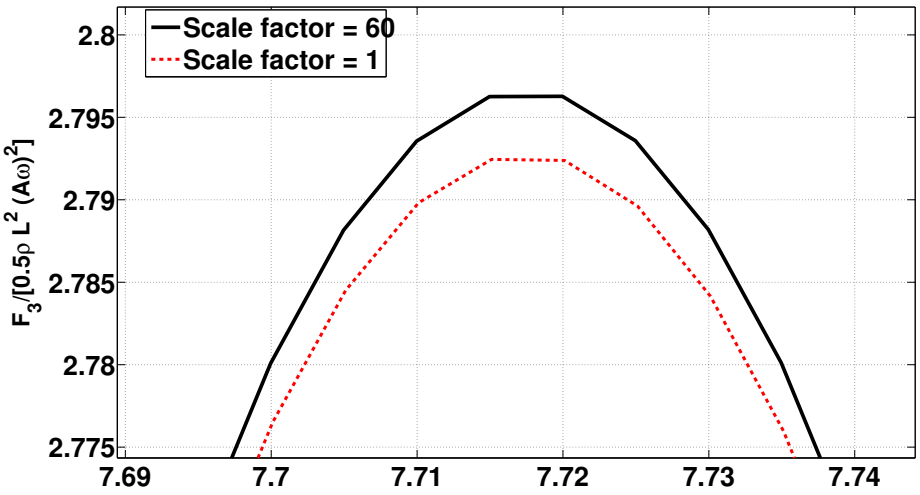

(b) Details

Figure B.1: SCALE FACTOR TEST, WIGLEY-I, FREE SURFACE RESOLUTION = $\lambda/60$. BODY PANELS = 50, TIME-STEP SIZE = $T/200$. FREE SURFACE INNER DOMAIN = 2 WAVELENGTHS.

details of the final steady state solution in Figure B.3(b). Here, the comparisons are made by adding 45^o to the yaw motions in reference frame 2, to get the yaw motions relative to frame 1. Comparisons of the heave and roll motions are made directly, with the results shown in Figure B.4.

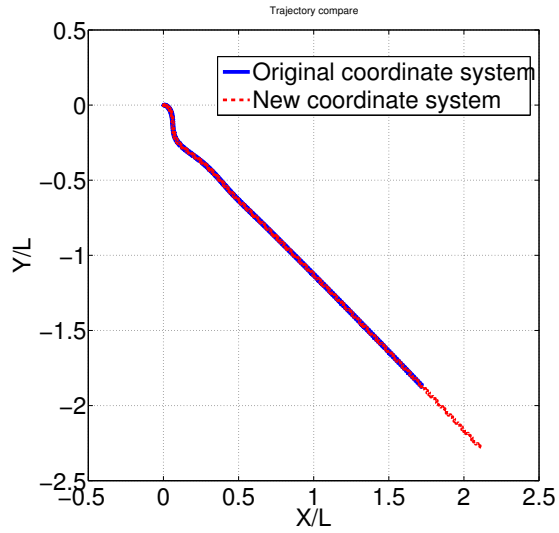

(a) Track of ship

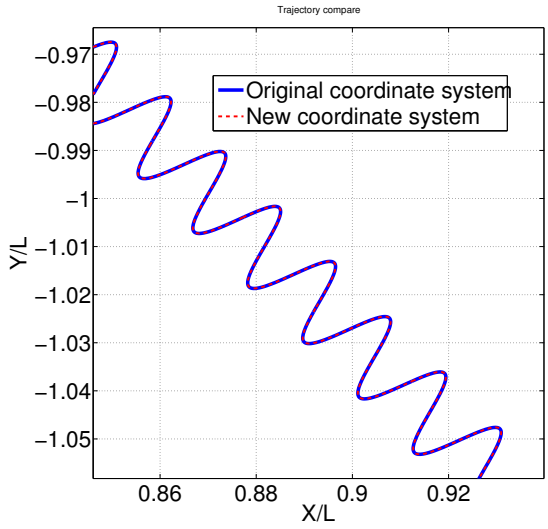

(b) Details

Figure B.2: COMPARISON OF TRACK, COORDINATE FRAME INVARIANCE TEST, WIGLEY-I, FREE SURFACE RESOLUTION = $\lambda/30$. BODY PANELS = 50, TIME-STEP SIZE = $T/200$. FREE SURFACE INNER DOMAIN = 2 WAVE-LENGTHS.

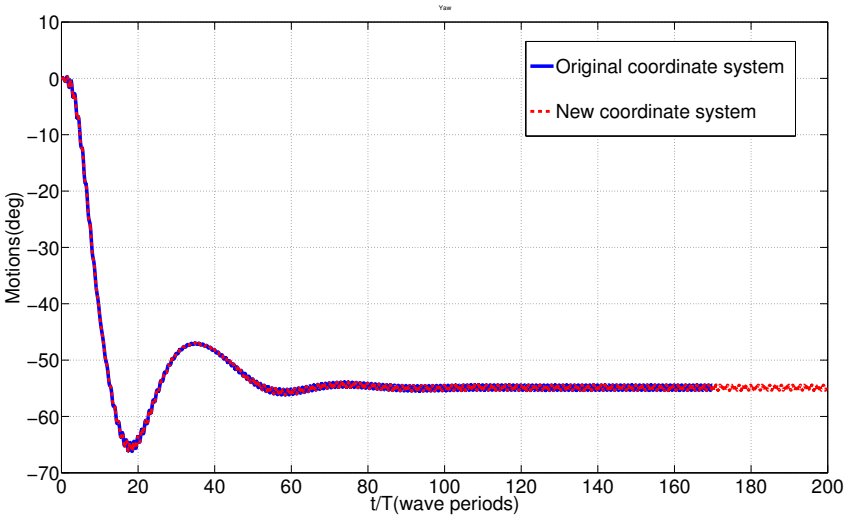

(a) Yaw motions

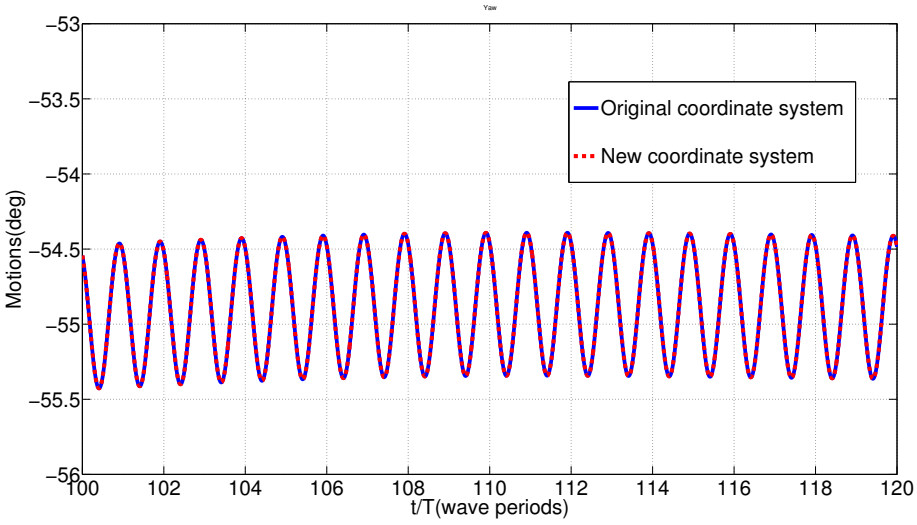

(b) Details

Figure B.3: COMPARISON OF YAW MOTIONS, COORDINATE FRAME INVARIANCE TEST, WIGLEY-I, FREE SURFACE RESOLUTION = $\lambda/30$. BODY PANELS = 50, TIME-STEP SIZE = $T/200$. FREE SURFACE INNER DOMAIN = 2 WAVELENGTHS.

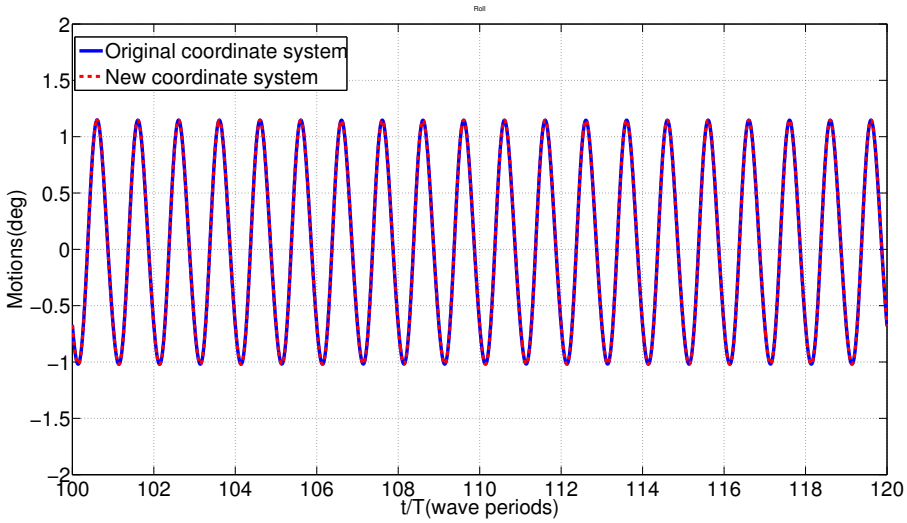

(a) Roll motions

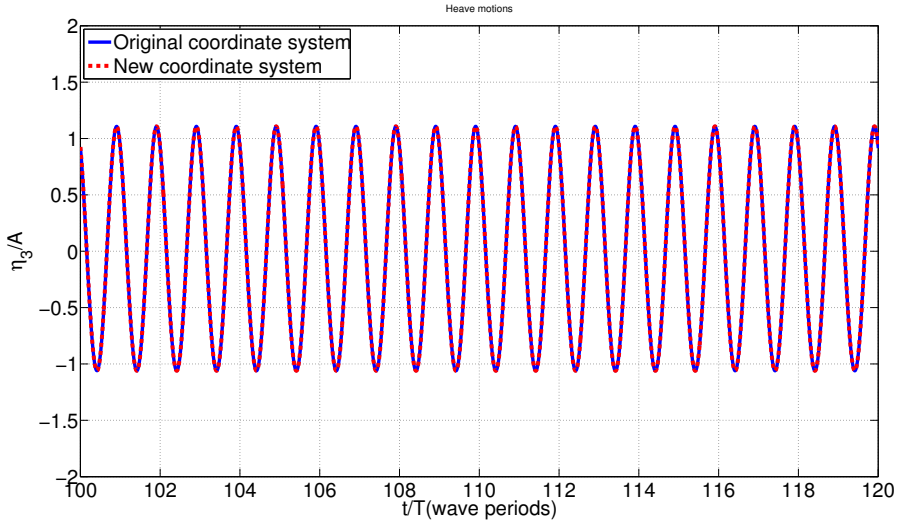

(b) Heave motions

Figure B.4: COMPARISON OF ROLL AND HEAVE MOTIONS, COORDINATE FRAME INVARIANCE TEST, WIGLEY-I, FREE SURFACE RESOLUTION = $\lambda/30$. BODY PANELS = 50, TIME-STEP SIZE = $T/200$. FREE SURFACE INNER DOMAIN = 2 WAVELENGTHS.

BIBLIOGRAPHY

BIBLIOGRAPHY

Bailey, P. A., W. G. Price, and P. Temarel (1997), A unified mathematical model describing the manoeuvring of a ship travelling in a seaway, in *Transactions of The Royal Institution of Naval Architects*, vol. 140, pp. 131–149.

Bandyk, P. J. (2009), A body-exact strip theory approach to ship motions computations, Ph.D. thesis, The University of Michigan, Department of Naval Architecture and Marine Engineering.

Bandyk, P. J., and R. F. Beck (2011), The acceleration potential in fluid-body interaction problems, *J Eng Math*, *70*, 147–163.

Cao, Y., W. W. Schultz, and R. F. Beck (1991), Three-dimensional desingularised boundary integral methods for potential problems, *International Journal for Numerical Methods in Fluids*, *12*, 785–803.

Clarke, D., P. Gedling, and G. Hine (1983), The application of maneuvering criteria in hull design using linear theory, in *Transactions of The Royal Institution of Naval Architects*, pp. 45–68.

Cointe, R., P. Geyer, B. King, B. Molin, and M. Tramoni (1990), Nonlinear and linear motions of a rectangular barge in a perfect fluid, in *Proceedings of the 18th Symp. Naval Hydro.*

Cummins, W. E. (1962), The impulse response function and ship motions, *Tech. Rep. 1661*, David Taylor Model Basin, Hydromechanics Laboratory, USA.

Fang, M. C., J. H. Luo, and M. L. Lee (2005), A nonlinear mathematical model for ship turning circle simulation in waves, *Journal of Ship Research*, *49*(2), 69–79.

Fossen, T. I. (1994), *Guidance and Control of Ocean Vehicles*, John Wiley and Sons.

Fossen, T. I. (2005), A nonlinear unified state-space model for ship maneuvering and control in a seaway, *International Journal of Bifurcation and Chaos in Applied Sciences and Engineering*, *15*(9), 2717–2746.

Himeno, Y. (1981), Prediction of ship roll damping-state of the art., *Tech. Rep. 239*, Univerisity of Michigan, Department of Naval Architecture and Marine Engineering.

Hirano, M., J. Takashina, K. Takeshi, and T. Saruta (1980), Ship turning trajectory in regular waves, in *Transactions of West-Japan Society of Naval Architects*, vol. 60, pp. 17–31.

Li, Z., J. Sun, and R. F. Beck (2010), Evaluation and modification of a robust path following controller for marine surface vessels in wave fields, *Journal of Ship Research*, *54*, 141–147.

Lin, W. M., S. Zhang, K. Weems, and D. Liut (2006), Numerical simulations of ship maneuvering in waves, in *Proceedings of the 26th Symposium on Naval Hydrodynamics*, pp. 17–22.

McCreight, W. R. (1986), Ship maneuvering in waves, in *Proceedings of the 16th Symposium on Naval Hydrodynamics*.

Ottosson, P., and L. Bystrom (1991), Simulation of the dynamics of a ship maneuvering in waves, in *Transactions of Society of Naval Architects and Marine Engineers*, vol. 99, pp. 281–298.

Park, J. H., and A. W. Troesch (1992), Numerical modeling of short-time scale nonlinear water waves generated by large vertical motions of non-wallsided bodies, in *Proceedings of the 19th Symposium on Naval Hydrodynamics*, pp. 143–158, National Academies Press.

Seo, M. G., and Y. Kim (2011), Numerical analysis on ship maneuvering coupled with ship motion in waves, *Ocean Engineering*, *38*, 1934–1945.

Skejic, R., and O. M. Faltinsen (2008), A unified seakeeping nad maneuvering analysis of ships in regular waves, *Journal of Marine Science and Technology*, *13*(4), 371–394.

Son, K., and K. Nomoto (1981), On the coupled motion of steering and rolling of a high speed container ship, *Journal of The Society of Naval Architects of Japan*, *150*, 232–244.

Tanizawa, K. (1996), Long time fully nonlinear simulation of floating body motions with artificial damping zone, *Journal of the Society of Naval Architects of Japan*, *180*, 311–319.

Ueno, M., T. Nimura, and H. Miyazaki (2003), Experimental study on manoeuvring motion of a ship in waves, in *Proceedings of the International Conference on Marine Simulation and Ship Manoeuvrability*.

Wang, M., and A. W. Troesch (1997), Numerical stability analysis for free surface flows, *International Journal for Numerical Methods in Fluids*, *24*(9), 893–912.

Yasukawa, H., and Y. Nakayama (2009), 6-dof motion simulations of a turning ship in regular waves, in *Proceedings of the International Conference on Marine Simulation and Ship Manoeuvrability*.

Yen, T. G., S. Zhang, K. Weems, and W. M. Lin (2010), Development and validation of numerical simulations for ship maneuvering in calm water and in waves, in *Proceedings of the 28th Symposium on Naval Hydrodynamics*, pp. 12–27.